A Maximum-Likelihood Search for Neutrino Point Sources with the AMANDA-II Detector

by

James R. Braun

A dissertation submitted in partial fulfillment of the

requirements for the degree of

Doctor of Philosophy

(Physics)

at the

University of Wisconsin – Madison

2009

A Maximum-Likelihood Search for Neutrino Point Sources with the AMANDA-II Detector

James R. Braun

Under the supervision of Professor Albrecht Karle

At the University of Wisconsin — Madison

Neutrino astronomy offers a new window to study the high energy universe. The AMANDA-II detector records neutrino-induced muon events in the ice sheet beneath the geographic South Pole, and has accumulated 3.8 years of livetime from 2000 – 2006. After reconstructing muon tracks and applying selection criteria, we arrive at a sample of 6595 events originating from the Northern Sky, predominantly atmospheric neutrinos with primary energy 100 GeV to 8 TeV. We search these events for evidence of astrophysical neutrino point sources using a maximum-likelihood method. No excess above the atmospheric neutrino background is found, and we set upper limits on neutrino fluxes. Finally, a well-known potential dark matter signature is emission of high energy neutrinos from annihilation of WIMPs gravitationally bound to the Sun. We search for high energy neutrinos from the Sun and find no excess. Our limits on WIMP-nucleon cross section set new constraints on MSSM parameter space.

Albrecht Karle (Adviser)

Acknowledgments

I owe a debt to many for the support, advice, and friendship I've received and made this work possible.

Particularly, I offer thanks to my adviser Albrecht Karle for his support, for suggesting neutrino point sources and dark matter as fruitful research topics with AMANDA, and for his advice throughout my work. I offer thanks to Bob Morse for my initial interest in AMANDA and IceCube, and to Francis Halzen for sharing his advice and his attitude toward science.

I wish to thank Gary Hill and Chad Finley for many discussions regarding maximum-likelihood techniques and point source analysis. I also thank Kael Hanson and Chris Wendt for the technical skills I've learned working on DOM testing and calibration.

Many thanks to Mark Krasberg for many softball games and sailing trips, and for making the workplace more fun. I thank my office mate John Kelley for nearly always having the answers to my questions and introducing me to the delicious wonders of good coffee.

I wish to thank my parents, Jim and Chris, my grandfather, Ralph, and my uncle, Steve, for encouraging my interest in Science over all these years. Finally, I thank my fiancée Jess for her unyielding love and support throughout this work.

Contents

Chapter 1

The High Energy Universe

Within our known universe are components which are hidden or poorly understood. One such component is associated with the high energy cosmic ray particles which bombard Earth, including particles many orders of magnitude more energetic than those generated by LHC or other collider experiments. The sources of cosmic rays are generally unknown; however, the existence of such particles implies extreme particle accelerators must exist in the universe. Further study of cosmic rays, including neutrino astronomy, will improve our knowledge of this high energy universe and potentially reveal the cosmic ray sources.

1.1 Cosmic Rays

The existence of an energetic ionizing radiation at Earth's surface had been established near the beginning of the 20^{th} century, as several scientists observed that charged, isolated electroscopes slowly discharge with time. The pioneering work establishing cosmic radiation was performed by Hess in 1911-1912, during several high altitude balloon flights. Hess observed the rate of electroscope discharge increases with altitude, establishing that the radiation source is extraterrestrial. The work was published in 1912 [1] and earned Hess a Nobel Prize in 1936.

1.1.1 Cosmic Ray Flux and Composition

The measured cosmic ray flux spans an enormous energy range, stretching to 10^{20} eV and falling roughly with an $E^{-2.7}$ power law above $\sim$1 GeV. The measured cosmic ray spectrum above 10 TeV is shown in figure 1.1, multiplied by $E^{2.7}$. At relatively low energies, below $\sim$1 PeV, cosmic

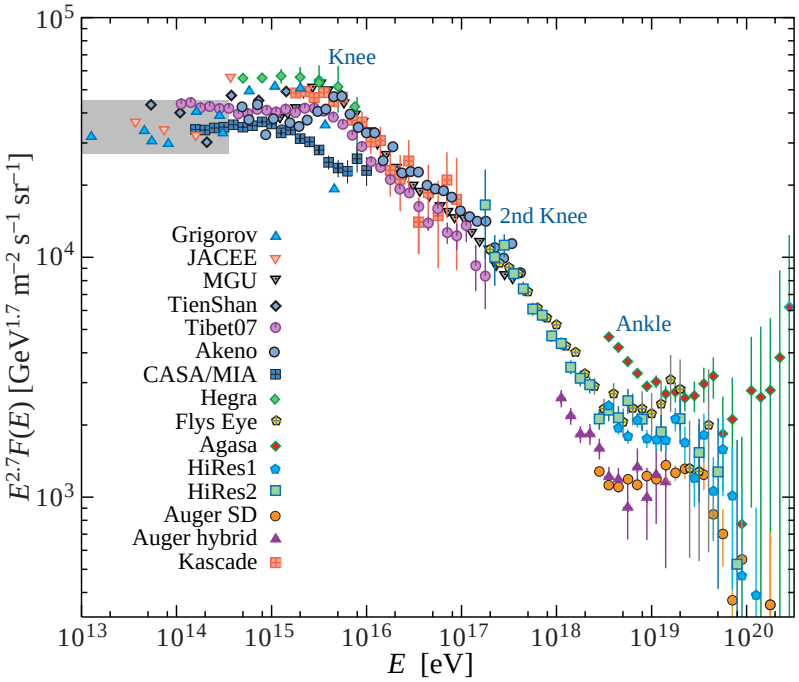

Figure 1.1: Cosmic ray flux measurements of an ensemble of experiments, from [2]. The flux is multiplied by $E^{2.7}$ to enhance the spectral features.

rays are directly measured by spectrometers ($\lesssim$TeV) and particle calorimeters in orbit (e.g. [3, 4]), or in long-duration stratospheric balloon flights (e.g. [5, 6]) above most of the atmosphere. At higher energies, detectors with progressively larger acceptance are required to offset the sharply falling flux with energy. Such acceptance is provided by recording the cascades produced as cosmic rays enter the atmosphere (section 1.3). At the highest energies, these cascades are recorded by giant ground-based air shower detectors [7], atmospheric fluorescence telescopes [8], or both [9]. Above 10^{20} eV, statistics rapidly diminish. Several features are apparent in the energy spectrum. At $\sim$3 PeV the spectrum steepens, a feature known as the "knee", and hardens again at the $\sim$3 EeV "ankle". These features provide clues to cosmic ray origins; particularly, it is believed that the ankle represents a transition from galactic cosmic rays to those produced by more powerful extragalactic sources. Above $\sim$60 EeV the spectrum again steepens [10, 11]. This steepening is evidence of the GZK cutoff [12], discussed

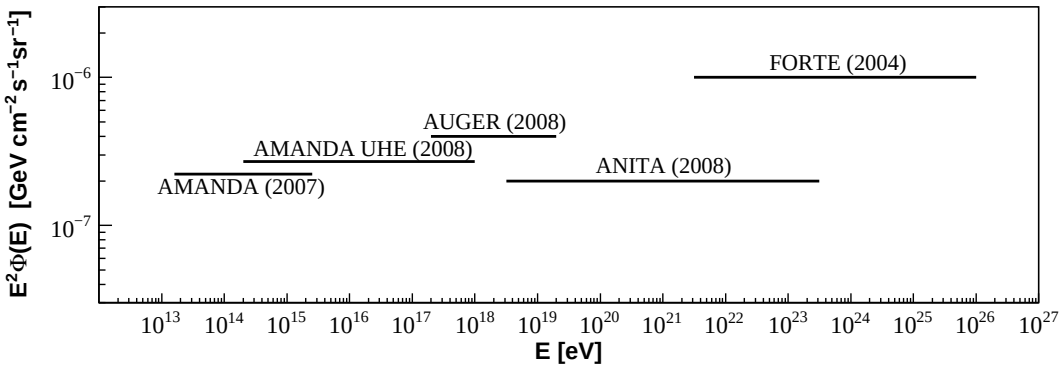

Figure 1.2: Current limits on E^{-2} all-flavor neutrino cosmic ray fluxes above 10 TeV

further in section 1.2.

Cosmic rays are primarily composed of hadronic particles, generally protons and heavier nuclei. The ratio of these constituent nuclei is currently an active area of research, and significant uncertainty exits at high energies [13, 14]. The flux of hadronic cosmic rays is very nearly isotropic at Earth due to magnetic scrambling from galactic and extragalactic magnetic fields. A small (0.1%) anisotropy exists in arrival directions at ∼TeV energies [15, 16, 17], possibly due to the local magnetic field or a nearby cosmic ray source. Below ∼100 TeV, a small fraction of cosmic rays are known to be photons, and, since photons are not deflected by magnetic fields, many TeV photon sources have been discovered [18, 19, 20]. Many of these TeV photon sources are candidate sources of hadronic cosmic rays. At ∼TeV energies and below, electrons and positrons constitute a small fraction of cosmic rays. Measurements of cosmic ray electrons and positrons [21, 22, 23, 24] and positron fraction [25] may provide evidence for WIMP dark matter, discussed further in chapter 8. No neutrino component of cosmic rays has yet been discovered [26, 27, 28, 29, 30, 31, 32, 33, 34, 35]. Flux limits on this neutrino component above 10 TeV are shown in figure 1.2.

1.1.2 Cosmic Ray Energization

The mechanisms thought to generate high energy cosmic rays are grouped in two categories.

- The **top-down scenario**: Supermassive particles with long lifetimes decay, producing cosmic rays energized by the rest mass of the parent particle.

- The **bottom-up scenario**: Low energy particles in the vicinity of energetic astrophysical phenomena are energized and propagate to Earth as cosmic rays.

Sources of supermassive particles in top-down models include super-heavy dark matter [36, 37] and topological defects [38]. Many top-down models are largely constrained. Models suggesting that ultra-high energy cosmic rays (UHECR) are produced locally in the galactic halo are constrained by observations of the GZK cutoff, discussed in section 1.2, and by measurements of the cosmic ray photon fraction [39, 40]. Top-down UHECR models at cosmological distances are constrained by limits on ultra-high energy neutrino fluxes and the diffuse GeV galactic photon flux [41].

The most widely accepted bottom-up acceleration mechanism is Fermi acceleration [42]. In first order Fermi acceleration, charged particles are energized by interactions with relativistic shocks. Such particles are confined to the shock by magnetic inhomogeneities and are energized by repeated magnetic reflection through the shock front. The repeated energization creates nonthermal, power law spectra with indices

$$\frac{dN}{dE} \simeq \mathrm{E}^{-\gamma}; \qquad \gamma \geq 2. \tag{1.1}$$

Charged particles can no longer be confined to the shock when the particle gyroradii approach the geometric size of the shock; therefore, the maximum energy attainable is a function of magnetic field strength and source size:

$$R = \frac{p}{q\mathrm{B}_{\perp}} = \frac{\mathrm{E}/c}{\mathrm{Z}e\mathrm{B}_{\perp}} \tag{1.2}$$

$$\frac{\mathrm{E}_{max}}{\mathrm{GeV}} \simeq 3 \times 10^{-2} \times \mathrm{Z} \times \frac{\mathrm{R}}{\mathrm{km}} \times \frac{\mathrm{B}}{\mathrm{G}}. \tag{1.3}$$

Figure 1.3, originally produced by Hillas [43], illustrates the source sizes and magnetic fields necessary to generate the highest energy cosmic rays, along with the estimated size and magnetic field for several classes of astronomical objects.

1.1.3 Candidate Cosmic Ray Accelerators

From the Hillas diagram in figure 1.3, several classes of energetic objects have the potential to accelerate cosmic rays to ∼PeV energies and beyond. Some of the most important include:

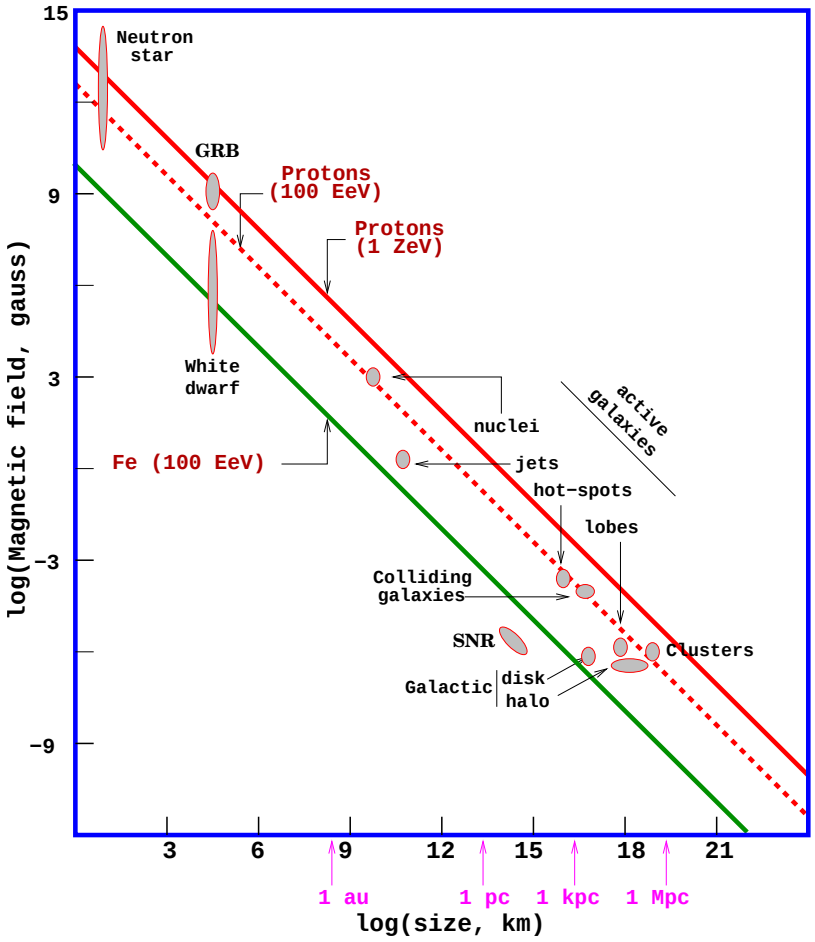

Figure 1.3: 'Hillas diagram' of source sizes and magnetic fields necessary to accelerate EeV cosmic rays, including the sizes and estimated magnetic fields for several classes of astronomical objects, from [44].

- **Active Galactic Nuclei (AGN)**: Active galaxies are significant sources of nonthermal radiation, thought to be powered by matter accretion on a central supermassive black hole. AGN are extensively classified based on the presence of relativistic jets, radio luminosity, x-ray luminosity, and other criteria [45]. Importantly, the nonthermal keV x-ray emission observed from some AGN is likely synchrotron radiation from shock accelerated electrons and indicates potential for hadron acceleration. Several AGN are known TeV photon emitters [46]. The TeV flux is variable in time, with occasional flaring on timescales of ∼days often linked to flares in nonthermal x-rays (e.g. [47]).

- **Gamma Ray Bursts (GRBs)**: GRBs are short (10^{-3} s – 10^{3} s [48]), highly energetic (E $> 10^{50}$ erg) bursts of keV – MeV photons from cosmological distances. The radiation is believed to be beamed along an expanding ultra-relativistic fireball [49] with a Lorenz factor of 100-1000 [50]. Similar to AGN, the keV – MeV emission is thought to be synchrotron emission from shock accelerated electrons.

- **Microquasars**: Microquasars are potential galactic sources with relativistic jets similar to AGN, except microquasars are much smaller; the central engine is a neutron star or black hole up to a few stellar masses. Several microquasars are significant TeV photon sources [46], and many are bright x-ray sources.

- **Supernova Remnants (SNRs)**: Supernovae are the most powerful explosions known in our galaxy, and the relativistic shocks produced expand for many years and are a possible cosmic ray acceleration source. SNRs can be broadly classified into two categories: Those with a central pulsar producing a relativistic wind (PWN), including the Crab, and those which are shell-like, including Cas A, with the latter type often considered the most likely source of Galactic cosmic rays up to ∼PeV energies [51]. Many SNRs of both types emit TeV photons [46].

Finally, the Sun is a known source of cosmic rays at the lowest energies, as energetic solar events accelerate protons up to ∼GeV energies.

1.2 Cosmic Ray Interaction with Matter and Radiation

Any high energy charged particles produced by cosmic ray accelerators or high energy particles in top-down models may interact with matter and radiation. The rate of such interactions is generally highest at the source, where local particle and photon densities are high.

1.2.1 Charged Particles

Energized protons and nuclei in cosmic ray accelerators would interact with other hadrons or with photons, producing energetic mesons:

$$\begin{aligned} p + X &\longrightarrow \pi^{\pm}(\pi^0) + \mathrm{X}' \\ p + X &\longrightarrow K^{\pm}(K^0) + \mathrm{X}' \\ p + \gamma &\longrightarrow p(n) + \pi^0(\pi^+). \end{aligned}$$

A fraction of heavier mesons are also produced, discussed in section 1.3. Interaction of the mesons is strongly disfavored at shock densities, and the mesons generally decay:

$$\begin{aligned} \pi^{\pm} &\longrightarrow \nu_\mu(\bar{\nu}_\mu) + \mu^{\pm} \\ &\qquad \mu^{\pm} \longrightarrow \bar{\nu}_\mu(\nu_\mu) + e^{\pm} + \nu_e(\bar{\nu}_e) \\ \pi^0 &\longrightarrow \gamma\gamma \\ K^{\pm}(K^0) &\longrightarrow \pi^{\pm}, \pi^0, \mu^{\pm}, \nu_\mu, e^{\pm}, \nu_e. \end{aligned}$$

Any interaction of high energy charged particles near the source therefore produces a significant photon flux, through π^0 decay, and a significant neutrino flux, through kaon and charged pion decay with subsequent muon decay, with a neutrino and antineutrino flavor ratio

$$\nu_e : \nu_\mu : \nu_\tau = \bar{\nu}_e : \bar{\nu}_\mu : \bar{\nu}_\tau \sim 1{:}2{:}0,$$

expected to oscillate into a flavor ratio of ∼1:1:1 at Earth. Estimates of such neutrino fluxes have been made for specific sources (e.g. [51, 52, 53, 54]), average GRBs [55], and for the total diffuse fluxes produced by AGN [56, 57], starburst galaxies [58], and GRBs [59]. Some of these predictions are based on observed TeV photon fluxes by assuming the TeV photons are from hadronic π^0 decay and calculating the complimentary neutrino flux from charged pion decay.

Such accelerators would additionally produce TeV photons through inverse Compton scattering of shock accelerated electrons on background photons. A major source of background photons is the synchrotron emission from within the shock. This synchrotron self-Compton emission is particularly

significant in the photon spectra of AGN. Importantly, TeV photons from hadronic π^0 decay cannot be easily separated from TeV inverse Compton emission, and typically spectral fitting is done to identify a hadronic component. Several sources with spectra relatively incompatible with inverse Compton emission alone have been observed [60, 61]; however, such observations are not considered conclusive evidence of hadronic π^0 decay due to uncertainty in source parameters, including magnetic field strength and background photon densities. Finally, any TeV electrons which propagate away from the source are rapidly attenuated by Compton scattering on background photons; thus TeV electrons travel at most ∼500 parsecs [62].

Protons and nuclei propagating from the source as cosmic rays may additionally interact with photons in free space. The cosmological microwave background (CMB) photons are extremely abundant and thus especially important. For protons, interaction with CMB photons is possible at center of mass energies above the threshold for delta resonance:

$$\begin{aligned} p + \gamma_{\text{CMB}} \longrightarrow \Delta^+ &\longrightarrow p + \pi^0 \\ &\longrightarrow n + \pi^+. \end{aligned}$$

In the lab frame, the minimum threshold is the ∼60 EeV GZK cutoff [12] and imposes a ∼50 Mpc distance limit [10] on particles arriving at Earth above ∼60 EeV (figure 1.4). The GZK pions from Δ^+ decay produce UHE photons and neutrinos; particularly, a significant GZK neutrino flux is expected at Earth (e.g. [63, 64]).

1.2.2 Photons

Since photons are not deflected by magnetic fields, photons are not magnetically bound to sources and are not deflected while propagating through space. Photons are attenuated, however, by pair production with background photons:

$$\gamma + \gamma_{\text{bgd}} \longrightarrow e^- + e^+.$$

Above ∼1 TeV, photons traveling >100 Mpc are attenuated by infrared background radiation (figure 1.4). The density of the infrared background is not well known, therefore the absolute luminosities of distant TeV photon sources are uncertain. Above 100 TeV, pair production on the much more numerous CMB photons limits photon range to ∼1 Mpc, and above 1 PeV, only our galaxy is visible.

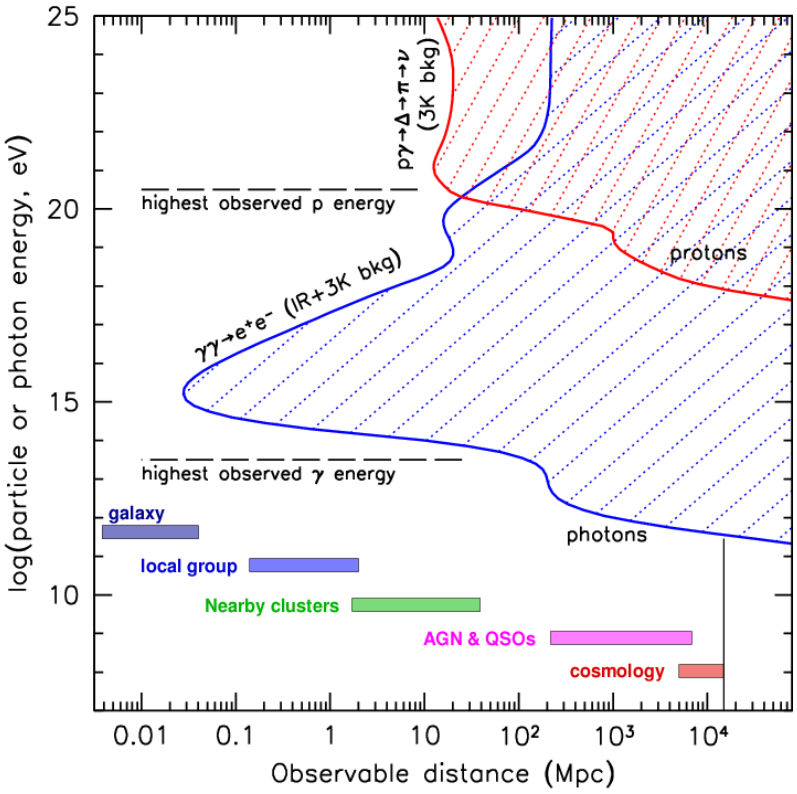

Figure 1.4: Observable distance for photons and protons, from P. Gorham [65].

1.2.3 Neutrinos

The interaction of Neutrinos with matter is described in detail in chapter 2. The universe is essentially transparent to neutrinos at energies up to ∼ZeV; therefore neutrinos can travel unimpeded from cosmological distances. The transparency of matter to neutrinos presents an obvious problem for neutrino detection, discussed in chapter 2.

1.3 Cosmic Ray Air Showers

Charged particles and photons interact upon entering the upper levels of the relatively dense atmosphere and initiate air shower cascades. Air showers initiated by photons and electrons propagate electromagnetically and differ considerably from those initiated by hadrons, which proceed additionally by the strong nuclear force.

1.3.1 Electromagnetic Showers

Electrons and positrons with energies above ∼100 MeV primarily lose energy via bremsstralung and emit high energy photons. Photons at such energies dominantly produce electron-positron pairs on the nuclear or electron fields. The radiation length for either process in the air is $\lambda_\gamma \sim \lambda_{e^-} \sim 40$ g/cm^2; the resulting cycle between photons and electrons/positrons results in a smooth, geometric increase of photons and electrons with depth up to a shower maximum, where the increase is overtaken by particle losses from the shower. The maximum occurs deeper in the atmosphere at higher energies. Finally, photons occasionally produce muon-antimuon pairs. The energy loss rate of muons is much less than electrons of similar energy (section 2.2), and these muons can carry shower energy significantly deeper than the electrons and photons.

1.3.2 Hadronic Showers

Cosmic ray protons and nuclei initiate hadronic showers in the atmosphere and produce pions, kaons, and heavier mesons, illustrated in figure 1.5. These mesons receive a fraction of the primary energy and therefore follow the primary cosmic ray spectrum of $\sim E^{-2.7}$. Hadronic interaction lengths are somewhat longer than electrons and photons, with $\lambda_n \sim 80$ g/cm^2 for nucleons and $\lambda_\pi \sim 120$ g/cm^2 for pions. Charged pions and kaons alternatively can decay and produce muons and neutrinos,

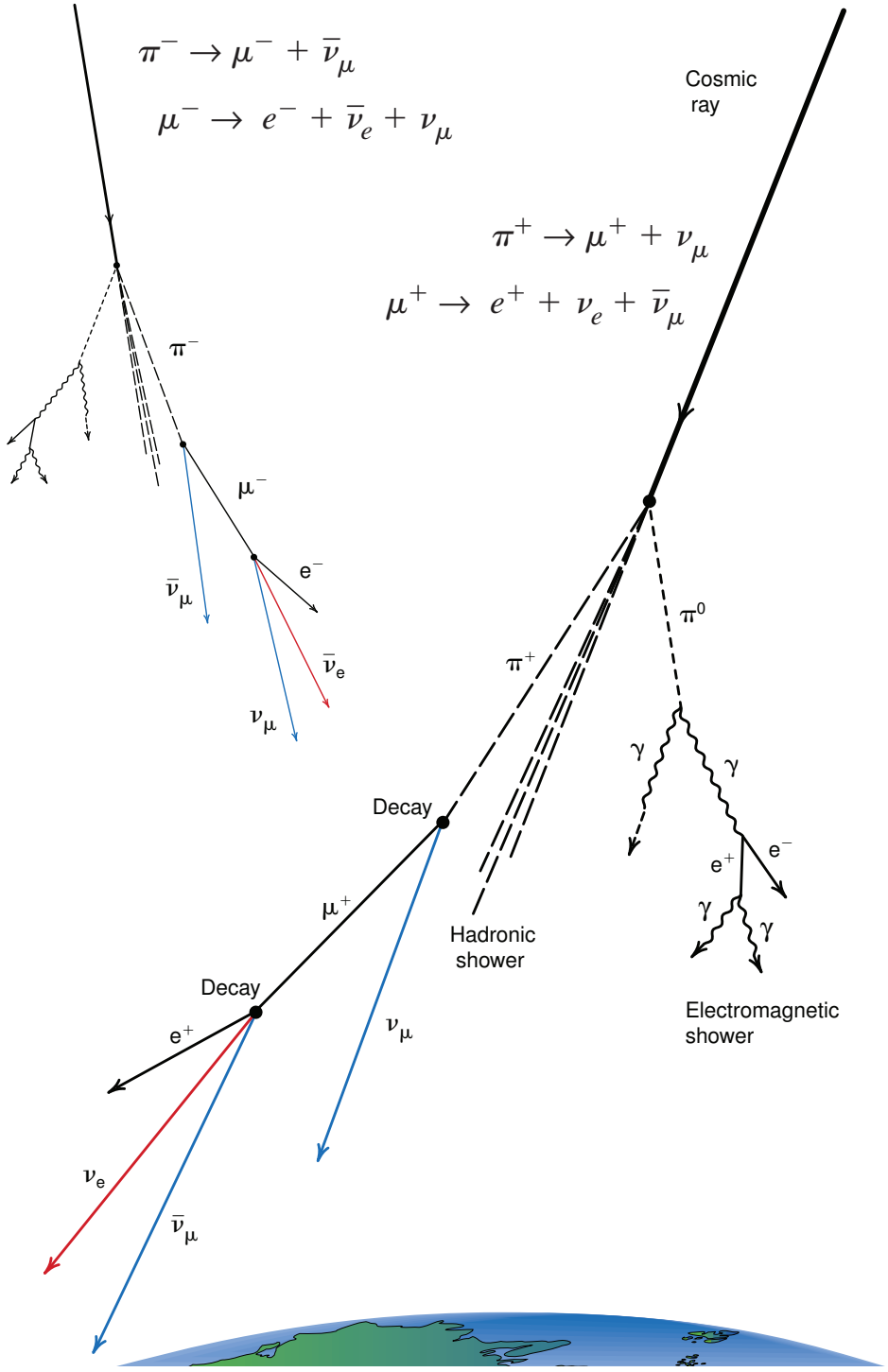

Figure 1.5: Illustration of a cosmic ray air shower, from [66].

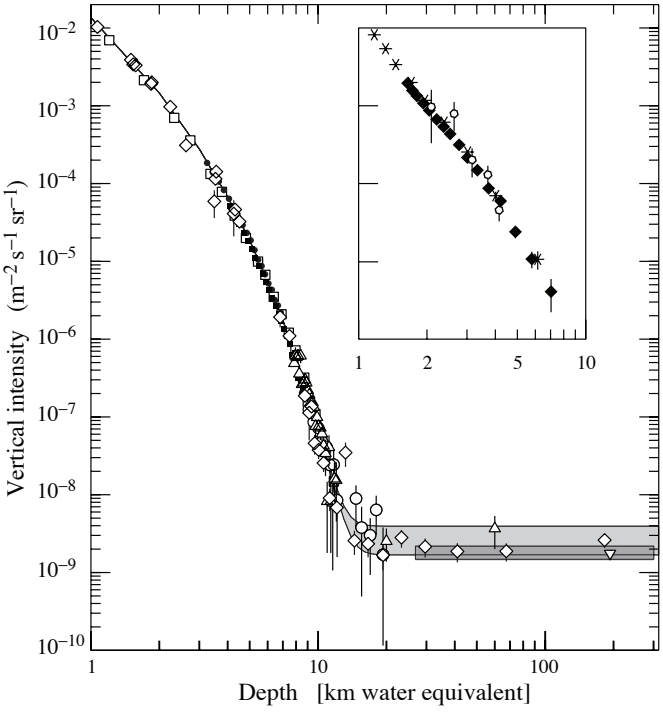

Figure 1.6: Muon flux vs. depth, from [2]. Muons induced by atmospheric neutrinos are relatively constant with depth and dominate the muon flux for depths greater than 20 km water equivalent.

described in the next section. The mesons carry energy away from the core of the shower, making the energy density within hadronic showers considerably more uneven than within electromagnetic showers. Finally, hadronic showers are generally accompanied by an electromagnetic component initiated by photons from the relatively instantaneous decay of charged pions.

1.3.2.1 Atmospheric Muons and Neutrinos

Mesons produced in hadronic showers may decay before interacting, producing muons and neutrinos which carry energy well beyond the maximum extent of the electromagnetic component of the shower and penetrate deep into the Earth. Measurements of the cosmic ray muon flux as a function of depth are shown in figure 1.6. The probability of meson decay is suppressed by the Lorentz factor, and the suppression is asymptotically E^{-1} at high energies. For atmospheric neutrinos, this results

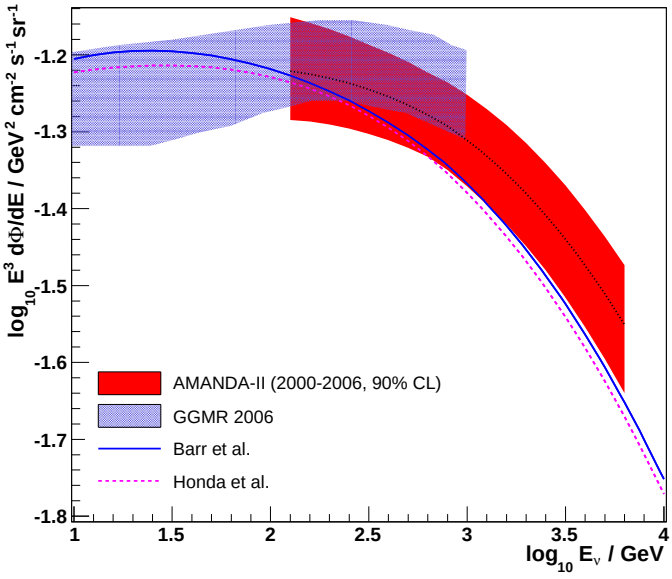

Figure 1.7: Measured and predicted atmospheric neutrino flux vs. energy, from [67].

in an energy spectrum of $\sim E^{-3.7}$ above $\sim$TeV. Measurements [67, 68] and models [69, 70] of this atmospheric neutrino flux are shown in figure 1.7. The meson interaction probability strongly depends on gas density, with low density favoring decay; thus, the atmospheric neutrino and muon rates vary seasonally, with higher rates produced by the less dense summer atmosphere, and at shorter time scales according to the stratospheric weather in the top 20 kPa of the atmosphere. Mesons entering the atmosphere at slanted angles also encounter less atmospheric mass, favoring decay; therefore, the atmospheric neutrino flux is zenith-dependent. Heavy mesons, including charm mesons, decay before interaction and should yield an additional $\sim E^{-2.7}$ component to the atmospheric neutrino and muon spectra. These *prompt* neutrinos should increase the atmospheric neutrino flux at high energies, but prompt fluxes have not yet been observed [26] and prompt models (e.g. [71]) are largely uncertain.

1.4 High Energy Astronomy

An ultimate goal of cosmic ray physics is astronomy, tracing high energy particles back to their origins and thus correlating cosmic ray emission with known astrophysical objects, perhaps some of the candidates described in section 1.1.3. TeV photon astronomy has been very successful; however,

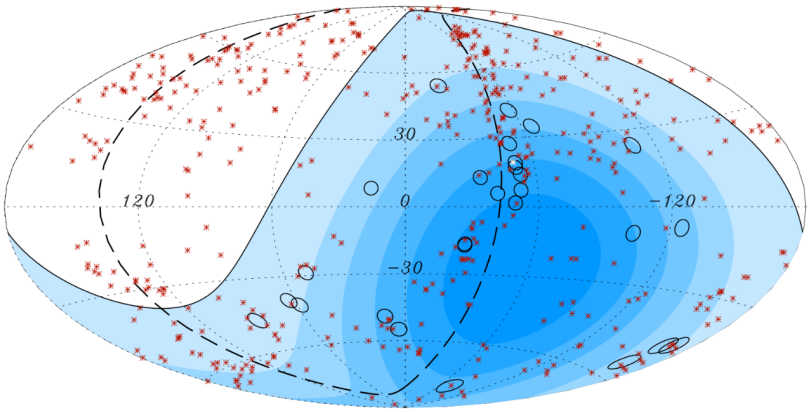

Figure 1.8: Skymap of 27 UHE cosmic ray events observed by Auger [73] with 3.1° angular ellipses (black) and AGN within 75 Mpc (red asterisks).

there is no strong evidence linking hadronic cosmic rays, which constitute the bulk of the cosmic ray flux, with any particular sources.

1.4.1 Charged Particles

Charged particles are deflected by magnetic fields, effectively scrambling their trajectories through galactic and intergalactic space. Magnetic effects are minimized by selecting only the highest energy cosmic ray events, which have the largest gyroradii, at a cost of reducing the data to a handful of events above a few tens of EeV. The AGASA and Auger air shower arrays reconstruct these high energy events with $\sim 1^\circ - 1.5^\circ$ angular resolution, while the Auger and HiRes fluorescence detectors are more accurate. No significant excesses at any point in the sky consistent with the detector angular resolution have been observed by AGASA and HiRes [72]. If no individual source produces a significant excess, the cumulative excess from a catalog of potential sources may still be significant. Such *source stacking* approaches may detect this cumulative excess and are further described in section 7.2.4. Auger reports a marginally significant correlation of 27 recorded cosmic ray events with energies above $\sim$60 EeV, shown in figure 1.8, to a catalog of AGN within 75 Mpc [73]. A similar correlation is not observed by HiRes [74] using the same source catalog.

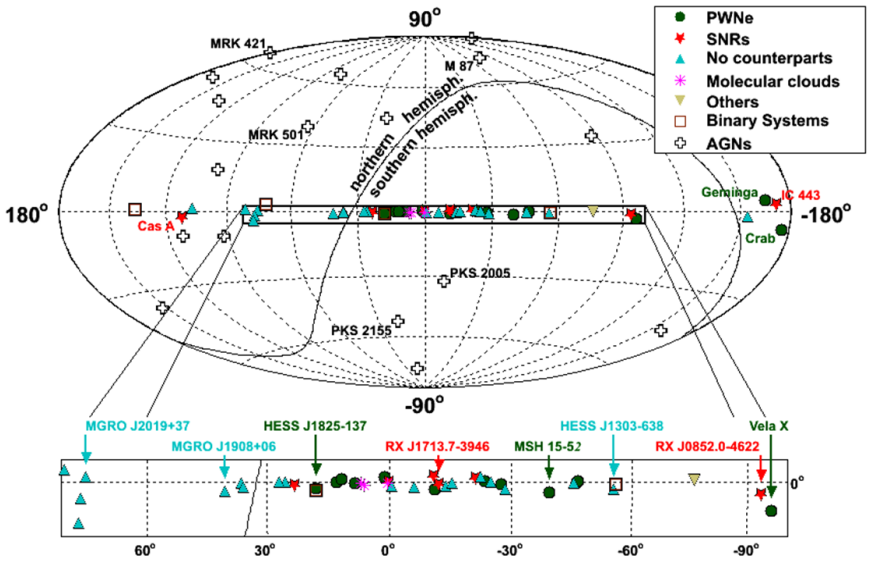

Figure 1.9: Known TeV gamma ray sources listed according to known astrophysical counterparts, courtesy of A. Kappes.

1.4.2 Photons

Gamma ray astronomy has now discovered 75 sources with TeV photon emission [46], many of them shown in figure 1.9. The extragalactic TeV sources discovered to date generally have AGN counterparts. Most galactic TeV sources are associated with supernova remnants and microquasars, although some do not have identified counterparts.

TeV photon experiments are broadly classified into two types: Imaging air-Cherenkov telescopes (IACTs) and high-density air shower arrays. The newest IACTs [75, 76, 77] image the Cherenkov light produced by atmospheric air showers (section 2.3.1) onto a "camera" array of photomultiplier tubes using a large diameter ($\sim$12 – 17 m) mirror array. Reconstruction of the air shower uses camera timing and pixel position information, and is accurate to $\sim$0.1°. IACTs have a field of view of $\sim$3° – 5° and operate only on clear, moonless nights. Alternatively, air shower gamma ray experiments [78, 79, 80] record the electromagnetic shower directly, and reconstruction of the shower front gives $\sim$1° pointing resolution. Air shower experiments are largely complimentary to IACTs. IACTs have significantly better pointing resolution and a lower energy threshold; however air shower

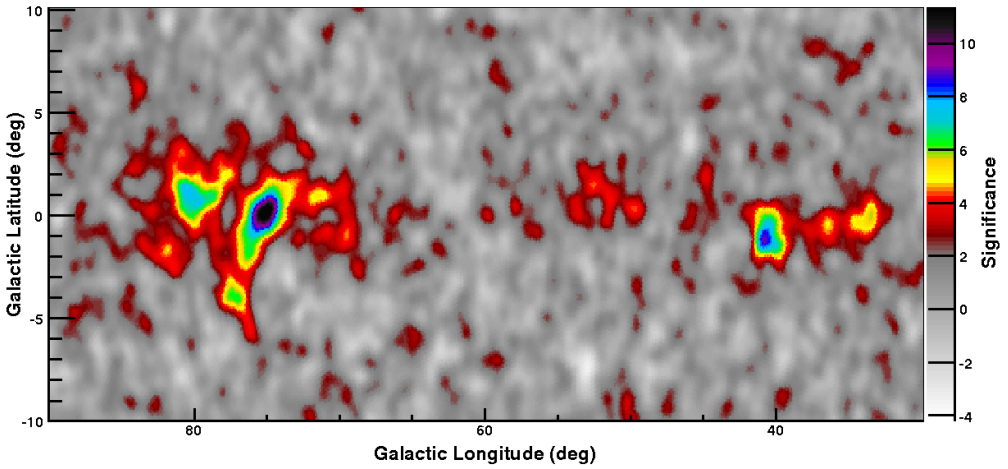

Figure 1.10: Milagro skymap showing TeV gamma ray sources near the galactic plane, with several strong sources in the Cygnus region [81].

experiments observe nearly half the sky simultaneously and are capable of an almost 100% duty cycle.

From the perspective of potential hadronic cosmic ray acceleration, the sources with the highest energy photon emission are some of the most interesting. Several new TeV sources [18], shown in figure 1.10, discovered by the Milagro air shower array are particularly compelling. The sources are galactic, and a cluster of activity exists near the Cygnus region. Several of the sources have been subsequently observed by IACTs [82, 83] and exhibit hard power law spectra with $\gamma \sim 2$, indicative of Fermi acceleration. The energy spectrum observed by HESS for the source MGRO J1908+06 is shown in figure 1.11. An observation of high energy neutrinos from MGRO J1908+06 and other TeV photon sources would confirm a component of the TeV emission is from pion decay and establish the sources as regions of cosmic ray acceleration.

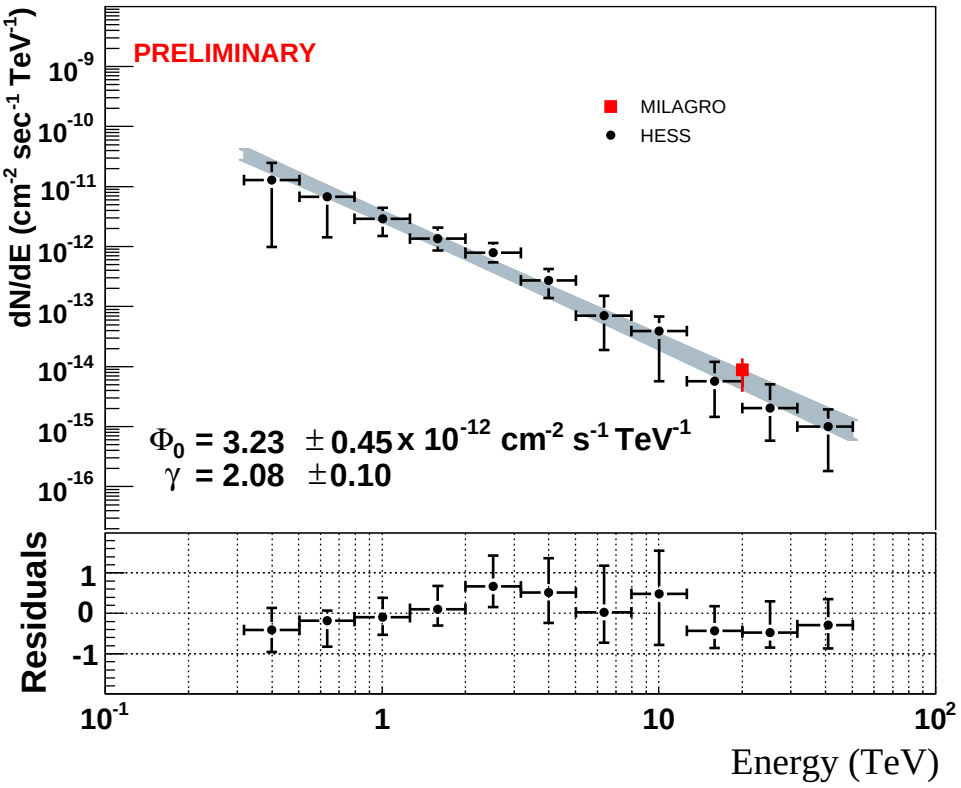

Figure 1.11: Energy spectrum of MGRO J1908+06 measured by HESS [82].

Chapter 2

High Energy Astronomy with Neutrinos

High energy (>TeV) neutrino astronomy is a long standing goal of astrophysics. Since neutrinos are neither deflected by magnetic fields nor significantly attenuated by matter and radiation en route to Earth, neutrino astronomy offers an undistorted view of the high energy universe. Particularly, since high energy neutrinos are an end product of high energy hadronic processes and are not produced by electromagnetic processes, neutrino astronomy offers an opportunity to unambiguously identify the sources of cosmic rays.

Neutrinos interact with matter through the weak nuclear force and thus have much smaller interaction cross sections than photons or charged particles; neutrinos can pass through a significant portion of the Earth. These small cross sections present the most significant difficulty associated with neutrino detection. Very large detectors are necessary to record enough neutrino interaction events to observe the predicted small neutrino fluxes.

2.1 Neutrino Interaction

Four neutrino interaction modes are generally considered:

$$\begin{array}{lcll} \nu_l + X & \longrightarrow & \nu_l + \mathrm{X}' & \text{(Neutral Current)} \\ \nu_l + X & \longrightarrow & l + \mathrm{X}' & \text{(Charged Current)} \\ \bar{\nu}_e + e^- & \longrightarrow & W^- & \text{(Glashow Resonance)} \\ \nu_l + \bar{\nu}_l & \longrightarrow & Z & \text{(Z-Burst)} \end{array}$$

where l is the neutrino flavor eigenstate, electron (ν_e), muon (ν_μ), or tau (ν_τ). The cross sections of the first three of these modes are shown in figure 2.1. These modes involve the following processes.

- **Neutral Current**: The neutrino exchanges a Z boson with a nucleon, depositing a fraction of its energy and initiating a hadronic cascade. The original neutrino exits the interaction with reduced energy and an angular deviation.

- **Charged Current**: The neutrino exchanges a W boson with a nucleon, initiating a similar hadronic cascade. Additionally, an energetic lepton is produced with a substantial fraction of the initial neutrino energy.

- **Glashow Resonance**: For the interaction of anti-electron neutrinos with electrons, resonant production of W bosons occurs at neutrino energies near ∼6.3 PeV and significantly enhances the anti-electron neutrino cross section, shown in figure 2.1. Equivalent interactions are possible with muon and tau flavors, but neither muons nor tau particles are currently practical targets.

- **Z-Burst**: Resonant production of Z bosons is possible for interactions between antineutrinos and neutrinos at an energy $E \sim \frac{m_Z^2 c^4}{4E'_\nu}$ if the target neutrino is relativistic with energy E'_ν, or $E = \frac{m_Z^2 c^2}{2m_\nu}$ if the target neutrino is nonrelativistic. One particular target is the theorized cosmologic neutrino background, which would partially absorb UHE neutrinos [85] above $\sim 10^{21}$ eV. Z-bursts, however, do not provide a practical way to detect high energy neutrino fluxes at Earth.

Neutral current and charged current interactions provide the potential to detect neutrinos over a significant energy range, with the associated cross sections increasing with neutrino energy, and anti-electron neutrino detection is enhanced near the ∼6.3 PeV Glashow resonance. All three modes produce cascades which can be detected when the interaction occurs within the detector volume. Additionally, charged current interaction produces charged leptons, and electrons, muons, and tau particles have characteristic energy loss signatures.

2.2 Lepton Propagation

The pattern of energy deposition along the lepton path is determined by the relative rate of continuous losses from ionization, large stochastic losses from bremsstralung, pair production, and photonuclear interactions, and for muons and especially tau particles, lepton decay.

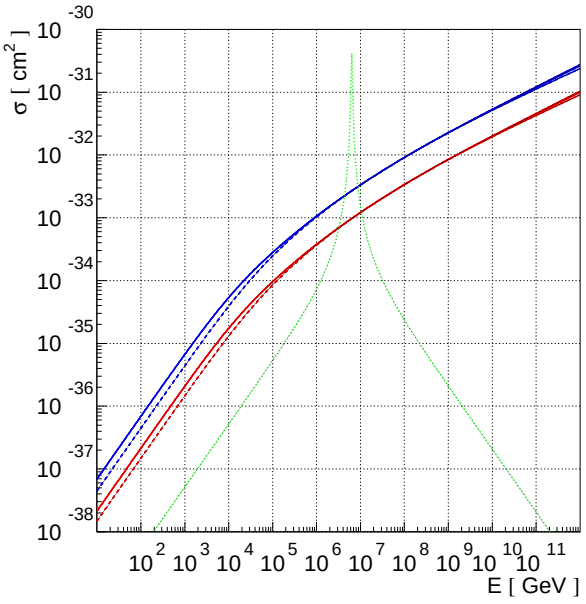

Figure 2.1: Neutrino cross sections for charged current (blue) and neutral current (red) for ν (solid) and $\bar{\nu}$ (dashed), from [84]. Also shown is $\bar{\nu}_e + e^- \longrightarrow W^-$ (dotted green) with the Glashow resonance at E_ν ∼6.3 PeV.

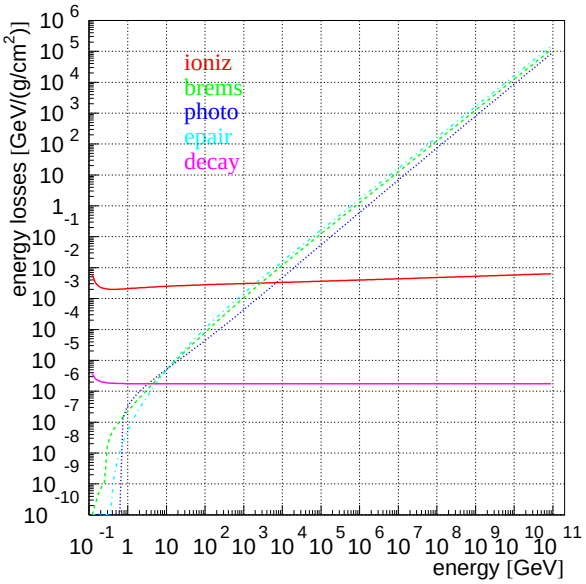

Figure 2.2: Muon energy losses in ice, from [84].

2.2.1 Electrons

Electron energy losses are strongly dominated by bremsstralung above ∼1 GeV in ice and other materials. Electrons deposit all of their energy within a few meters water equivalent (mwe), leaving relatively short and bright electromagnetic cascades.

2.2.2 Muons

Muon energy losses in ice are shown in figure 2.2 as a function of muon energy. Loss rates are generally much smaller than those of electrons at the same energy due to the significantly larger relative mass of the muon; therefore muons produce significantly longer tracks. Below ∼1 TeV, continuous energy losses from ionization dominate, with losses of 200 MeV per mwe. Above ∼1 TeV, stochastic losses become significant and substantially increase the energy loss rate, rising proportionally with the muon energy. The typical muon track length is roughly proportional to energy up to ∼1 TeV, reaching ∼2.5 km. Above ∼1 TeV, the muon track length increases logarithmically with energy, reaching ∼20 km at 1 PeV [84]. Thus, muons do not need to interact within the detector to be observed; they propagate from significant distances.

2.2.3 Tau Particles

Tau particles produce short tracks ending in decay due to the short tau lifetime of $\sim 3 \times 10^{-13}$ s. At the decay vertex, a tau neutrino is regenerated and a cascade is produced for hadronic and electron decay modes. This "double bang" signature, with a cascade at the start and end of the track, is unique to tau events. The two cascades are separated by a short track length, determined by the tau Lorenz factor, of ∼100 m for tau energies of a few PeV. The secondary tau neutrino, with a fraction of the primary neutrino energy, propagates from the vertex and may interact again. The tau track itself is not as energetic as a muon track due to the higher relative mass of the tau. Finally, tau decay produces a muon rather than a cascade with a branching ratio of 17.4%.

2.3 TeV Neutrino Detection

The most sensitive method currently available for TeV neutrino detection is the optical Cherenkov technique. Water and ice serve as practical Cherenkov radiative media, as they have good optical properties and are available in large volumes. An array of optical sensors is placed in the water or ice, and the Cherenkov light produced by tracks and cascades within the detector active volume are recorded as events. Energy resolution and angular resolution are critical to distinguish astrophysical neutrino events from the background of muons and neutrinos from cosmic ray air showers.

2.3.1 Cherenkov Radiation

Cherenkov radiation is emitted by transparent, electrically insulating media when relativistic charged particles pass through, provided the particle velocity is greater than the phase velocity of light in the medium at a given wavelength. The photons propagate from the track in a conical shock front, emitted at an angle

$$\cos\theta_c = \frac{1}{\beta n_g} \tag{2.1}$$

relative to the track, where $\beta = \frac{v}{c}$ and n_g is the group index of refraction of the medium. For relativistic leptons with energies above 10 GeV, $\beta \sim 1$. The Cherenkov angle θ_c is 1.4° in air for visible wavelengths and 100 kPa, and θ_c is 40.5°–42.5° in water or ice, depending on the wavelength.

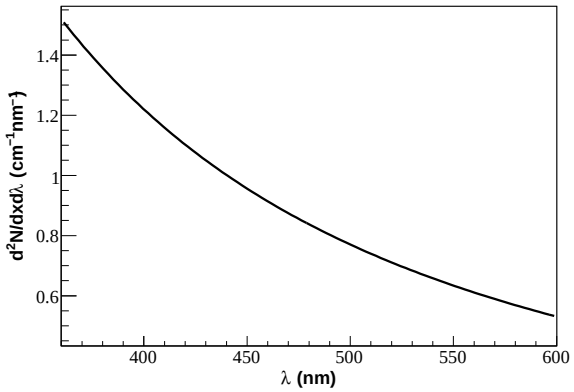

Figure 2.3: Cherenkov wavelength distribution in ice, using the index of refraction parametrization of [86].

The wavelength distribution of Cherenkov photons is given by the Franck-Tamm formula,

$$\frac{d^2N}{dxd\lambda} = \frac{2\pi\alpha}{\lambda^2}\Big(1 - \frac{1}{\beta^2 n^2(\lambda)}\Big), \tag{2.2}$$

and is weighted toward shorter wavelengths, as shown in figure 2.3. The number of expected Cherenkov photons per unit track length is found by integrating the Franck-Tamm formula over the wavelength band of interest. This number is roughly 210 photons per centimeter in ice for the wavelength band 365 nm – 600 nm, with the upper wavelength bound imposed by ice transparency [87], and a practical lower bound of 365 nm due to the ultraviolet absorption of glass used to house the photon counting apparatus [88].

2.3.2 Energy Resolution Considerations

An event energy estimate is possible by measuring the amount of Cherenkov light in the detector, as more energetic events produce more secondary particles and more Cherenkov light. For electron neutrino cascades, all secondary particles are produced a short distance from the interaction vertex. When such events are fully contained within the detector, good energy resolution is possible. Energy estimation is also possible for muons, as energetic muons emit more light during stochastic energy losses, which appear as cascades along the muon track. In [84], the muon energy loss is

parametrized as

$$-\frac{dE}{dx} = a + bE, \tag{2.3}$$

with a ∼0.268 GeV/mwe (ionization) and $b \sim 4.7 \times 10^{-4}$/mwe (stochastic) for ice. Below ∼1 TeV, ionization losses dominate, making energy estimation extremely difficult. Two additional factors complicate energy measurement with muons: First, the muon stochasticity limits the energy resolution. The number and intensity of stochastic losses within the detector volume is random and variable. Finally, the muon energy estimate is not strongly correlated to the primary neutrino energy, which is the interesting quantity. The distance any muon travels to the detector is generally unknown, and energy losses en route make the muon energy estimate a lower limit of the primary neutrino energy.

2.3.3 Angular Resolution Considerations

Angular reconstruction is possible using the space-time pattern of Cherenkov light recorded by the array of optical sensors. Electron neutrino cascades are generally contained within a few mwe, which is very short compared to the dimensions necessary for a large detector. Although these cascades are asymmetric, they appear rather spherical due to photon scattering, and therefore the direction of the primary neutrino is reconstructed poorly. In contrast, TeV muons typically pass through the detector, creating tracks with a large lever arm for accurate reconstruction. The muon track is offset from the primary neutrino track by a median angular deviation parametrized [89] by

$$\Delta\psi = 0.7^\circ \times \left(\frac{\mathrm{E}_\nu}{\mathrm{TeV}}\right)^{-0.7}. \tag{2.4}$$

Long tau particle tracks and double bangs should also have good angular resolution. For neutrino astronomy, angular resolution is essential; therefore, this work focuses only on track-like events.

2.4 The Earth as a Neutrino Target

Neutrinos must interact near the detector to be observed. Upgoing neutrinos must pass through nearly the full diameter of Earth to reach the detector, while downgoing particles need only traverse the detector overburden, generally a few thousand mwe. The column depth a particle must travel through the Earth to a detector 1500 mwe below the surface of Earth is shown in figure 2.4. For the vertical upgoing direction ($\cos\theta$ ∼–1), the column depth through the Earth is sufficient to attenuate

neutrinos above ∼100 TeV. The precise column density for near-vertical neutrinos penetrating the inner core of the Earth is uncertain due to uncertainties in the inner core density and radius. Attenuation measurements of upgoing neutrinos above ∼10 TeV are expected to constrain these uncertainties [91]. The column density decreases as zenith angle becomes more horizontal, such that ∼PeV neutrinos penetrate to the detector at $\cos\theta$ ∼–0.4, and EeV neutrinos are visible above $\cos\theta$ ∼–0.05. Tau neutrinos are an exception, as secondary neutrinos produced by tau decay may still propagate to the detector, allowing observation of PeV – EeV tau neutrinos from steeply upgoing zenith angles. For downgoing zenith angles $\cos\theta > 0.05$, the column depth becomes less than maximal muon ranges. Since neutrino-induced muon fluxes increase from the surface until an equilibrium is reached between muons ranging out and charged-current muon neutrino interactions producing muons, downgoing zenith angles may not have sufficient column depth to reach this equilibrium and subsequently have smaller neutrino-induced muon fluxes. Additionally, muons from cosmic ray air showers are able to reach the detector at downgoing zenith angles.

2.5 The Background from Cosmic Ray Air Showers

Downgoing muons from cosmic ray air showers penetrate to the detector for $\cos\theta > 0.05$ and dominate muons from neutrino charged current interactions, increasing the background of track-like events by several orders of magnitude. This background limits sensitivity to neutrino-induced muon tracks to the upgoing zenith range $\cos\theta < 0.05$. Two techniques are under development to extend sensitivity to $\cos\theta > 0.05$. The first uses energy cuts and searches for ∼PeV neutrinos [92], since the cosmic ray muon background is much smaller at those energies. Another technique searches for neutrino-induced muons starting within the detector, rejecting the cosmic ray muon background passing completely through, and should be sensitive at ∼TeV neutrino energies. The remaining chapters focus on neutrino astronomy for only the upgoing region $\cos\theta < 0.05$.

While the zenith range $\cos\theta < 0.05$ is free from cosmic ray muons, the neutrinos from cosmic ray air showers easily penetrate to the detector. This atmospheric neutrino background presents the greatest challenge to TeV neutrino astronomy in the upgoing zenith range. Astrophysical sources can be distinguished from this background by searching for spatial excesses comparable to the detector resolution. Additionally, astrophysical neutrino sources with energy spectra $\sim E^{-2}$ would produce

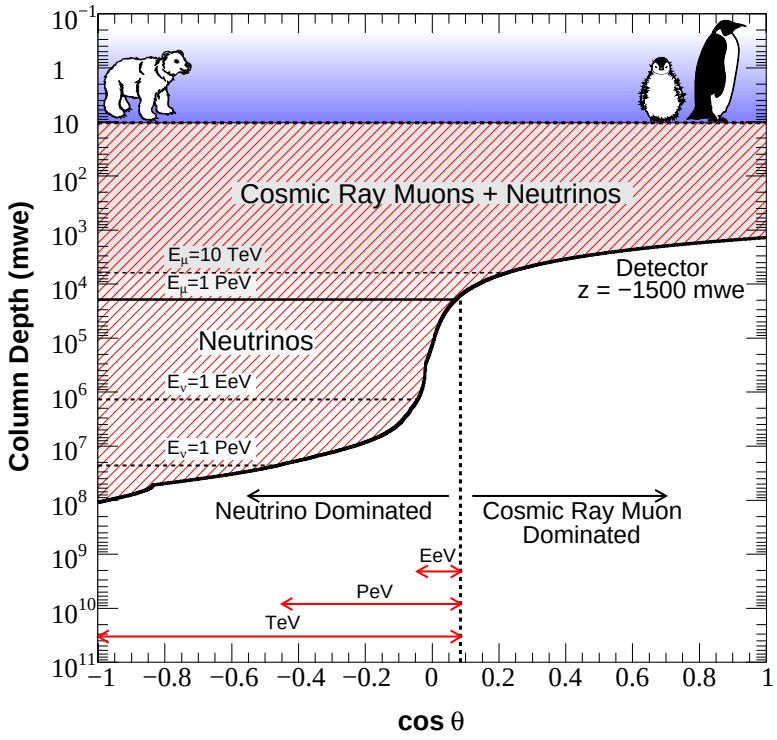

Figure 2.4: Column penetration for muons and neutrinos as a function of zenith angle for a detector 1500 mwe below the surface. Earth column density is calculated from the Preliminary Reference Earth Model [90].

excesses at high energy relative to $\sim E^{-3.7}$ atmospheric neutrinos. The method used to identify these excesses is described in chapter 6 and represents a significant portion of this work. Many sources are additionally expected to exhibit time-dependent fluxes. Such time dependence provides additional power to identify these sources, and methods including time dependence are described in appendix B.

Chapter 3

The AMANDA Cherenkov Telescope

The Antarctic Muon And Neutrino Detector Array (AMANDA) is a large optical Cherenkov detector built in the ice sheet at the geographic South Pole. AMANDA has been designed with the intent of observing high energy astrophysical neutrinos, or at minimum proving the concept of in-ice optical Cherenkov detection and paving the way for a larger detector.

3.1 In-Ice Array

The main component of AMANDA is an array of photosensitive modules frozen beneath the ice sheet. The array (figure 3.1) consists of 677 optical modules arranged in 19 vertical strings, which roughly form a vertical cylinder of 200 m diameter. Most optical modules lie in the region from 1500 m to 2000 m below the ice surface.

Installation of each string consists of first drilling a hole through the firn, roughly the first 50 m, with a closed circulation of hot ($\sim 90^{\circ}$C) water. Drilling of the underlying ice then commences with an open circulation of hot water, possible because the ice, unlike the firn, retains the water well created. The string of optical modules is lowered into the water when drilling is complete, with each module installed in-turn on the main cable as it descends. The strings freeze into place within a few days. A significant fraction of modules ($\sim$7%) do not survive installation/refreeze and are lost. The inner ten strings, dubbed AMANDA-B10, were installed by early 1997. The AMANDA-II detector was completed by early 2000 with nine final strings.

Each string contains roughly 40 optical modules. The main component in each module is an 8 inch Hamamatsu R5912-2 photomultiplier tube (PMT) with a bialkali photocathode, which performs

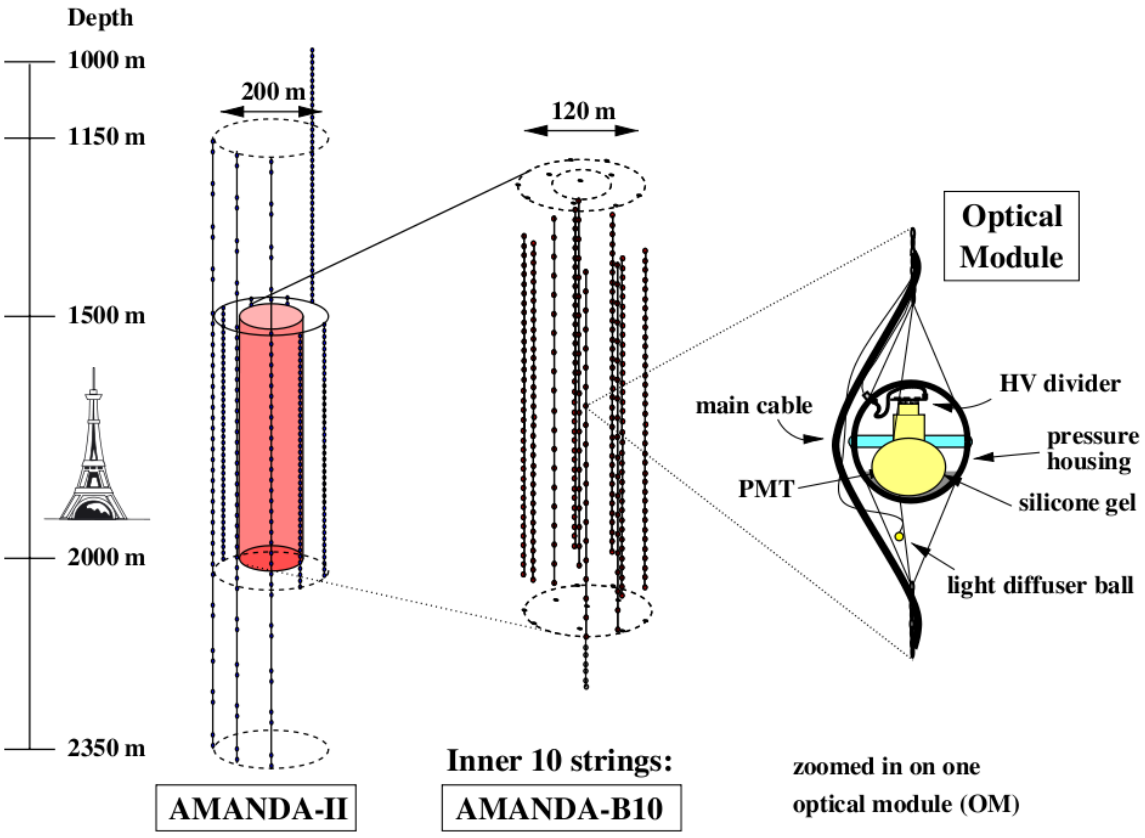

Figure 3.1: The AMANDA-II in-ice array and optical module, from [93].

with ∼20% quantum efficiency and a timing resolution of <5 ns. The PMT is optically coupled to a 30 cm glass pressure sphere housing using silicone gel. The main cable provides high voltage to each module, divided by internal circuitry and providing the appropriate voltage to each PMT dynode. Each module has an individual set voltage, and the voltages are tuned to provide a gain of $\sim 10^9$ for all modules in the array. The main cable also provides analog transmission of PMT signals to the surface via coax, twisted pair, and analog-optical channels. String-18 [94], unlike the remainder of the array, has remote data acquisition electronics in each module and communicates digitally to the surface. This string was designed as a prototype for IceCube [95] optical modules and data transmission.

3.2 Muon-DAQ

The AMANDA muon-DAQ system is illustrated in figure 3.2. PMT pulses from electrical channels are first amplified, then fed to a discriminator. The pulse is also sent to a peak-sensing ADC through a 2 μs delay. Pulses in analog-optical channels are converted to electrical and are routed similarly to discriminators and ADCs. For all channels, the discriminator fires when the channel pulse amplitude exceeds the discriminator threshold (a "hit"), and the discriminator output signal is fed to a TDC and the trigger. The vast majority of hits are optical noise, produced by ^{40}K decay in the glass PMT face and pressure sphere. The trigger logic, the main component of the DMADD (Digital Multiplicity ADder-Discriminator) module, provides triggers according to the following specifications:

- 24-fold multiplicity trigger, when 24 modules register hits within 2.5 μs.
- String trigger, requiring a set multiplicity from the same string. This trigger, designed to retain low multiplicity events and thus low energy muons, requires hits in 6 modules from inner strings 1-4 or hits in 7 modules from strings 5-19 within 2.5 μs.

When the trigger fires, a digitization signal is sent to the bank of ADCs, which digitize the pulse peak amplitudes. A stop signal is sent to the TDC bank through a 10 μs delay. Each TDC records the times of both positive and negative edges for a maximum of eight successive threshold crossings, and the time over threshold (TOT) for each pulse can be calculated. The ADC and TDC banks are

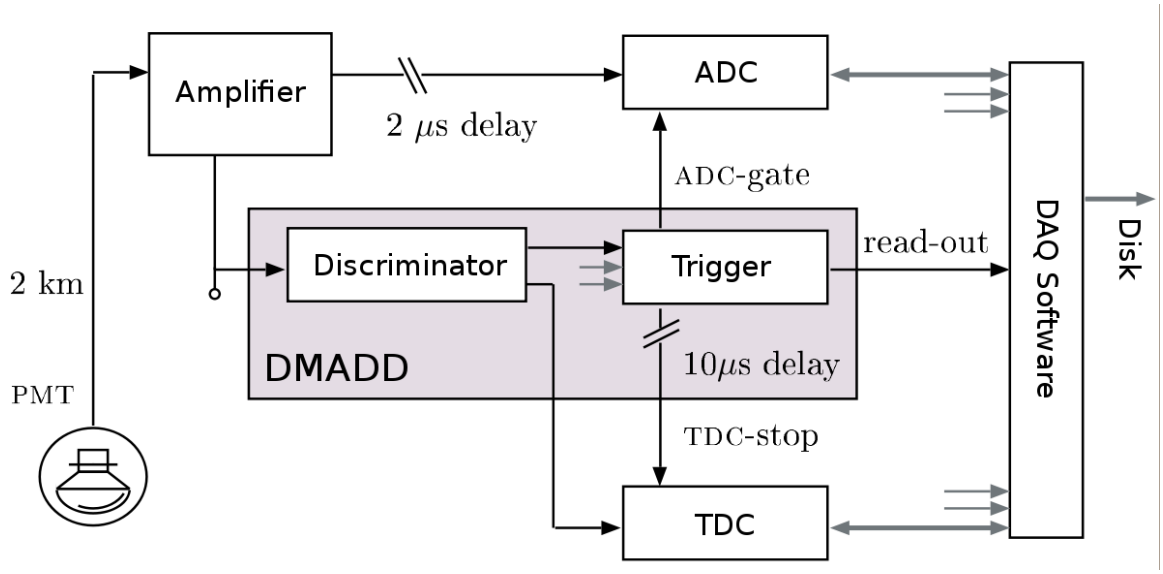

Figure 3.2: Schematic of the AMANDA muon-DAQ, adapted from [97].

read out along with the trigger. The hit and trigger times are calibrated to GMT time and stored on disk. The process of triggering, reading, and clearing the DAQ components requires ∼2 ms, during which the detector cannot record another event. An illustration of the data obtained is shown in figure 3.3. A more advanced data acquisition system was installed in early 2003 [96], providing full PMT waveforms and operation without deadtime; however, data from this system is not discussed further.

3.3 Calibration

An accurate understanding of detector relative timing and geometry are critical since muon reconstruction is based on these quantities. Each channel has a specific cable and electronics propagation time delay. These delays are measured by injecting light at known times with a surface laser through an optical fiber, which has a known optical propagation delay, to modules in the array. The calibration is of the form

$$t = t_{raw} - T_0 - \frac{\alpha}{\sqrt{A}}, \tag{3.1}$$

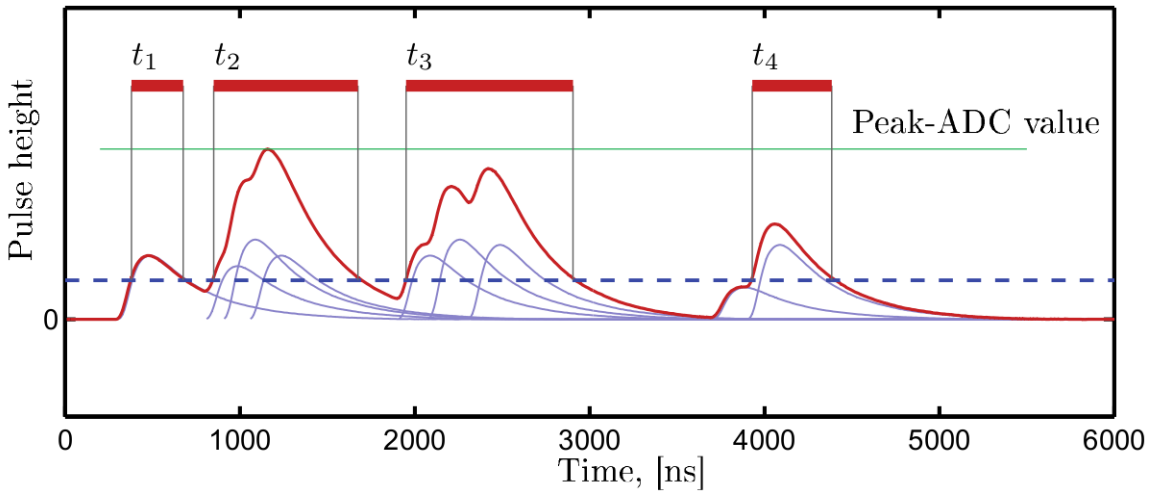

Figure 3.3: Illustration of the data available from the AMANDA muon-DAQ, from [97]. For each hit module, we record the overall peak ADC value and the times of positive and negative edges for up to eight discriminator crossings. The red curve represents the sum of several individual PMT pulses.

where T_0 is the main correction factor and $\alpha/\sqrt{A}$ is an amplitude-dependent factor necessary due to pulse distortion. Systematic uncertainty in the calibration adds to the PMT jitter and results in ∼15 ns end-to-end timing uncertainty. Accurate surveys of (x,y) coordinates for each string are recorded during deployment. The z position of each module on the string is determined by a combination of the known position along the main cable and the depth of the bottom of the string, determined by pressure readings at the end of deployment. These measurements are improved using laser pulses, since the distance of a module to a light source is known:

$$d = (t_{rcv} - t_{emit}) \times \frac{c}{n_{ice}}, \tag{3.2}$$

where t_{rcv} and t_{emit} are the reception and emission times of the light pulse, respectively, and n_{ice} is the group index of refraction of South Pole ice.

3.4 Properties of South Pole Ice

Cherenkov photons produced by relativistic leptons propagate through ice before reaching optical modules. The photons propagate at a velocity c/n_g, where n_g is the group index of refraction, which varies from 1.38 at 337 nm to 1.33 at 532 nm [86]. The ice within the detector volume is composed of two general categories: Undisturbed glacial ice and hole ice.

3.4.1 Glacial Ice at the South Pole

Measurements show that the glacial ice at the South Pole is distinctly layered, with nearly an order of magnitude variation in scattering and absorption coefficient as a function of depth [87], shown in figure 3.4. This depth dependence is due to the time-variable accumulation of dust onto the glacier surface, sinking deeper into the glacier with time as more snows accumulate. High resolution studies of this ice [98] reveal individual explosive volcanic events. Above 1400 m, scattering from bubbles within the ice becomes increasingly significant, rendering this region less useful for Cherenkov detection. Below 1400 m, time and pressure have transformed these bubbles into air hydrate crystals, making the ice significantly more transparent.

3.4.2 Hole Ice

As water refreezes within holes after string deployment, the ice formed is significantly different from the bulk of the ice. Scattering and absorption are constant with depth due to mixing. More importantly, refreezing forces air out of the water, forming bubbles and significantly increasing scattering. The effective scattering coefficient for hole ice is not well-measured, but may be 50 cm or less.

3.5 Simulation

An accurate simulation of AMANDA is required to understand the detector response to muon and neutrino fluxes over a wide energy range, thereby quantifying the event expectations of meaningful neutrino signal hypotheses. We simulate fluxes of muon and tau neutrinos with ANIS [99], using the CTEQ5 [100] structure functions and Preliminary Reference Earth Model [90]. Muons produced by ANIS are propagated with MMC [84], which simulates muon decay and stochastic losses.

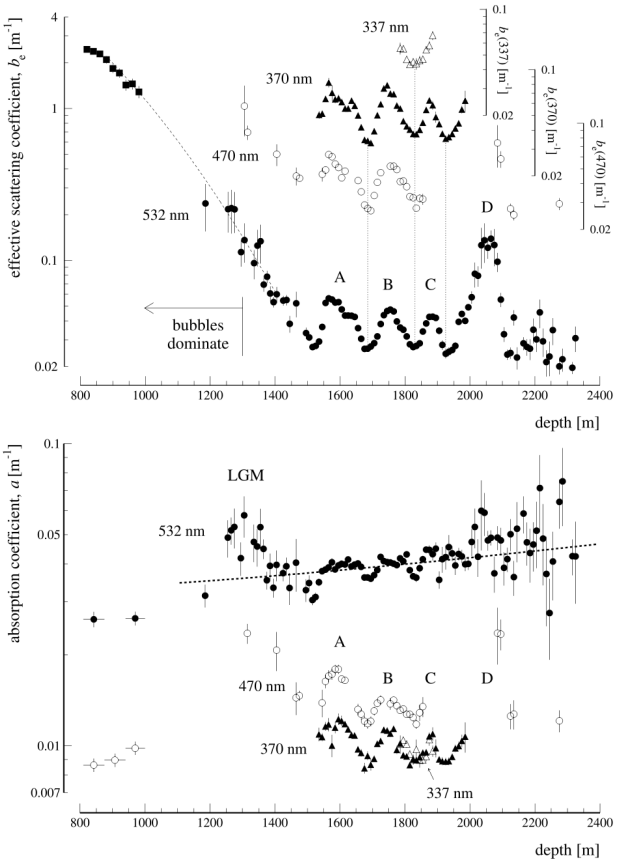

Figure 3.4: Scattering coefficient (top) and absorption coefficient (bottom) of South Pole ice as a function of depth (from [87]), showing scattering/absorption peaks A-D.

Cherenkov light produced by muons and cascades near the detector is simulated by PTD. Using a photon Monte Carlo, photon densities are tabulated in terms of radial distance from the muon track (or cascade axis), z distance along the axis, time, and PMT orientation. The simulation does not account for depth-dependent ice properties, and instead assumes the following scattering properties of the bulk ice, obtained by matching event rate and timing distributions with downgoing muon tracks:

$$\begin{aligned} \lambda_{scat}^{eff} &= 21 \text{ m} \\ < \cos\theta_{scat} > &= 0.85 \end{aligned}$$

Absorption is modeled with wavelength dependence, with a typical absorption length of $\lambda_a = \sim$100 m. Hole ice is simulated with a scattering length of $\lambda_{scat}^{eff} = 50$ cm. Photonics [101], a newer ice simulation which includes layering, is now used. The detector simulation AMASIM [102] uses these photon density tables; photon hits in optical modules and the hit timing are determined by Monte Carlo. For tracks with multiple muons or muons with stochastic losses and resulting cascades within the detector, photon densities are summed appropriately. Cosmic ray air showers are also simulated using CORSIKA [103], and resulting muons are propagated through the same simulation chain using MMC and AMASIM.

Chapter 4

Data Selection and Event Reconstruction

4.1 Data Selection

The raw AMANDA muon-DAQ data returned from the South Pole are mostly downgoing muons from cosmic ray air showers, which are recorded at a rate of ∼80 Hz, with only a few neutrino-induced muon events per day. The data is filled with problematic periods corresponding to hardware glitches, including power outages, HV failures, DAQ failures, etc. Similarly, a large fraction of the optical modules experience transient problems or are simply dead. Such unstable time periods and optical modules reduce our ability to properly simulate the detector and assess livetime, both of which are critical to evaluate the detector response to a simulated neutrino flux, so this bad data must be removed. The most sensitive stability indicator is the individual dark noise rates of all optical modules. This noise rate is measured for each module by counting hits from triggered events which occur well before the trigger time, and thus are not likely to have been produced by the event causing the trigger. For 2005 and 2006, a reasonable time window is ∼0 – 7000 ns (TDC < 7000), shown in figure 4.1. The number of total hits within this time window for typical 10 minute AMANDA runs should follow a Poisson distribution, and the noise rate for each optical module (OM) is given by $\mathcal{R} = \frac{N_{hit}}{N_{trig} \cdot 7\mu s}$. Obvious non-Poissonian structure is visible in a 2-D noise rate histogram of OM vs. time for 2005, shown in figure 4.2.

For 2000-2004, stability cuts have been developed to remove unstable periods, using the number of OMs outside of a noise rate range 83 Hz $< \mathcal{R} <$ 8.3 kHz as a stability indicator. OMs have been removed using cuts on both the number of files with noise rates outside the above range and the

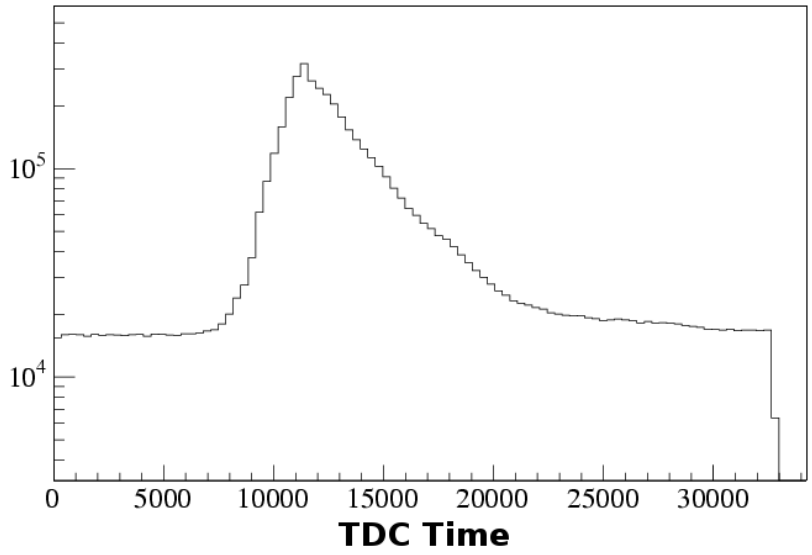

Figure 4.1: TDC time distribution of hits for triggered events during AMANDA run 9363 in 2005. One TDC unit is ∼1 ns. The peak near 11,000 is comprised mostly of hits from muons.

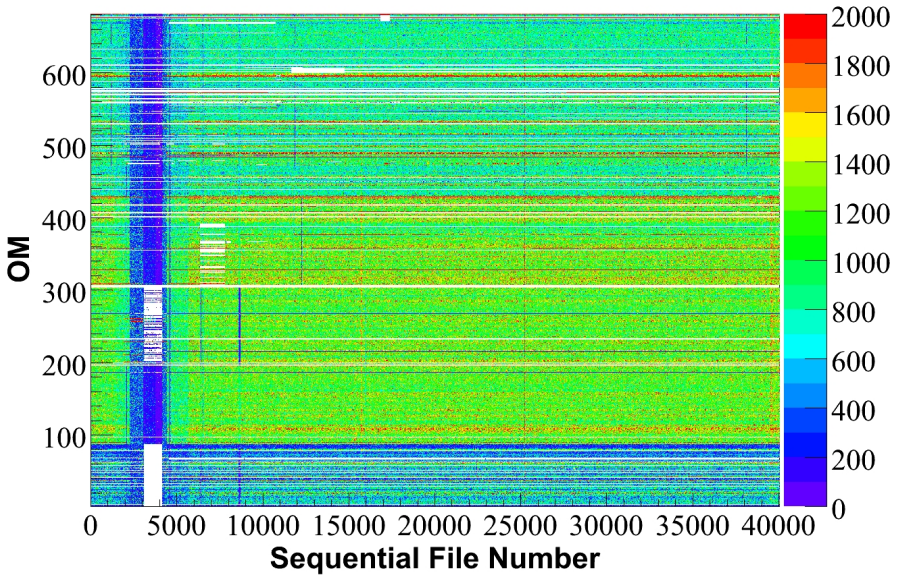

Figure 4.2: 2005 Noise rate matrix of OM vs. sequential raw data file.

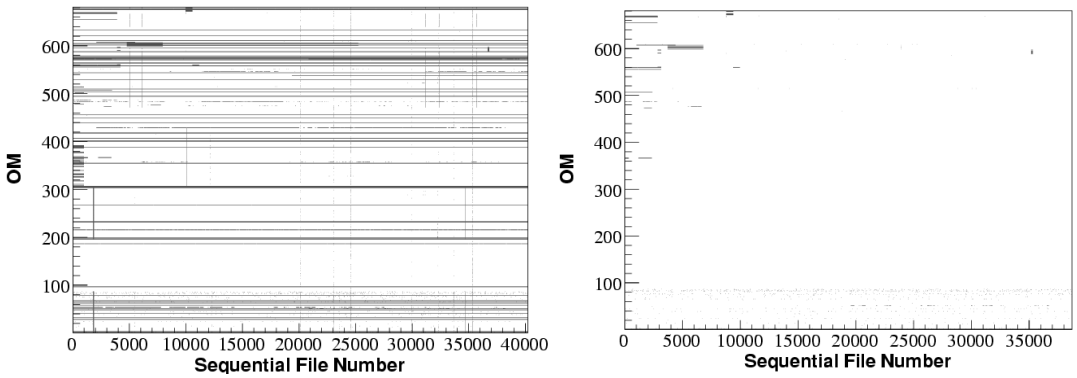

Figure 4.3: Matrix of 2005 data quality before (left) and after (right) quality cuts are applied. Black regions indicate noise rates below 83 Hz or above 8.3 kHz.

RMS fluctuation of the noise rate [104]. However, since problematic files and problematic OMs are correlated, a better way to do the filtering is to remove the most unstable OM or file and recompute the stability of the remaining OMs and files, then repeat the process until the data shows acceptable stability. This procedure has been performed on the 2005 and 2006 AMANDA data using a log-likelihood approach, using the following parameters as a measure of stability:

$$\mathcal{Q}_f = -\frac{1}{N_{OM}} \sum_{i=1}^{N_{OM}} \log[P(\mathcal{R}| < \mathcal{R} >)] \tag{4.1}$$

$$\mathcal{Q}_{OM} = -\frac{1}{N_f} \sum_{i=1}^{N_f} \log[P(\mathcal{R}| < \mathcal{R} >)], \tag{4.2}$$

where $\mathcal{Q}_f$ and $\mathcal{Q}_{OM}$ are the file and OM quality, N_{OM} is the number of remaining optical modules, N_f is the number of remaining files, and $< \mathcal{R} >$ is the mean noise rate for the given OM. The OM or file with the highest value of $\mathcal{Q}$ is removed and $\mathcal{Q}$ is recomputed until further removal would cause the loss of an unacceptably large fraction of data. A matrix of data quality is shown for 2005 in figure 4.3 both before and after the quality cut is applied.

Also, we remove a large portion of data during the austral summer when significant maintenance is performed on the detector, roughly from November 1 to February 15 of each year. Additionally, we remove a subset of optical modules with either problematic calibration (OMs 81-86) or a location away from the core of the detector (the top and bottom of strings 11-13 and string 17). Finally, the first IceCube strings have been deployed near AMANDA in early 2005 and early

2006. Calibration of these strings requires using optical flashers; thus, we remove AMANDA events occurring during this flashing activity.

4.2 Hit Selection

Each event is composed of a number of photon hits in optical modules. These hits generally fall into one of three categories:

- Hits caused by Cherenkov radiation from energetic particles within the detector.
- Hits from PMT dark noise.
- Hits from detector artifacts.

We are interested in reconstructing tracks and cascades using the timing distribution of hits from the first category. Hits from the second and third categories have pathological timing distributions and significantly impair our reconstruction ability, thus they must be removed. The hit selection for muon tracks differs from the selection for other analyses including cascade and monopole searches, etc., and several hit selections are performed in parallel during filtering using the Sieglinde [105] software suite. The cut procedure for muon tracks is as follows:

- Poor quality hits with amplitude outside the range $0.1 < \text{ADC} < 1000$ or time over threshold outside an OM-specific range are removed.
- Hits falling outside a time window of $4500 \text{ ns} < t < 11500 \text{ ns}$ are removed.
- Hits without another hit within 100 m and 500 ns are removed.
- Hits induced by electrical crosstalk are removed.

The second and third cuts eliminate the majority of dark noise hits. Electrical crosstalk mostly affects OMs on strings 5 – 10 with communication to the surface on twisted pair cables. The crosstalk cut is performed in two steps. First, crosstalk hits usually have a large amplitude without a correspondingly large time over threshold. For each affected OM, this ADC-TOT response is characterized as shown in figure 4.4, and a crosstalk cut is made. Additionally, crosstalk effects are measured by identifying large amplitude hits and recording the resulting crosstalk hits in nearby channels, which occur in discrete

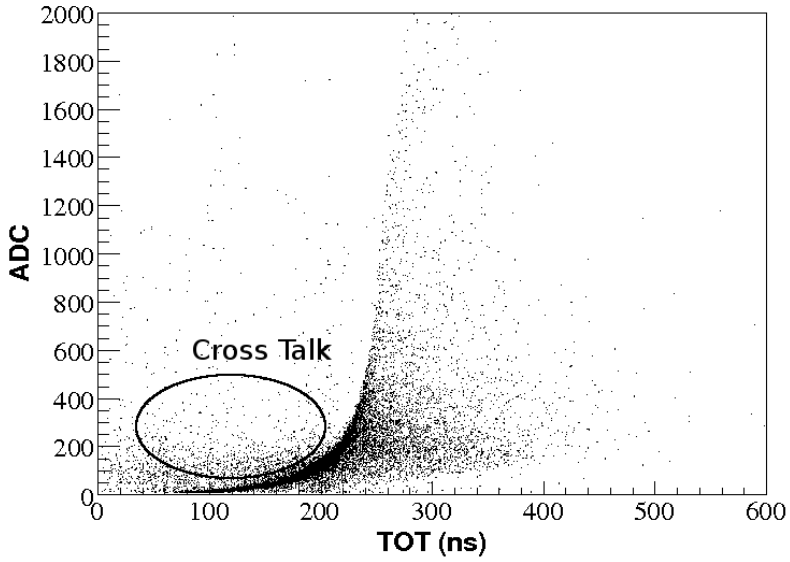

Figure 4.4: Identification of crosstalk in ADC vs. TOT distributions for OM 246 during run 9453 in 2005.

time windows relative to the large amplitude hit. A map of time windows for each problematic talker-receiver channel combination is generated and used to reduce crosstalk. The data is retriggered after hit selection, and events not passing the multiplicity trigger or string trigger criteria are removed.

4.3 Track Reconstruction

The remaining hits are mostly produced by Cherenkov radiation from energetic particles within the detector. The Cherenkov photons propagate outward from the particle track, forming a cone with angle $\sim 41^\circ$ as illustrated in figure 4.5. For a module a distance d from the muon track, the expected arrival time of Cherenkov photons emitted at time $t_\circ$ is

$$t_{exp} = t_\circ + \frac{d \cdot \cot \theta_c}{c}. \tag{4.3}$$

At distances greater then $\sim 1 - 2$ effective scattering lengths from the muon track, the photon flux is smaller than expected from absorption alone because scattering confines photons to the region near the track. Photons reaching such distances are delayed by the scattering, and a useful quantity is

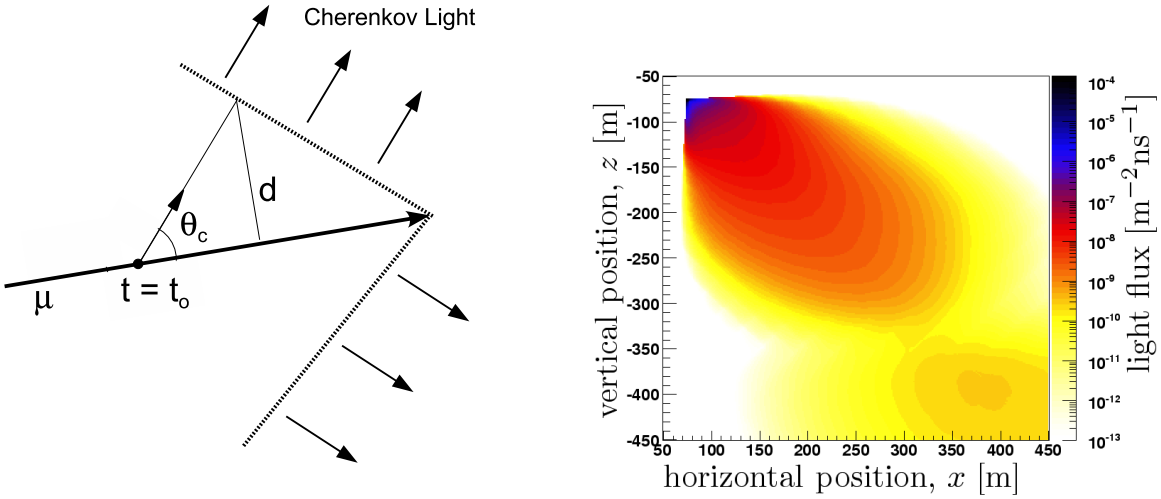

Figure 4.5: Depiction of the Cherenkov cone produced by a relativistic muon (left), and an instantaneous snapshot of the simulated Cherenkov light flux produced by a relativistic muon in ice traveling to the upper left at $\theta = 135°$ (right), from [101]. The Cherenkov cone is visible in the top left of the image.

relative arrival time or time residual,

$$t_{res} = t - t_{exp}. \tag{4.4}$$

Typical time residuals are larger in regions of ice with shorter scattering lengths due to higher concentrations of imperfections.

4.3.1 Unbiased Likelihood Reconstruction

Given a muon track hypothesis, distances of hits from the track and thus expected Cherenkov photon arrival times are known; therefore, the time residual for each hit can be computed as described above. If the likelihood of observing a given time residual is known as a function of distance d from a hypothesis track for each of the N hits comprising the event, a likelihood can be formulated given the track zenith (θ), azimuth (ϕ), and vertex ($\mathbf{r}$):

$$\mathcal{L}(\theta, \phi, \mathbf{r}) = \prod_{i=1}^{N} P(t_{res,i} | d_i(\theta, \phi, \mathbf{r})). \tag{4.5}$$

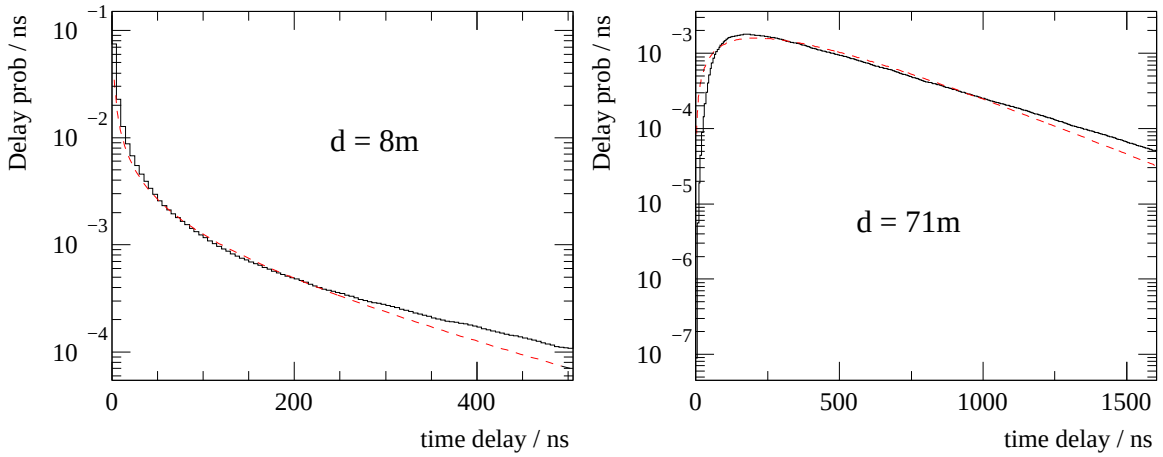

Figure 4.6: Time residual distribution from a photon Monte Carlo (black) and Pandel function (red) for 8 m and 71 m from the muon track, from [93].

Track hypotheses can be ranked by this likelihood, and this formulation can then be used to determine the best reconstructed track. The time residual distributions $P(t_{res}|d)$ can be determined by a photon Monte Carlo including scattering and absorption. Alternatively, a more convenient approach is the Pandel function [106], an analytic solution of the photon time residual probability as a function of distance from the muon track for media with significant absorption and scattering:

$$P(t_{res}|d) = \frac{\tau^{-(d/\lambda)} \cdot t_{res}^{(d/\lambda-1)}}{N(d) \cdot \Gamma(d/\lambda)} \cdot e^{-\left(t_{res} \cdot \left(\frac{1}{\tau} + \frac{c}{n_g \cdot \lambda_a}\right) + \frac{d}{\lambda_a}\right)}, \tag{4.6}$$

$$N(d) = e^{-d/\lambda_a} \cdot \left(1 + \frac{\tau \cdot c}{n_g \cdot \lambda_a}\right)^{-d/\lambda}. \tag{4.7}$$

Comparison with simulation yields a best fit to the free parameters: $\tau = 557$ ns, $\lambda = 33.3$ m, and $\lambda_a = 98$ m for typical AMANDA ice, shown in figure 4.6. PMT signals in AMANDA have an end-to-end leading edge timing uncertainty of $\sim$15 ns, and this timing uncertainty is convoluted with the Pandel function t_{res} distributions used in reconstruction [93]. The quantity $-\log \mathcal{L}$ is minimized numerically with respect to the track free parameters θ, ϕ, and $\mathbf{r}$, yielding a best fit track hypothesis. Dispersion limits the ability to separate consecutive hits in AMANDA to $\sim$100 ns and $\sim$10 ns for electrical and optical channels, respectively [93], so many photons are often are combined with the first hit. Any hits in a given OM subsequent to the first provide much less information for reconstruction and are disregarded. If many photons are observed in a given module, the first arrives sooner than

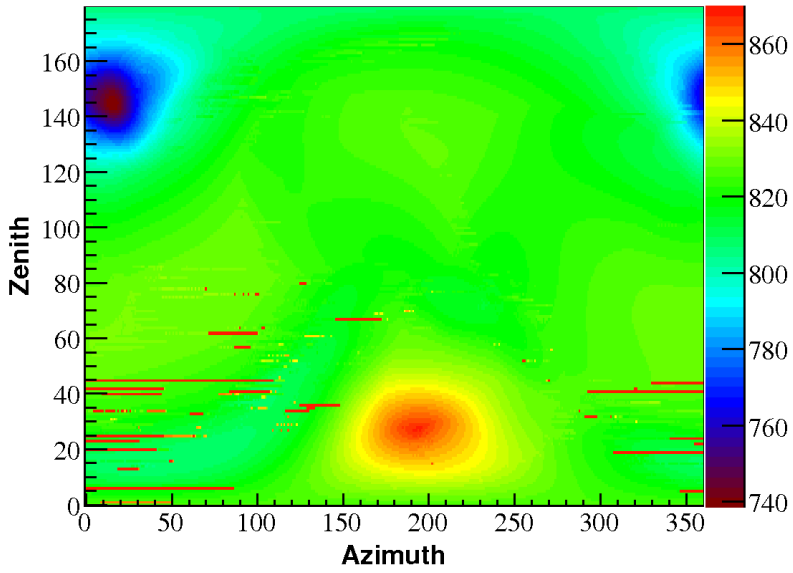

Figure 4.7: Pandel likelihood map of $-\log\mathcal{L}$ for upgoing event 7442798 in run 9490 of 2005. The minimum is at zenith 145.1°, azimuth 17.45°.

expected since, on average, the first photon is less scattered. Using only the timing information of this first photon introduces a mild pathology in the reconstruction of high energy events, which may yield many photons in any given OM. This effect can be corrected by calculating the time residual distribution for only the first photon, given N total photons observed in the optical module [93]:

$$P_1(t_{res}|d) = N \cdot P(t_{res}|d) \cdot \left(\int_{t_{res}}^{\infty} P(t|d)dt \right)^{(N-1)}. \tag{4.8}$$

This multi-photoelectron probability is currently computationally intensive and not used for this analysis, although efforts are underway to improve speed for use in IceCube analysis. Figure 4.7 displays $-\log\mathcal{L}$ for an event with respect to zenith and azimuth, fitting only the track vertex $\mathbf{r}$ at each grid point. The event is clearly upgoing, with minimum $-\log\mathcal{L}$ at zenith 145.1°, azimuth 17.4°. The fit fails to find the true minimum at a portion of grid points for this event, especially at small zenith angles, due to the complexity of the likelihood space. The detector display of this event along with the best fit muon track are shown in figure 4.8. To increase the probability of locating the true minimum, the minimization is repeated 32 times with different starting values for θ, ϕ, and $\mathbf{r}$. Two of the seeds come from the best track using the Direct Walk and JAMS algorithms, described in section

4.3.4.

4.3.2 Paraboloid Reconstruction

For point source searches, knowing the angular resolution of obtained events is critical. The ability to reconstruct muon tracks in AMANDA partially depends on event topology. A muon track passing through a larger portion of the detector or hitting a larger number of modules should, on average, reconstruct with better angular resolution due to a longer lever-arm or larger number of constraining parameters, respectively. Angular resolution can be determined on an event-by-event basis by examining the likelihood space in the vicinity of the best fit track [107]. As the zenith and azimuth coordinates (θ, ϕ) are forced away from the best fit values ($\hat{\theta}$, $\hat{\phi}$), the quantity $-\log\mathcal{L}$ increases parabolically from its minimum as shown in figure 4.7. The likelihood ratio $-2\cdot\log\left(\frac{\mathcal{L}(\theta,\phi)}{\mathcal{L}(\hat{\theta},\hat{\phi})}\right)$ is evaluated on a grid of zenith and azimuth near the best fit, and the resulting values are fit to a paraboloid with the form

$$-2\cdot\log\left(\frac{\mathcal{L}(\theta,\phi)}{\mathcal{L}(\hat{\theta},\hat{\phi})}\right)=\frac{x^2}{\sigma_x^2}+\frac{y^2}{\sigma_y^2}, \tag{4.9}$$

where the x and y axes are fit and do not necessarily correspond to zenith and azimuth. Likelihood ratio contours enclosing the minimum are chi-square distributed and contain the true direction with confidence $-2\cdot\log\left(\frac{\mathcal{L}(\theta,\phi)}{\mathcal{L}(\hat{\theta},\hat{\phi})}\right)\sim\chi_2^2$. Specifically, the $-2\cdot\log\left(\frac{\mathcal{L}(\theta,\phi)}{\mathcal{L}(\hat{\theta},\hat{\phi})}\right)=1$ contour would enclose the true direction in 39.3% of trials. The paraboloid fit is a convenient approximation of the likelihood space, summing the complex map of $-2\cdot\log\left(\frac{\mathcal{L}(\theta,\phi)}{\mathcal{L}(\hat{\theta},\hat{\phi})}\right)$ into three values: σ_x, σ_y, and an axis rotation angle. The corresponding track direction probability density estimate can be obtained from the fit by:

$$\frac{\mathcal{L}(\theta,\phi)}{\mathcal{L}(\hat{\theta},\hat{\phi})}=\frac{e^{-\left(\frac{x^2}{2\sigma_x^2}+\frac{y^2}{2\sigma_y^2}\right)}}{2\pi\sigma_x\sigma_y}. \tag{4.10}$$

4.3.3 Forced Downgoing (Bayesian) Reconstruction

Poor quality downgoing muon events often are misreconstructed as upgoing. Since the number of downgoing events outnumber the upgoing neutrino events by a factor of $\sim10^6$, a fraction of misreconstructed downgoing events easily overwhelms the much smaller neutrino sample. One method to remove such events is to reconstruct each as downgoing, and then compare the downgoing likelihood with the likelihood of the best fit track hypothesis. The downgoing fit is performed in the same

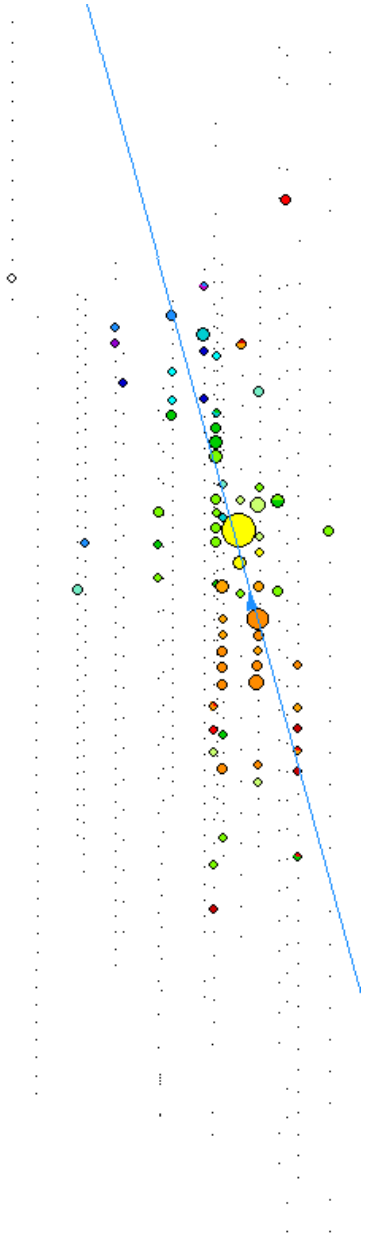

Figure 4.8: Detector display for event 7442798 in run 9490 of 2005. Hit timing is indicated by the color pattern, with red and blue indicating first and last hits, respectively. The event is clearly an upgoing muon with a track similar to the shown best fit.

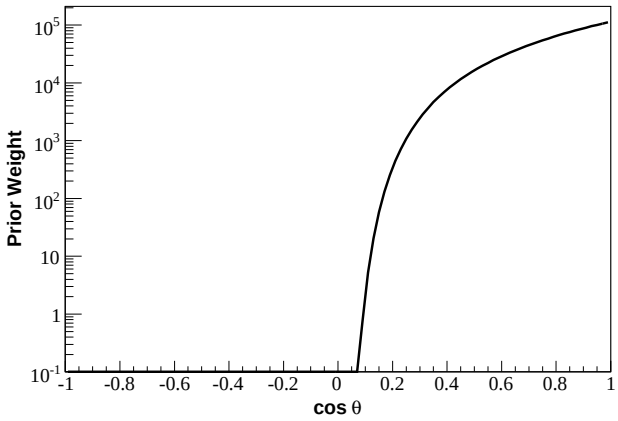

Figure 4.9: Zenith prior applied to the likelihood function during Bayesian reconstruction.

manner as the single-photoelectron likelihood reconstruction, except track zenith is weighted in the likelihood function by a prior function describing the zenith distribution of downgoing muons, shown in figure 4.9. The reconstruction is repeated 64 times with different starting values for θ and ϕ. The best downgoing track likelihood is compared with the best fit likelihood:

$$Q_{Bayesian} = -\log\Big(\frac{\mathcal{L}(\hat{\theta}_{down}, \hat{\phi}_{down})}{\mathcal{L}(\hat{\theta}, \hat{\phi})}\Big). \tag{4.11}$$

Good upgoing tracks have large values of $Q_{Bayesian}$ since these tracks are not very compatible with a downgoing hypothesis. Misreconstructed downgoing tracks generally have smaller values of $Q_{Bayesian}$.

4.3.4 First Guess Algorithms

While the likelihood methods above yield the best angular resolution, it is computationally not practical to apply a likelihood reconstruction to all of the $O(10^9)$ events recorded by AMANDA each year. Also, the likelihood reconstruction is sensitive to the initial track hypothesis. For these reasons, we first apply quick, less accurate reconstruction methods, and later we use the results as a filter for interesting tracks and as seeds for likelihood reconstruction.

4.3.4.1 Direct Walk

Direct Walk is a pattern matching algorithm which identifies tracks using pairs of hits connected by nearly the speed of light (track elements) [93]. Track elements are selected if the following is satisfied:

$$|\Delta t| < \frac{d}{c} + 30 \text{ ns}; \qquad d > 50 \text{ m}, \tag{4.12}$$

where d is the distance between the hit OMs. For each track element, we next identify and count the number of other hits associated with the track element according to the following:

$$-30 \text{ ns} < t_{res} < 300 \text{ ns}; \qquad r < 25 \text{ m} \cdot (t_{res} + 30)^{1/4}, \tag{4.13}$$

where r is the distance of closest approach between the track and hit module. High quality track elements are selected by requiring at least 10 associated hits and an RMS distance along the track between the track vertex and closest approach to each associated hit greater than 20 m. If multiple high quality track elements are identified, a cluster search is performed to find the track with the most other tracks within 15°, and the final track is the average of the tracks within the cluster.

4.3.4.2 JAMS

JAMS is a pattern matching algorithm similar to Direct Walk [108]. For a large number of track zenith and azimuth hypotheses, we examine each hit for clustering neighbors according to

$$\sqrt{(\Delta r)^2 + (\Delta z - c\Delta t)^2} < r_{max}. \tag{4.14}$$

Δz and Δr are the distances between the hits along and perpendicular to the track direction, respectively, Δt is the hit time difference, and r_{max} is an arbitrary threshold. A minimum cluster size of 7 hits is required to keep the track. Each passing track is refined with a simplified log likelihood reconstruction and then ranked using a neural network. The input parameters include the number of negative and very large time residuals, and the number of hits >50 m from the track. The final track is the track with the highest neural net quality.

Chapter 5

Event Selection

As illustrated in figure 5.1, AMANDA records $O(10^9)$ events per year, mostly from muons produced by cosmic ray air showers. Of these, $O(10^3)$ are upgoing muons produced by atmospheric neutrinos, and AMANDA records at most $O(10)$ high quality events per year from extraterrestrial sources with E^{-2} energy spectra given current limits [26]. We attempt to isolate these neutrino events from the downward muon background in a computationally efficient manner.

5.1 Data Sets

After accounting for deadtime in data acquisition electronics, nominally ∼15% of uptime, we have accumulated 1387 days (3.8 years) of livetime with 1.29×10^{10} events during seven years of operation (table 5.1). A detector simulation is necessary to optimize the selection of high energy neutrino-induced muon events. We simulate neutrino events using the software chain described in

Year	Livetime	Total Events	Filtered Events	Final Selection
2000	197 d	1.37 B	1.63 M	596
2001	193 d	2.00 B	1.90 M	854
2002	204 d	1.91 B	2.10 M	1009
2003	213 d	1.86 B	2.22 M	1069
2004	194 d	1.72 B	2.09 M	998
2005	199 d	2.06 B	5.21 M	1019
2006	187 d	2.00 B	4.89 M	1050
Total	1387 d	12.92 B	20.04 M	6595

Table 5.1: AMANDA livetime and event totals.

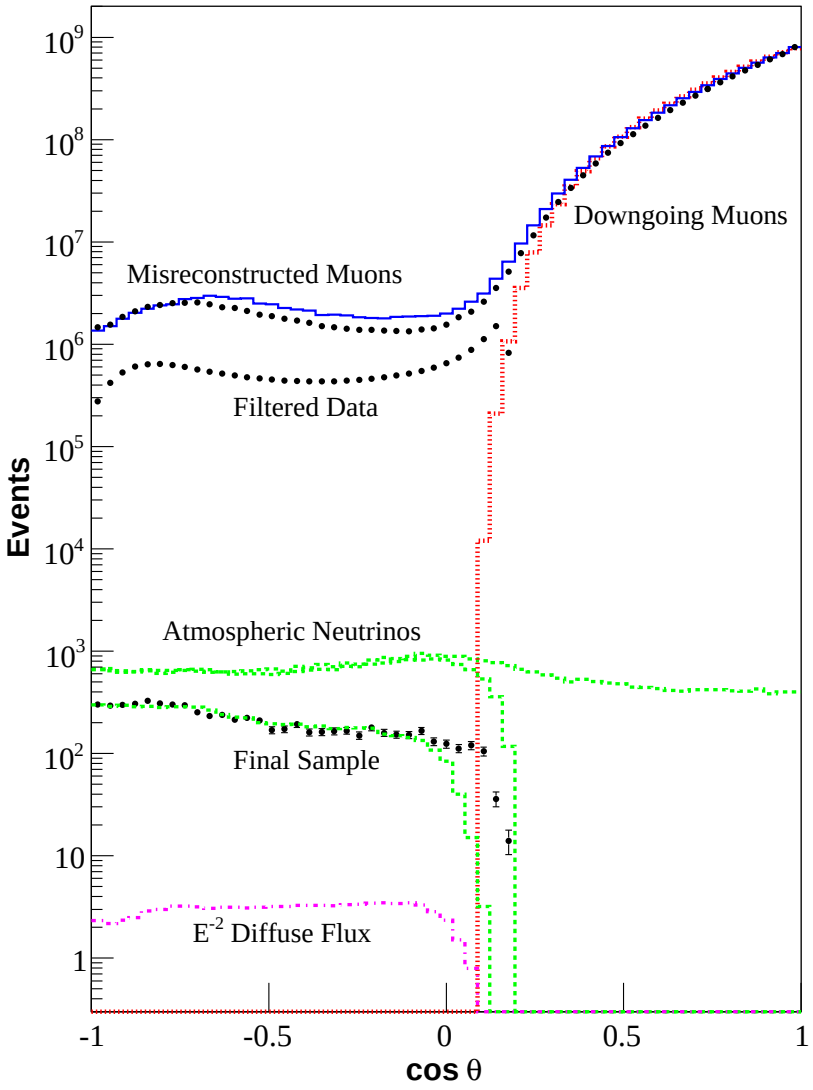

Figure 5.1: Zenith angle (θ) distributions for data and simulation at several reduction levels. Reconstructed (solid) and true (fine dotted) zenith angle distributions are shown for CORSIKA [103] cosmic ray muon simulation at retrigger level, and reconstructed zenith angle distributions are shown for atmospheric neutrino simulation (dotted) and data (circles) at retrigger level, filter level, and final selection. We also show the reconstructed zenith angle distribution of a diffuse E^{-2} neutrino flux at the current limit [26] using our final selection (dash-dotted).

chapter 3. Each year is simulated with a specific detector configuration to account for changes and upgrades which occur during the austral summer. We have generated 9×10^5 events per year for ν_μ fluxes following an E^{-1} energy spectrum, with a zenith angle distribution uniform in cos θ from $80^\circ < \theta < 180^\circ$. An event selection sensitive to track-like events is also sensitive to muons produced by tau decay and even tau tracks at PeV – EeV energies; thus, we have generated similar ν_τ fluxes. We have also generated 2×10^6 muon neutrino events per year equally divided into 20 narrow declination bands, each separated by five degrees, to simulate point sources. The weighting of simulated events to real fluxes is described in appendix A. Finally, we have generated $\sim1\times10^{10}$ cosmic ray air showers with CORSIKA [103], used to understand the rejection of background cosmic ray muons.

The event selection is carried out in two phases: First, we apply reconstructions and filter well-reconstructed downgoing cosmic ray muon events using the Sieglinde [105] software suite. We then perform the more challenging task of removing cosmic ray muon events wrongly reconstructed as upgoing. Simulated events are filtered identically to the data.

5.2 Filtering Downgoing Events

For neutrino analysis, the first task is removing the well-reconstructed downgoing muons which dominate our data, which is a computationally intensive process. The AMANDA raw muon-DAQ data comprises roughly 2 TB per year. Each year of data contains ∼60,000 files, each with ∼25,000 events. Each file is processed by Sieglinde [105] according to the following procedure.

5.2.1 Retriggering

After hit cleaning (chapter 4), an event may no longer satisfy the 24-module multiplicity or string trigger thresholds. Such events are removed to preserve agreement with Monte Carlo. This retrigger removes roughly 50% of events.

5.2.2 First Guess Reconstruction

Events satisfying the retrigger condition are then reconstructed with the JAMS and DirectWalk (DW) algorithms, described in chapter 4. The data has been filtered in two separate blocks, 2000-2004 and 2005-2006, with slightly different event selection strategies. For 2000-2004, our upgoing

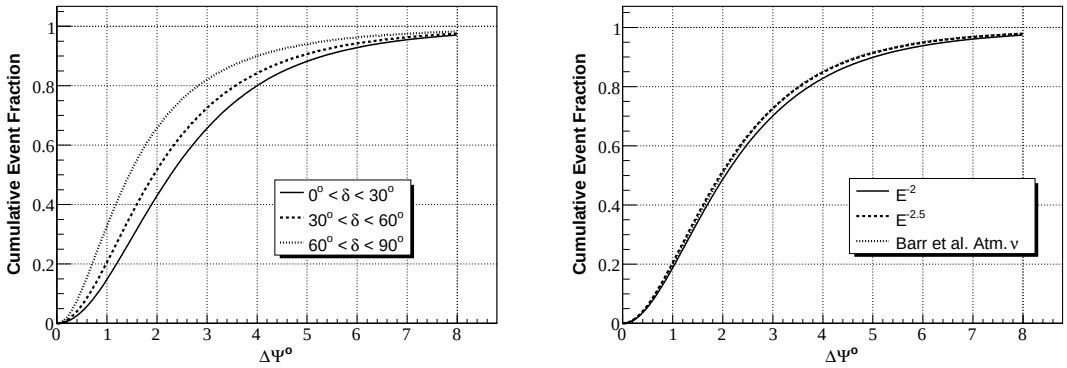

Figure 5.2: Angular deviation between neutrino and UL fit track for simulated E^{-2} muon neutrino events from several declination ranges (left) and energy distributions (right).

event selection requires zenith angles $\theta_{DW} > 70°$ and $\theta_{JAMS} > 80°$. The cuts are interchanged for 2005 and 2006, requiring $\theta_{JAMS} > 70°$ and $\theta_{DW} > 80°$.

5.2.3 Unbiased Likelihood Reconstruction

The computationally intensive 32-iteration unbiased likelihood (UL) reconstruction is then applied to surviving events (∼1% of triggered events). The median accuracy of the UL fit is 1.5° – 2.5°, shown in figure 5.2. With the additional cut $\theta_{UL} > 80°$, our upgoing event filter reduces the downward muon background by nearly a factor of 1000 relative to trigger level (table 5.1). Events passing the filter are reconstructed with the 64-iteration Bayesian likelihood (BL) and paraboloid reconstructions.

5.3 Final Event Selection

Several million misreconstructed downgoing muons pass through the filter, still outnumbering upgoing atmospheric neutrinos by a factor of 1000 (figure 5.1). We remove these misreconstructed events by applying topological criteria designed to select quality muon tracks. The criteria we use are the following:

- The $Q_{Bayesian}$ likelihood ratio of the UL and BL fits, described in chapter 4. High values of

log(UL/BL) select upgoing events.

- The angular uncertainty of the UL fit, from the paraboloid reconstruction. Misreconstructed events generally have large angular uncertainty.

- The *smoothness*, or homogeneity of the hit distribution along the UL track [93]. High quality events contain photon hits along the entire length of the track and have smoothness values near zero, whereas hits from misreconstructed events tend to distribute near the beginning or end of the track and have smoothness values near +1 and −1, respectively.

- The UL track *direct length*, obtained by projecting *direct hits* backward to the UL track at the Cherenkov angle and taking the distance along the track between the first and last. We select direct hits, compatible with relatively unscattered photons and arriving on-time with the Cherenkov cone, using the time window -15 ns $< \; t - t_{ch} \; <$ 25 ns [93]. Hits from misreconstructed events rarely follow the muon-Cherenkov timing pattern over significant distances, resulting in short lengths.

We select zenith angle dependent cuts using these parameters, assuming our signal is a neutrino point source with an E^{-2} energy spectrum. The cuts are optimized to minimize the model rejection factor [109], resulting in the best possible sensitivity to neutrino fluxes. For the zenith angle region $91.5^\circ < \theta < 180^\circ$, the cuts are (figure 5.3):

$$\begin{aligned} \log(\text{UL/BL})\ (Q_{Bayesian}) &> 34 - 25 \cdot \Phi(\cos\theta + 0.15) \\ \text{Angular uncertainty } \sqrt{\sigma_x \cdot \sigma_y} &< 3.2 - 4 \cdot \Phi(-\cos\theta - 0.75) \\ |\text{Smoothness}| &< 0.36. \end{aligned}$$

Here $\Phi(x) = x$ for positive x, and $\Phi(x) = 0$ for $x < 0$. We use a support vector machine (SVM) [110] trained on the above parameters to improve event selection in the near-horizontal region $80^\circ < \theta < 91.5^\circ$. The SVM output is a quality parameter, which is ∼1 for signal-like events and ∼-1 for background-like events. We apply the following cut on this quality parameter:

$$\text{SVM Parameter} \quad > \quad 1.0 - 12.08 \cdot \Phi(\cos\theta - 0.023).$$

Application of these quality cuts yields 6595 neutrino candidate events [111] (figure 5.6).

Simulated atmospheric neutrino fluxes [69, 70] agree with data in track quality parameter distributions and zenith angle (figure 5.5) up to a normalization factor within uncertainties on at-

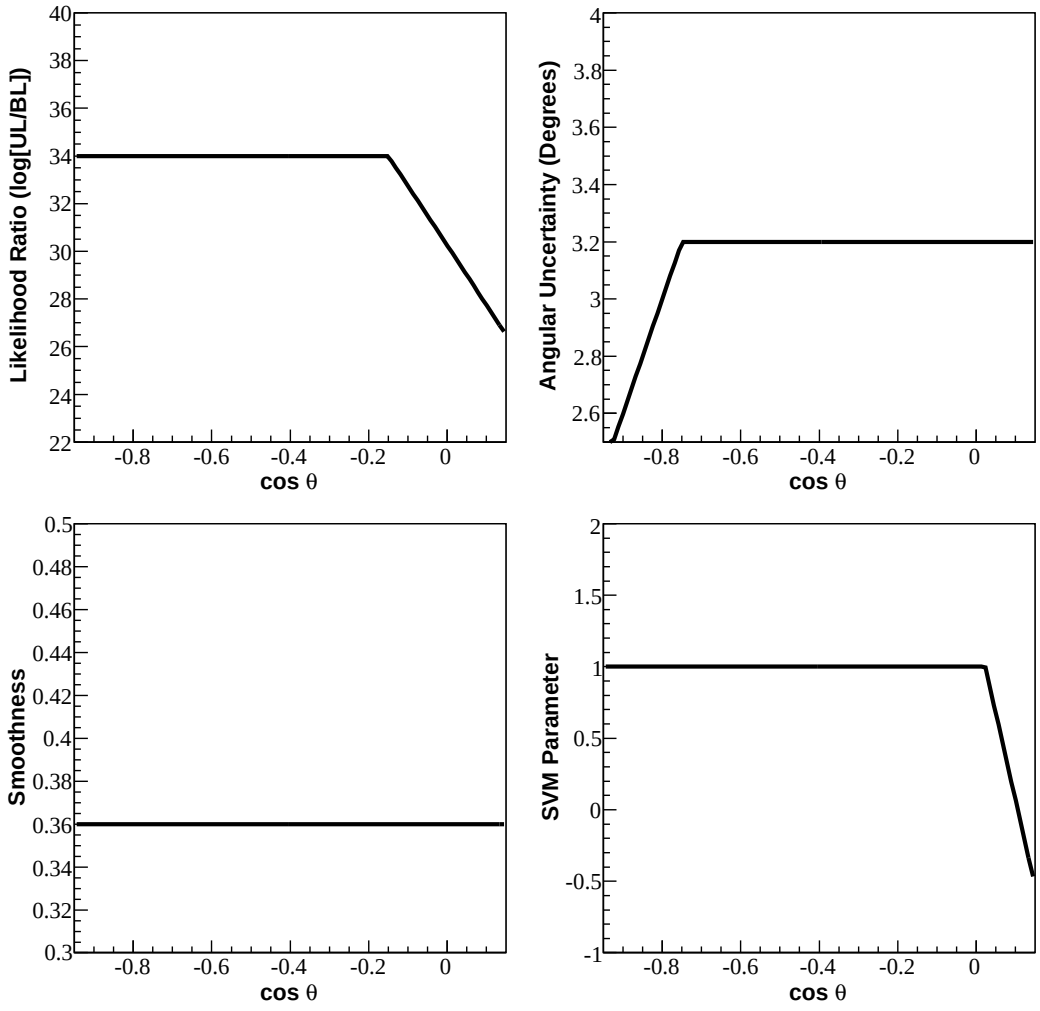

Figure 5.3: Zenith (θ) dependent final cuts for $91.5^\circ < \theta < 180^\circ$ (top and left), and $80^\circ < \theta < 91.5^\circ$ (bottom right).

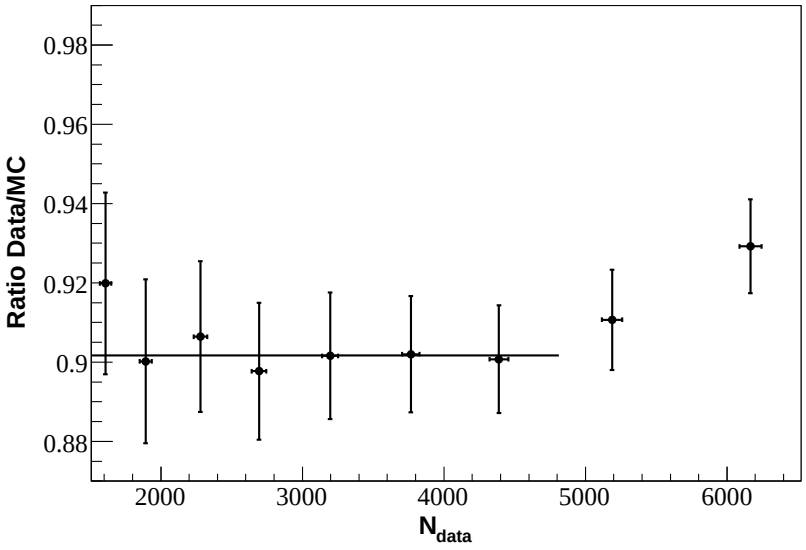

Figure 5.4: Ratio of data to simulated atmospheric neutrinos [69] as a function of cut tightness. As cuts tighten, reducing the number of data and simulated atmospheric neutrino events, the ratio stabilizes ∼3% lower than the value with optimal cuts and ∼6100 data events.

mospheric neutrino flux. Application of the filter selection and final quality cuts to this simulation yields an atmospheric neutrino efficiency of 30% relative to retrigger level for $\theta > 90°$. The contribution of misreconstructed downward muons, estimated by tightening quality cuts until a very pure atmospheric neutrino sample is obtained, is less than ∼3% for $\theta > 95°$ (declination $\delta > 5°$), shown in figure 5.4. Misreconstructed muons are more significant near the equator and dominate events in the Southern Sky. Evaluation of simulated events retained by the final cuts provides the neutrino effective area, described in appendix A, shown in figure 5.7 for neutrino energies from 10 GeV to 100 PeV. The simulation is later used to provide flux limits for neutrino point sources.

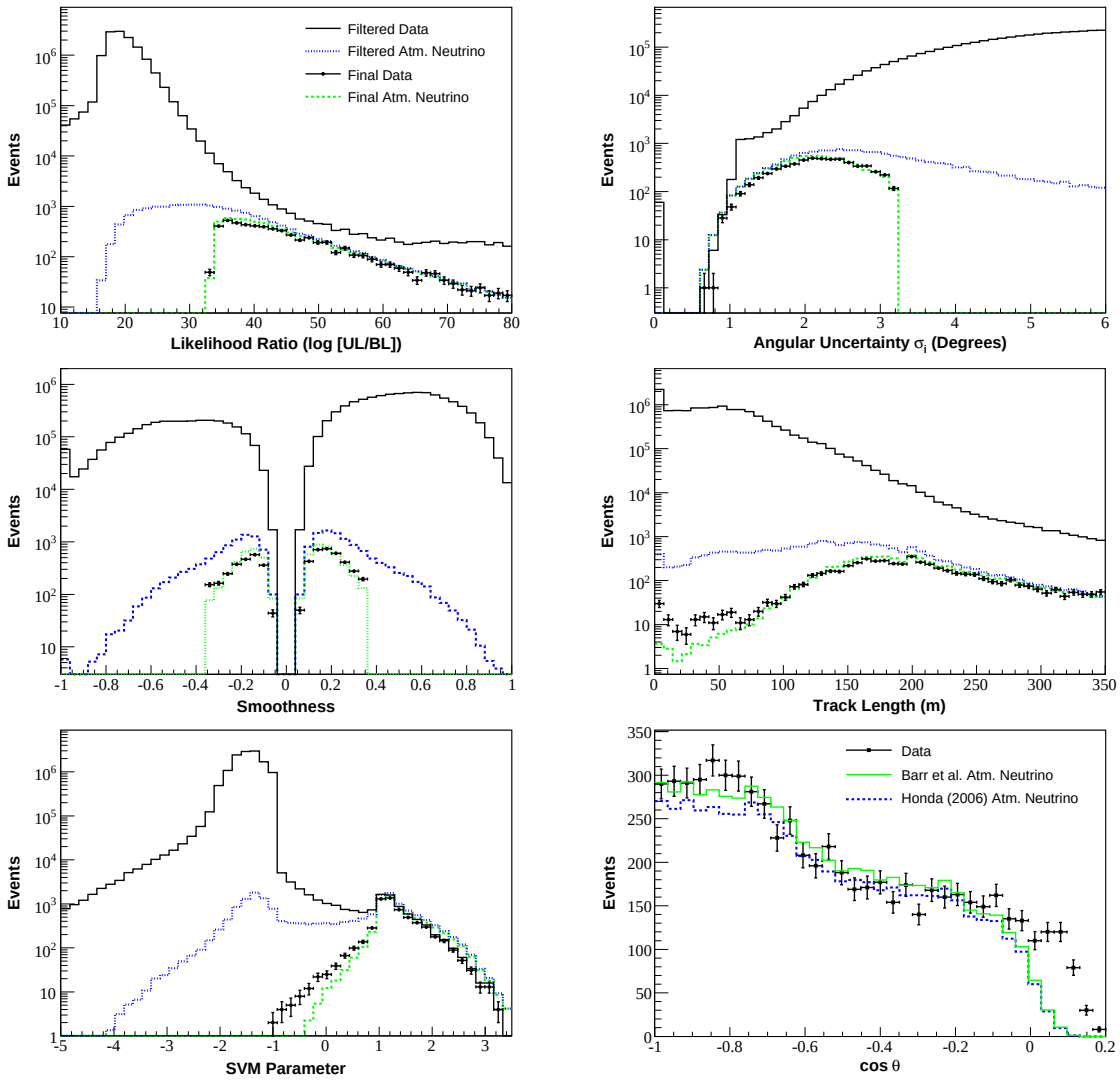

Figure 5.5: Distributions of data and atmospheric neutrinos at filter level and final selection level for several parameters and zenith angles $\theta > 95°$ (top and left), and zenith angle distribution for the selected 6595 neutrino candidate events compared with model predictions [69, 70] for atmospheric neutrinos (bottom right).

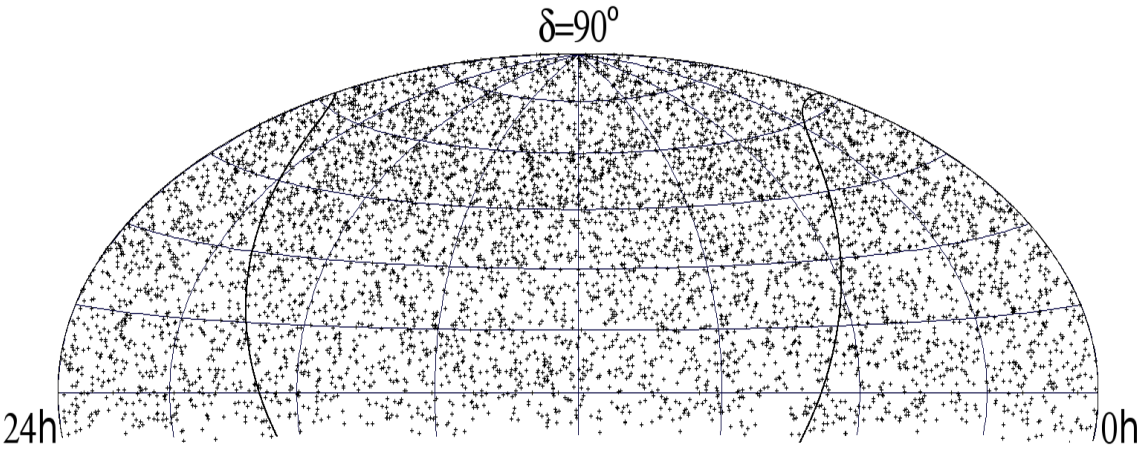

Figure 5.6: Equatorial sky map of final 6595 events recorded by AMANDA-II from 2000–2006.

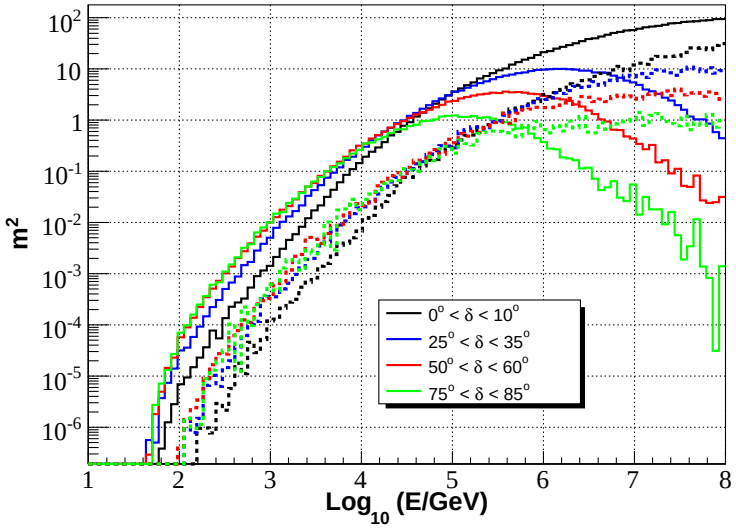

Figure 5.7: Effective area for averaged ν_μ and $\bar{\nu}_\mu$ (solid) and averaged ν_τ and $\bar{\nu}_\tau$ (dashed) neutrino fluxes for several declination ranges.

Chapter 6

Search Method

No TeV neutrino sources have yet been observed. We therefore use discovery-oriented statistical methods to separate any small neutrino point source signal in our data from the atmospheric neutrino background. To maximize the potential for discovery, we must use all relevant information from the data in our analysis. Several features distinguish point source signals from the background:

- The event angular distribution. Signal events would cluster around the direction of the neutrino source with a deviation from the true direction dependent on the detector angular resolution.
- The event energy distribution. The differential energy spectrum of the signal expected from Fermi acceleration mechanisms is close to E^{-2}, harder than that of atmospheric neutrinos, as shown in figure 6.1. The differential spectrum of atmospheric neutrinos approximately follows a power law of $E^{-3.7}$ above $\sim$1 TeV.
- The event time distribution. Signal events would be distributed nonuniformly in time from sources which are periodic, flaring, or one-time bursts. The atmospheric neutrino event rate is generally constant over time.

The most straightforward way to incorporate this information into a search method is through a *binned* search, using an angular bin with radius comparable to the detector angular resolution to select events. A neutrino source would produce an event excess above the atmospheric neutrino background event expectation for the bin, with a significance given by binomial statistics. Additional cuts may be used to select energetic events or, in the case of time dependence, events within a time

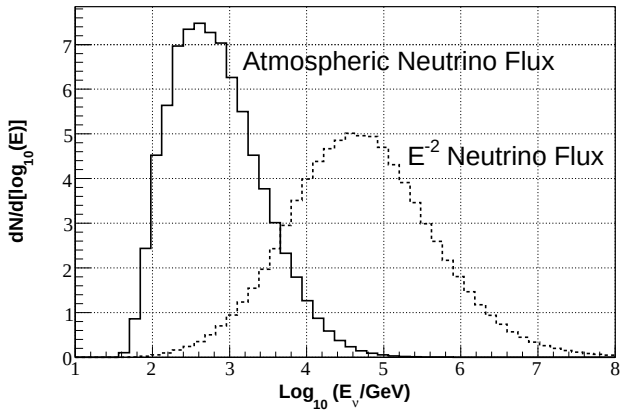

Figure 6.1: Energy distribution of events passing selection criteria for simulated atmospheric neutrino background [69] in a 3.5° bin and an E^{-2} point source with flux $\Phi_{\nu_\mu+\nu_\tau} = 10^{-10}$ TeV cm^{-2} s^{-1}. Such a source would be detected at 5σ in approximately 40% of trials.

window to reduce the background and increase the probability that a given neutrino flux will be significant. Two general problems reduce the performance of binned methods:

1. **The information reduction problem**: All of the event information is reduced to a binary classification; either the event passes the cuts and is counted, or it does not. Information is lost that alternatively could indicate the relative agreement of each event with a neutrino point source signal or background. For example, events at the edge of a search bin are not as indicative of a point source as events near the center, but are counted the same. More importantly, muon events with energies above the cut threshold are counted the same; however, since the spectra of an E^{-2} signal and the atmospheric neutrino background differ by $\sim E^{1.7}$, muons with energy well above the cut threshold are orders of magnitude more compatible with a point source signal than with background.

2. **The optimization problem**: The cuts, including the angular bin radius, must be optimized given a specific point source signal hypothesis. If the hypothesis does not accurately describe the signal, the cuts may not be optimal. Additionally, the cuts which optimize sensitivity [109]

(i.e. set the best limits) do not maximize the probability of discovering a signal, and therefore a choice must be made to sacrifice either sensitivity or discovery potential.

We avoid these problems entirely by using a maximum-likelihood search method [112], incorporating event angular and energy information on an event-by-event basis. Similar methods have been proposed [113, 114, 115]. In appendix B we expand this method to include time information for sources with time-dependent fluxes.

6.1 Maximum Likelihood Search Method

At any direction in the portion of the sky observed by AMANDA, the data can be modeled by two hypotheses:

- H_0: The data consists solely of background atmospheric neutrino events, i.e. the null hypothesis.
- H_S: The data consists of atmospheric neutrino events as well as astrophysical neutrino events produced by a source with some strength and energy spectrum.

If H_0 and H_S are described by probability density functions (PDFs) over parameters from the data, the likelihood of obtaining the data is calculable given either hypothesis. We use a likelihood ratio test with the standard log-likelihood test statistic

$$\lambda = -2 \log \left[\frac{P(\text{Data}|H_0)}{P(\text{Data}|H_S)} \right]. \tag{6.1}$$

Larger values of λ indicate the data is less compatible with the background hypothesis H_0. The PDFs $P(\text{Data}|H_0)$ and $P(\text{Data}|H_S)$ are calculated using knowledge of the spatial and energy distribution of events from background and simulated neutrino point sources.

6.1.1 Confidence Level and Power of a Test

The utility of a statistical test is measured by the rate of type-I and type-II errors (α and β), known respectively as the confidence level (CL) and power (1 - β) of the test:

- **Type-I Error**: H_0 is rejected when H_0 is true, i.e. a false discovery claim.
- **Type-II Error**: H_0 is not rejected when H_0 is false.

A tradeoff exists between CL and power, and reducing the probability of false discovery necessarily reduces the power to discover any signal present in the data. The accepted CL threshold necessary to claim a discovery is generally 5σ, a false discovery rate of 5.73×10^{-7}, and a weaker 3σ result (2.7×10^{-3}) may be considered evidence of a signal. At a given CL, power is dependent on the strength of the signal; weaker signals are less likely to be detected. The flux necessary to reach a given level of power (e.g. 50%, 90%) at a given CL is the discovery potential, a figure of merit for the search. Finally, 1σ (68%) and 90% CL are often used as uncertainty bounds on the physical parameters of H_S.

6.1.2 Search Method

We consider a search method for neutrino emission from a fixed point in the sky $\vec{x}_s$ using the set of 6595 AMANDA muon events. Each muon event has an energy estimate and a reconstructed position $\vec{x}_i$, separated from the source position by an angular distance $\Psi_i = |\vec{x}_i - \vec{x}_s|$. The signal PDF describes the likelihood of observing the event energy estimate and angular separation Ψ_i given a point source at position $\vec{x}_s$, and is a product of spatial and energy likelihood terms:

$$\mathcal{S}_i = \mathcal{L}(\Psi_i) \times \mathcal{L}(\mathrm{E}_i). \tag{6.2}$$

6.1.2.1 Spatial Likelihood

Each event has an angular uncertainty about the best fit position $\vec{x}_i$ related to the event topology (section 4.3.2), and we incorporate this angular uncertainty into the analysis. We use the paraboloid reconstruction angular uncertainties, σ_x and σ_y, in a circularized fashion:

$$\sigma_i = \sqrt{\sigma_x \cdot \sigma_y}. \tag{6.3}$$

The angular error estimate σ_i is an accurate approximation of the much more complex reconstruction likelihood space, shown for example in figure 4.7. The spatial PDF is the relative likelihood of the true track direction being $\vec{x}_s$, given both the angular distance Ψ_i from the event best fit and event angular uncertainty σ_i, which is a normalized two-dimensional Gaussian:

$$\mathcal{L}(\Psi_i) = \frac{1}{2\pi\sigma_i^2} e^{-\frac{\Psi_i^2}{2\sigma_i^2}}. \tag{6.4}$$

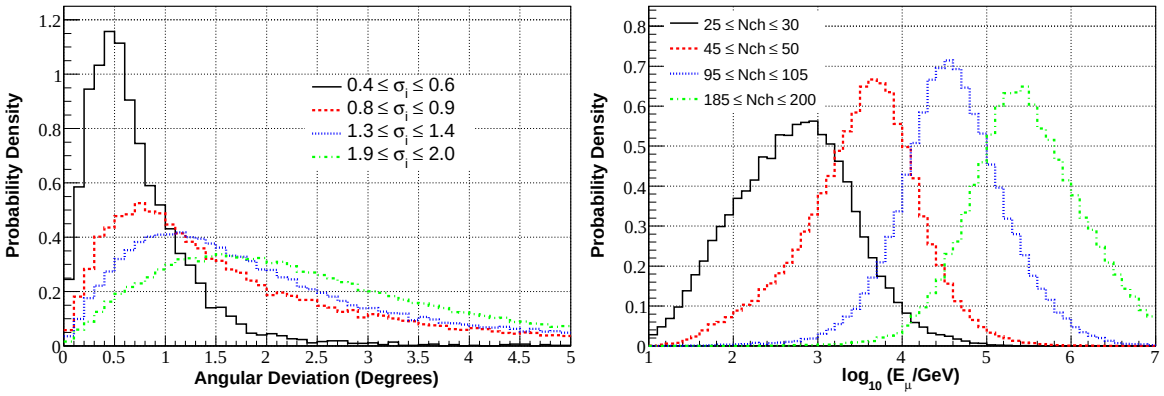

Figure 6.2: Distributions of angular deviation between true and reconstructed tracks for simulated neutrino-induced muon events over several ranges of estimated angular uncertainty (left), and muon energy distributions for four ranges of Nch (right).

Distributions of the angular deviation between true and reconstructed tracks of simulated muons in figure 6.2 show the correlation between estimated angular uncertainty and track reconstruction error.

6.1.2.2 Energy Likelihood

The amount of light deposited in the detector depends strongly on muon energy above ∼1 TeV, and the number of hit modules (Nch) provides an approximate measure of event energy. Distributions of muon energy for several ranges of Nch are shown in figure 6.2. As an energy estimator, Nch yields a 1σ uncertainty in $\log_{10}(\mathrm{E}_\mu)$ of 0.65. Astrophysical neutrino spectra are assumed to follow a power law $\mathrm{E}^{-\gamma}$ with $\gamma\sim2$, so the meaningful quantity is the likelihood of obtaining the event Nch value (Nch_i) given a spectral index. This energy PDF is

$$\mathcal{L}(\mathrm{E}_i) = P(\mathrm{Nch}_i|\gamma) = \int_{\mathrm{E}_\mu}\int_{\mathrm{E}_\nu} P(\mathrm{Nch}_i|\mathrm{E}_\mu)P(\mathrm{E}_\mu|\mathrm{E}_\nu)P(\mathrm{E}_\nu|\gamma)d\mathrm{E}_\nu d\mathrm{E}_\mu. \tag{6.5}$$

The convolution is done by the neutrino simulation. Nch distributions of any spectral index are produced by weighting the simulation according to the spectral index (appendix A). From these simulations, we tabulate Nch probabilities for spectral indices $1 \leq \gamma \leq 4$ and for atmospheric neutrinos [69] in bins of 0.01, shown in figure 6.3. For example, a muon event with an Nch value of 200 is a

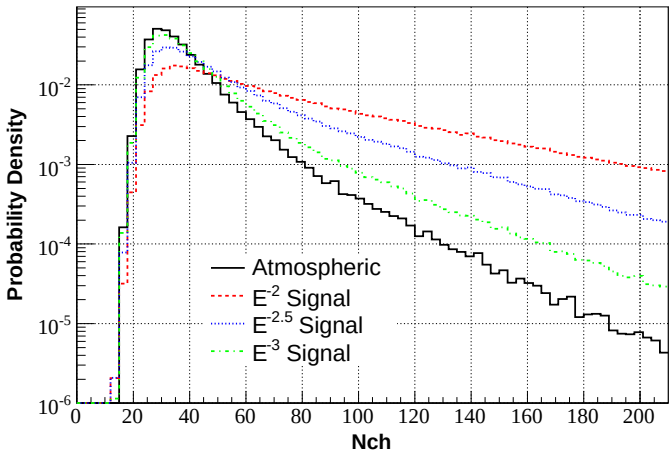

Figure 6.3: Simulated Nch distributions for atmospheric neutrinos [69] and E^{-2}, $E^{-2.5}$, and E^{-3} power law neutrino spectra.

factor of ∼100 more likely to be from an E^{-2} source than from the atmospheric background.

6.1.2.3 Signal and Background PDFs and the Test Statistic

The final signal PDF is the product of the spatial and energy PDFs,

$$\mathcal{S}_i(\Psi_i, \sigma_i, \mathrm{Nch}_i, \gamma) = \frac{1}{2\pi\sigma_i^2} e^{-\frac{\Psi_i^2}{2\sigma_i^2}} \times P(\mathrm{Nch}_i|\gamma). \tag{6.6}$$

The atmospheric neutrino background is uniform in right ascension and roughly uniform over a narrow declination band. Similar to the signal PDF, the normalized atmospheric neutrino background PDF is the product of the spatial and energy terms:

$$\mathcal{B}_i(\mathrm{Nch}_i) = \frac{1}{\Omega_{\mathrm{band}}} \times P(\mathrm{Nch}_i|Atm_\nu). \tag{6.7}$$

We only consider events within a declination band of ±8° of the search position $\vec{x}_s$, much larger than the declination-dependent AMANDA resolution of 1.5° - 2.5°. The normalization constant Ω_{band} is the solid angle of this band. If enough events are recorded, the probability $P(\mathrm{Nch}_i|Atm_\nu)$ can determined from an Nch histogram directly obtained from off-source data. This is preferable, especially in the case the data contains misreconstructed downgoing muons, which tend to have higher Nch values than atmospheric neutrinos; however, our sample of 6595 events is not sufficient at large Nch values, and we use probabilities tabulated from simulation.

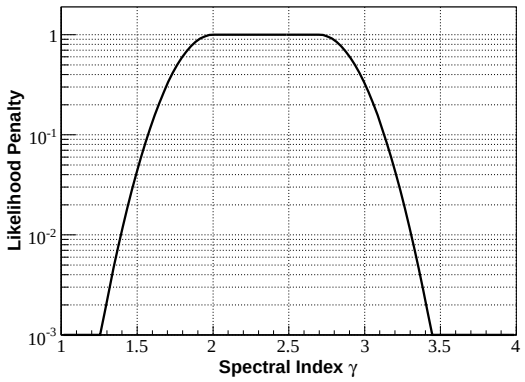

Figure 6.4: Likelihood penalty limiting γ to the range $2.0 < \gamma < 2.7$.

We model the data as a two-component mixture of signal and background events, i.e. the data is a combination of $\mathcal{S}_i$ and $\mathcal{B}_i$. The full-data likelihood is the product of this mixture likelihood over N total events in the declination band:

$$\mathcal{L}(\vec{x}_s, n_s, \gamma) = \prod_{i=1}^{N} \left(\frac{n_s}{N} \mathcal{S}_i + (1 - \frac{n_s}{N}) \mathcal{B}_i \right), \tag{6.8}$$

where $\frac{n_s}{N}$ is the unknown fraction of signal events. The likelihood is maximized with respect to n_s and γ, giving the best fit signal hypothesis and best estimates of the number of signal events $\hat{n}_s$ and spectral index $\hat{\gamma}$. We first perform a grid search in γ to determine a starting value, and then the maximization is done by numerically minimizing the quantity $-2 \log \mathcal{L}$ with the MIGRAD minimizer from the MINUIT library [116]. We limit γ to the approximate range $2.0 < \gamma < 2.7$ with a top-hat Gaussian likelihood penalty, shown in figure 6.4. The penalty improves discovery potential for the expected source spectra, shown in figure 6.6, by discriminating against the $\gamma \sim 3.7$ atmospheric neutrino background. Finally, a lower limit exists for the fraction of signal events $\frac{n_s}{N}$, below which $-2 \log \mathcal{L}$ becomes infinite, so we place an explicit bound on the minimization:

$$\frac{n_s}{N} > max\Big(\frac{\mathcal{B}_i}{\mathcal{B}_i - \mathcal{S}_i}\Big)_{\mathcal{S}_i > \mathcal{B}_i}. \tag{6.9}$$

If no events satisfy $\mathcal{S}_i > \mathcal{B}_i$, $-2 \log \mathcal{L}$ monotonically increases with $\frac{n_s}{N}$, and the minimization uses $\frac{n_s}{N} > -1$ as a lower bound. This pathological case occurs when no events are present within an angular distance comparable to the angular resolution and can effectively be ignored. Alternative likelihood

maximization techniques, including expectation-maximization (EM) [115], have been proposed and should yield equivalent results. The test statistic is the comparison of the background-only likelihood (i.e. $n_s = 0$) with the best fit signal likelihood, using $\hat{n}_s$, and $\hat{\gamma}$:

$$\lambda = -2 \cdot sign(\hat{n}_s) \cdot \log \left[\frac{\mathcal{L}(\vec{x}_s, 0)}{\mathcal{L}(\vec{x}_s, \hat{n}_s, \hat{\gamma})} \right]. \tag{6.10}$$

We include the factor $sign(\hat{n}_s)$ to differentiate negative and positive excesses.

Finally, it is preferable to include event energy information when the distribution of energies from signal events differs considerably from background. When the energies are comparable, e.g. in a search for neutrinos from WIMP annihilation (chapter 8), the inclusion of energy information provides no benefit. The signal and background PDFs without energy information are

$$\mathcal{S}_i(\Psi_i, \sigma_i) = \frac{1}{2\pi\sigma_i^2} e^{-\frac{\Psi_i^2}{2\sigma_i^2}} \tag{6.11}$$

$$\mathcal{B}_i = \frac{1}{\Omega_{band}}, \tag{6.12}$$

resulting in simpler expressions for $\mathcal{L}$.

6.2 Evaluating Significance and Discovery Potential

Given an observation of the test statistic λ, we compute significance by comparing the observed value with the distribution of test statistic values obtained from data randomized in right ascension, which is analogous to the background-only hypothesis. We obtain this distribution by performing $5{\times}10^6$ iterations of the likelihood search using randomized data, then recording the value of λ at an arbitrary point for each of 20 declination bands spanning -7.5° $< \delta <$ 87.5°. Larger values of λ are less compatible with the background hypothesis, so CL thresholds of λ are obtained by integrating the distribution backward. The 3σ threshold of λ is taken directly from the integral distribution, and because of statistical uncertainty, an exponential fit is done on the tail of the integral distribution to obtain the 5σ threshold, shown in figure 6.5. The integral distribution approximately follows a chi-square ($\sim \frac{1}{2}\chi_1^2$).

We then obtain distributions of the test statistic given a signal of known strength. For each declination band, we perform 50,000 iterations of the likelihood search for 80 values of signal strength from 1 to 80 added signal events. For each iteration, signal events are chosen by a weighted random

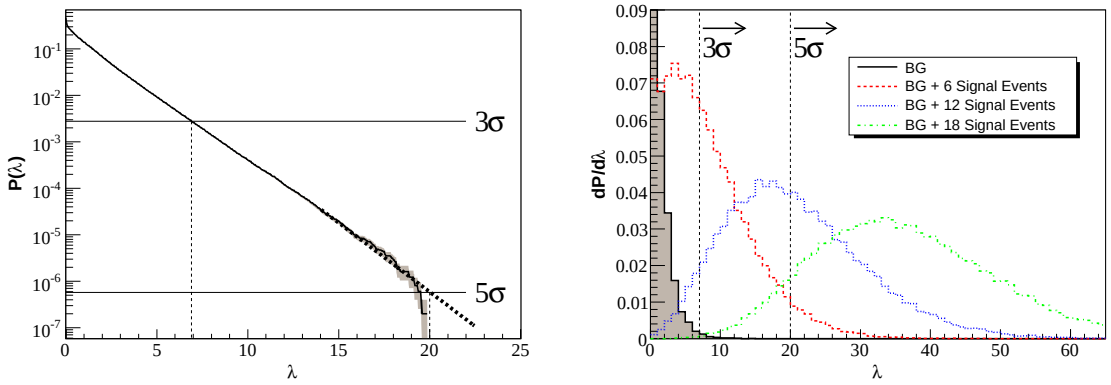

Figure 6.5: Integral distribution of the test statistic for background at δ=42.5° with 3σ and 5σ thresholds indicated and statistical uncertainty shaded in gray (left), and distribution of the test statistic for background and 6, 12, and 18 added signal events at δ=42.5° (right).

selection from neutrino simulation with a power-law energy spectrum, usually E^{-2}. For each value of signal strength, a fraction of trials F_i pass the 3σ or 5σ CL thresholds, shown in figure 6.5. From this, we compute the detection probability $\mathrm{F}(\mu)$, the fraction of trials passing 3σ or 5σ CL thresholds given a Poisson mean number of events μ:

$$\mathrm{F}(\mu) = \sum_{i=0}^{80} \Big(\mathrm{F}_i \times P(i|\mu) \Big), \tag{6.13}$$

where $P(i|\mu)$ is the Poisson probability of observing i events given mean μ. The mean number of events is directly proportional to the neutrino flux, and the fraction $\mathrm{F}(\mu)$ is the power at 3σ or 5σ CL thresholds. The power of this analysis is shown in figure 6.6, and 13 – 14 signal events are required to detect a neutrino point source at 5σ CL in 50% of trials. For E^{-2} spectra, the use of energy information in the likelihood reduces the mean number of events necessary to discover 50% of sources at 5σ CL by 35%, shown in figure 6.6. The improvement increases for harder spectra, and is close to zero for soft spectra $\sim\mathrm{E}^{-3}$ – $\mathrm{E}^{-3.5}$.

The proportionality factors between mean number of signal events and point source neutrino flux are determined by simulation. The model discovery potential (MDP) is the flux necessary to achieve a given CL and power, and is shown in figure 6.8 at 3σ and 5σ CL and 90% power as a

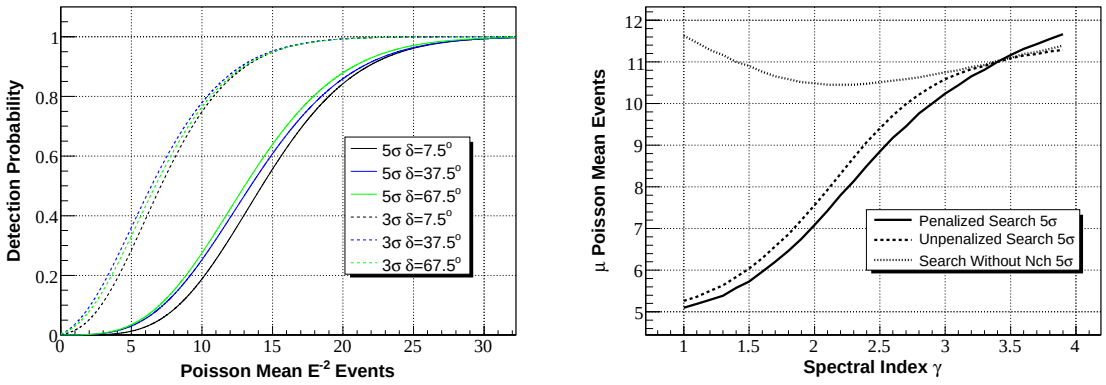

Figure 6.6: Power (detection probability) of the AMANDA 2000-2006 analysis at 3σ and 5σ CL as a function of mean signal strength (left), and comparison of 5σ CL, 50% power mean event thresholds for the analysis with spectral index constraint, without constraint, and not using Nch information as a function of spectral index for the AMANDA 2006 data (right).

function of declination.

6.3 Evaluating Flux Limits

Flux limits are evaluated using the frequentist Feldman-Cousins [117] technique. The observable for this analysis is the test statistic, which is continuous, rather than an integer number of events. We therefore generate our own confidence bands rather than using the precomputed tables of Feldman and Cousins. Our confidence limits constrain the mean number of signal events and are converted to flux limits with proportionality constants determined from simulation. We use $\mathcal{D} = \text{sign}(\lambda)\cdot\sqrt{|\lambda|}$ as the observable rather than λ to condense the observable axis. We create a 2-dimensional histogram with 3000 bins on the observable axis from -10 to 40 in $\mathcal{D}$ and 5000 bins on the mean signal strength axis from 0 to 50 events. We then fill the histogram with distributions of $\mathcal{D}$ for each of the 5000 values of the mean signal strength μ. For a given mean signal strength μ, the probability of obtaining $\mathcal{D}$ is

$$P(\mathcal{D}|\mu) = \sum_{i=0}^{80} \Big(P(\mathcal{D}|i) \times P(i|\mu) \Big), \tag{6.14}$$

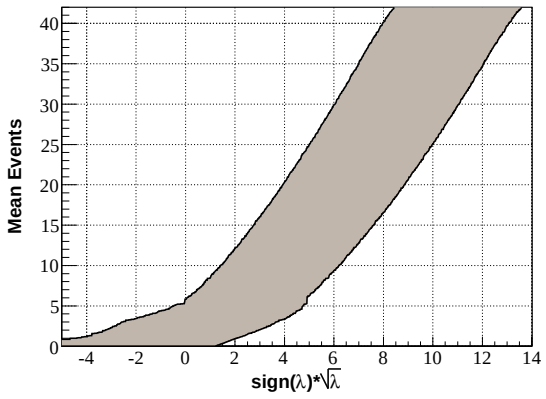

Figure 6.7: Feldman-Cousins 90% confidence level band for δ=42.5°.

where $P(\mathcal{D}|i)$ is the probability of obtaining $\mathcal{D}$ given i signal events, and $P(i|\mu)$ is the Poisson probability obtaining i signal events given μ. For each observable bin, the maximum value of $P(\mathcal{D}|\mu) = P(\mathcal{D}|\mu_{best})$ is recorded. Acceptance intervals are constructed for each value of μ by ranking each observable bin by the ratio

$$\mathcal{L} = P(\mathcal{D}|\mu)/P(\mathcal{D}|\mu_{best}). \tag{6.15}$$

The bin with the maximum value of $\mathcal{L}$ is included in the acceptance interval, and then the interval is expanded on either side by choosing the bin with the largest $\mathcal{L}$. The expansion continues until the integrated probability in the acceptance interval reaches 90% CL. The band coverage is then increased until all values of $\mathcal{D}$ intersect the band exactly twice, i.e. the band is monotonic. Figure 6.7 shows an example of the final confidence band created. Upper and lower limits in signal strength given an observation of $\mathcal{D}$ are the upper and lower intersection, respectively of the vertical line containing $\mathcal{D}$ and the band. Sensitivity is the average upper limit obtained from the $\mathcal{D}$ distribution given background alone (i.e. $P(\mathcal{D}|0)$). This procedure is repeated for each of the 20 declination bands and is shown in figure 6.8. The declination average sensitivity to muon neutrino fluxes following an E^{-2} energy spectrum is 2.5×10^{-11} TeV cm^{-2} s^{-1}.

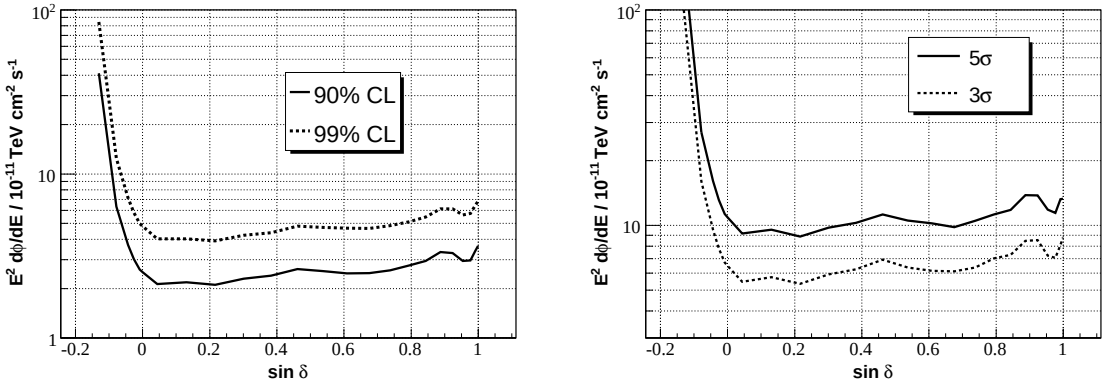

Figure 6.8: Sensitivity (left) and MDP at 90% power (right) for fluxes from point sources of muon neutrinos following E^{-2} energy spectra as a function of declination.

6.4 Estimating Spectral Index

Since source spectral index is a free parameter and fitted to the most likely value, the method provides an estimate of the spectral index of any discovered sources. The estimation becomes more accurate as the number of signal events increases, with 1σ uncertainty in spectral index improving from $\sim$0.3 for 15 signal events to $\sim$0.15 for 50 signal events, as shown in figure 6.9 for simulated E^{-2} and $E^{-2.5}$ source spectra. Source strength and spectral index can be constrained simultaneously from the likelihood function. Likelihood ratio contours enclosing the best fit minimum ($\hat{n}_s$ and $\hat{\gamma}$) are approximately chi-square distributed, with $-2 \cdot \log\left(\frac{\mathcal{L}(n_s,\gamma)}{\mathcal{L}(\hat{n}_s,\hat{\gamma})}\right) \sim \chi^2_2$. Figure 6.9 shows 1σ CL contours for 10 simulated experiments with 50 added signal events each, with E^{-2} energy spectra. 70% of the circles contain the true point, consistent with the chosen CL.

Finally, a small offset exists between the mean of $\hat{\gamma}$ returned from the likelihood minimization and the true value, as can be seen in figure 6.9. The offset is declination dependent and results from small differences in the Nch distribution with declination; it can be measured and calibrated away.

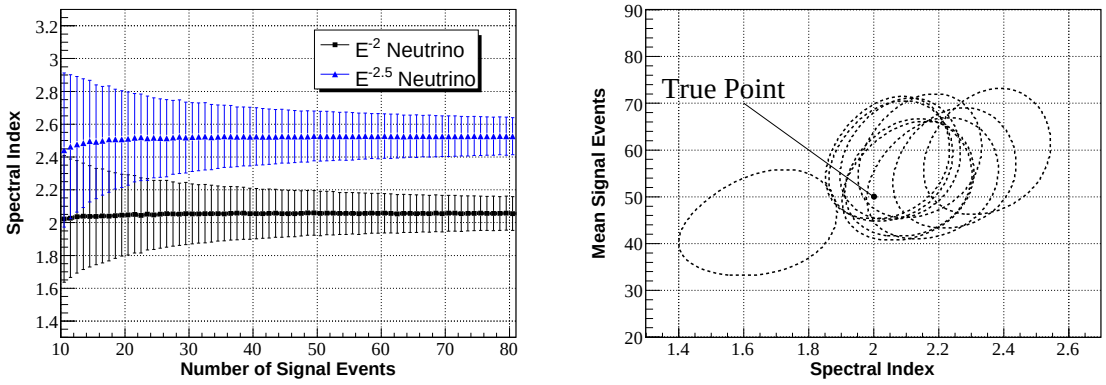

Figure 6.9: Spectral index estimation for simulated experiments with 10 to 80 added E^{-2} or $E^{-2.5}$ simulated signal events at $\delta = 22.5°$ (left). Error bars indicate the 1σ uncertainty in spectral index. Confidence contours for 10 simulated experiments at $\delta = 22.5°$ (right). The dashed circles represent the 1σ confidence level simultaneous estimation of signal strength and spectral index for each trial.

Chapter 7

Search for Neutrino Point Sources

We apply the method described in the previous chapter to three separate searches for ∼TeV neutrino point sources in the Northern Sky, including an unbiased search, a search based on a list of interesting astronomical objects, and a search for a cumulative signal from six Milagro hotspots. Finally, we perform a search for event correlations at small angular scales. We calculate significances and neutrino flux limits, taking into account the systematic uncertainties in our simulation.

7.1 Systematic Uncertainties

Systematic uncertainties affecting our event expectations from E^{-2} fluxes are itemized in table 7.1. Most of these uncertainties originate in our detector simulation and can be constrained by comparing simulated atmospheric neutrinos and downgoing muons with data. Especially, downgoing muons provide high statistics, and comparison with CORSIKA simulation allows an accurate estimate of these uncertainties.

7.1.1 Optical Module Sensitivity

The sensitivity of optical modules is not absolutely known and is one of the largest systematic uncertainties, directly affecting the trigger rate for near-threshold events. Simulations show this trigger rate effect is zenith dependent, and thus any global change in optical module sensitivity alters the zenith distribution of downgoing muons [118]. The optical module sensitivity in downgoing muon simulations is shifted until the simulated zenith distribution matches data, giving a best fit global optical module sensitivity offset of $^{+3}_{-10}$% and impacting the event expectation from E^{-2} neutrino

Source	Magnitude
Optical module sensitivity	$^{+2}_{-9}$ %
Photon propagation	± 5 %
Event selection bias	$^{+0}_{-7}$ %
Event reconstruction	$^{+0}_{-7}$ %
Rock density and neutrino cross section	± 8 %
Other known sources	< 4 %
Total	$\mathbf{^{+10}_{-17}}$ **%**

Table 7.1: Systematic uncertainties in event rate expectations for point sources with E^{-2} energy spectra.

fluxes by $^{+2}_{-9}$%.

7.1.2 Photon Propagation

The depth dependence in scattering and absorption coefficients of South Pole ice [87] are ignored in our simulation. A more recent photon propagation code [101] which includes this depth dependence is now available. A comparison of these simulations yields an event rate uncertainty of $\pm 5\%$ when applied to E^{-2} neutrino fluxes [118]. The uncertainties in optical module sensitivity and photon propagation are not fully independent and can alternatively be constrained simultaneously. This is done in [119] and chapter 8, and yields similar results.

7.1.3 Event Selection and Reconstruction

Simulated distributions of event selection parameters show small offsets relative to distributions obtained from data. Particularly, distributions of smoothness and angular uncertainty (σ_i) are shifted by ∼5-10% for simulated downgoing muons, and by ∼7-10% for atmospheric neutrinos in the final sample [118]. In both cases, the shifts show fewer data events are selected than suggested by simulation, and thus the event selection efficiency is overestimated. Scaling the simulation by these factors reduces event expectations from E^{-2} neutrino fluxes by 7% [118], so we assume an uncertainty of $^{+0}_{-7}$%. The bias in reconstruction uncertainty also suggests our reconstruction of simulated events is overly accurate and the point spread of E^{-2} neutrino point sources is underestimated. Increasing our simulated point spread by 8% results in E^{-2} neutrino flux limits 7% higher, so we assign an

uncertainty of $^{+0}_{-7}$%. The absolute pointing accuracy of AMANDA has been confirmed by observing downgoing muon events coincident with well-reconstructed air showers recorded by SPASE [93] and events coincident with IceCube.

7.1.4 Rock Density, Neutrino Cross Section, and Other Sources of Uncertainty

The rate of neutrino induced muons passing through the detector depends on the composition of the surrounding medium and the neutrino-nucleon charged current cross section. The density of underlying bedrock at the South Pole is known to 10% uncertainty [118]. Adjusting the bedrock density in simulations by 10% affects the E^{-2} neutrino event expectation by at most 7% [118] for near vertical events, which pass through the most bedrock. The neutrino-nucleon charged current cross section uncertainty is estimated by error analysis of CTEQ6 parton density functions [120], and the resulting uncertainty on E^{-2} event rates is less than 3% [118] at TeV – PeV energies. Other known sources of systematic uncertainty, including uncertainties in optical module timing resolution and uncertainties associated with the search method, total less than 4%. The total systematic uncertainty of $^{+10}_{-17}$% is incorporated into our Feldman-Cousins [117] limit calculations using the method of Conrad *et al.* [121] as modified by Hill [122].

7.2 Search for Point Sources

7.2.1 Search Based on a List of Candidate Sources

We first apply the search to a predefined list of 26 interesting coordinates (table 7.2), including locations of AGN, supernova remnants, microquasars, and other energetic phenomena. For each source location, we compute the value of the unbinned search test statistic λ and compare to data randomized in right ascension to compute significance. Limits on $\nu_\mu + \nu_\tau$ fluxes at 90% confidence level and chance probabilities (p) are shown in table 7.2. Limits on ν_μ fluxes alone correspond to half these values. The highest significance is found for Geminga with $p = 0.0086$. The probability of obtaining $p \leq 0.0086$ by chance for at least one of 26 sources is 20% and is therefore not significant.

7.2.2 Search of the Northern Sky

We then apply the search to declinations $-5^\circ < \delta < 83^\circ$ on a $0.25^\circ \times 0.25^\circ$ grid. The region above declination 83° is left to a dedicated search for WIMP annihilation at the center of the Earth [123]. For each grid point, we similarly compute a flux limit and significance (figure 7.1). We find a maximum pre-trial significance of $p = 7.4 \times 10^{-4}$ at $\delta = 54^\circ$, $\alpha = 11.4$h. We account for the trial factor associated with the all sky search by comparing the maximum pre-trial significance to the distribution of maximum pre-trial significances obtained from sky maps randomized in right ascension. We find 95% of sky maps randomized in right ascension have a maximum significance of at least $p = 7.4 \times 10^{-4}$ (figure 7.1). Sensitivity and flux limits are summarized in figure 7.3.

7.2.3 The Cygnus Region

The region near Cygnus deserves special attention, as several TeV gamma ray sources exist in this area. Most interesting are the galactic sources discovered by Milagro [18], including MGRO J2019+37 and MGRO J2031+41, which are detected at 10.4 σ and 6.6 σ pre-trial significance respectively. Subsequent observation of these sources by VERITAS [125] and MAGIC [83] suggest they have hard energy spectra with $\gamma \sim$-2. Further observation by Milagro has revealed diffuse emission from the Cygnus region [126]. Such observations suggest these TeV sources may be galactic cosmic ray accelerators and should be accompanied by neutrino emission. Several predictions of neutrino fluxes have been made for these sources [51, 127], which are generally about an order of magnitude weaker than the sensitivity of this analysis. Pre-trial significances from our analysis of this region are shown in figure 7.4 along with the significance map from Milagro [81]. The maximum pre-trial significance observed by AMANDA is $\sim$2.2 σ, which is not significant considering trial factors over the entire Northern Sky. A 1.5 σ excess of events is observed from the general Cygnus region ($72^\circ < l < 83^\circ, -3^\circ < b < 4^\circ$). If these small excesses are due to sources, they will be discovered by IceCube within the next few years.

7.2.4 Milagro Source Stacking

Since the galactic TeV gamma ray sources observed by Milagro are promising TeV neutrino candidates, we improve our ability to detect a weak signal from these objects by combining obser-

Candidate	$\delta(^\circ)$	$\alpha(h)$	Φ_{90}	p	$\Psi(^\circ)$	N
3C 273	2.05	12.49	8.71	0.086	2.1	3
SS 433	4.98	19.19	3.21	0.64	2.2	1
GRS 1915+105	10.95	19.25	7.76	0.11	2.3	8
M87	12.39	12.51	4.49	0.43	2.3	3
PKS 0528+134	13.53	5.52	3.26	0.64	2.3	0
3C 454.3	16.15	22.90	2.58	0.73	2.3	5
Geminga	17.77	6.57	12.77	0.0086	2.3	2
Crab Nebula	22.01	5.58	9.27	0.10	2.3	7
GRO J0422+32	32.91	4.36	2.75	0.76	2.2	3
Cyg X-1	35.20	19.97	4.00	0.57	2.1	3
MGRO J2019+37	36.83	20.32	9.67	0.077	2.1	7
4C 38.41	38.14	16.59	2.20	0.85	2.1	4
Mrk 421	38.21	11.07	2.54	0.82	2.1	3
Mrk 501	39.76	16.90	7.28	0.22	2.0	6
Cyg A	40.73	19.99	9.24	0.095	2.0	3
Cyg X-3	40.96	20.54	6.59	0.29	2.0	8
Cyg OB2	41.32	20.55	6.39	0.30	2.0	8
NGC 1275	41.51	3.33	4.50	0.47	2.0	4
BL Lac	42.28	22.05	5.13	0.38	2.0	2
H 1426+428	42.68	14.48	5.68	0.36	2.0	3
3C66A	43.04	2.38	8.06	0.18	2.0	6
XTE J1118+480	48.04	11.30	5.17	0.50	1.8	3
1ES 2344+514	51.71	23.78	5.74	0.44	1.7	2
Cas A	58.82	23.39	3.83	0.67	1.6	2
LS I +61 303	61.23	2.68	14.74	0.034	1.5	5
1ES 1959+650	65.15	20.00	6.76	0.44	1.5	5

Table 7.2: Flux upper limits for 26 neutrino source candidates: Source declination, right ascension, 90% confidence level upper limits for $\nu_\mu + \nu_\tau$ fluxes with E^{-2} spectra ($E^2\Phi_{\nu_\mu+\nu_\tau} \leq \Phi_{90} \times 10^{-11}\,\mathrm{TeV\,cm^{-2}\,s^{-1}}$) over the energy range 1.9 TeV to 2.5 PeV, pre-trial significance, median angular resolution of primary neutrino, and number of events inside a cone centered on the source location with radius equal to the median point spread. Since event energy is an important factor in the analysis, the number of nearby events does not directly correlate with pre-trial significance.

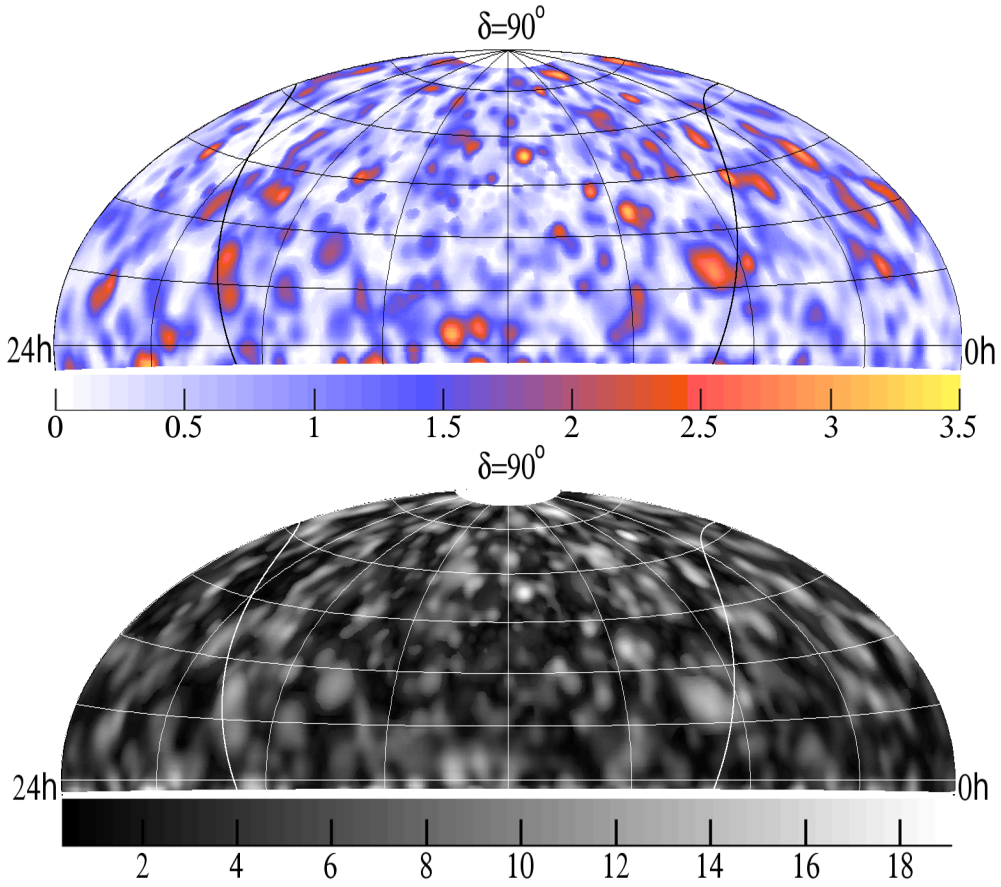

Figure 7.1: Sky map of significances (σ) obtained in the full-sky search excluding trial factors (top), and sky map of $\nu_\mu + \nu_\tau$ flux upper limits for an E^{-2} energy spectrum (10^{-11} TeV cm^{-2} s^{-1}) over the energy range 1.9 TeV to 2.5 PeV (bottom).

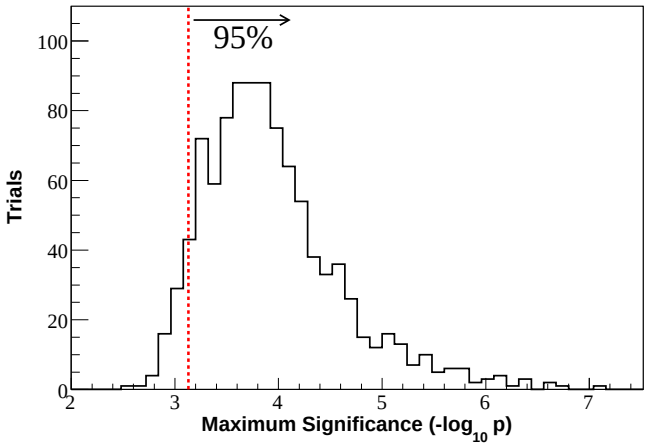

Figure 7.2: The distribution of maximum significances obtained from 1000 randomized sky maps, with the obtained significance $p = 7.4 \cdot 10^{-4}$ dotted.

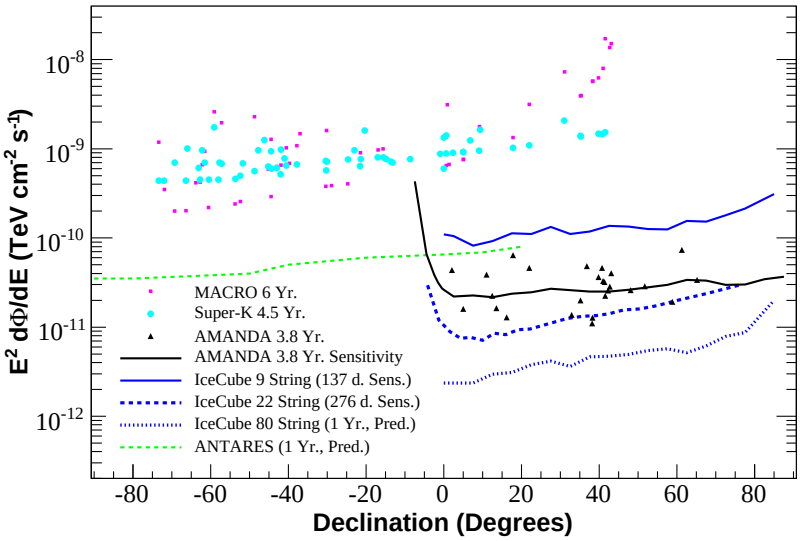

Figure 7.3: E^{-2} ν_μ flux limits for this work, MACRO [28], and Super-K [29], E^{-2} ν_μ sensitivity for this work and the IceCube 9-string analysis [92], and predicted sensitivity for ANTARES [124] and IceCube. Our $\nu_\mu + \nu_\tau$ limits are divided by 2 for comparison with limits on only ν_μ.

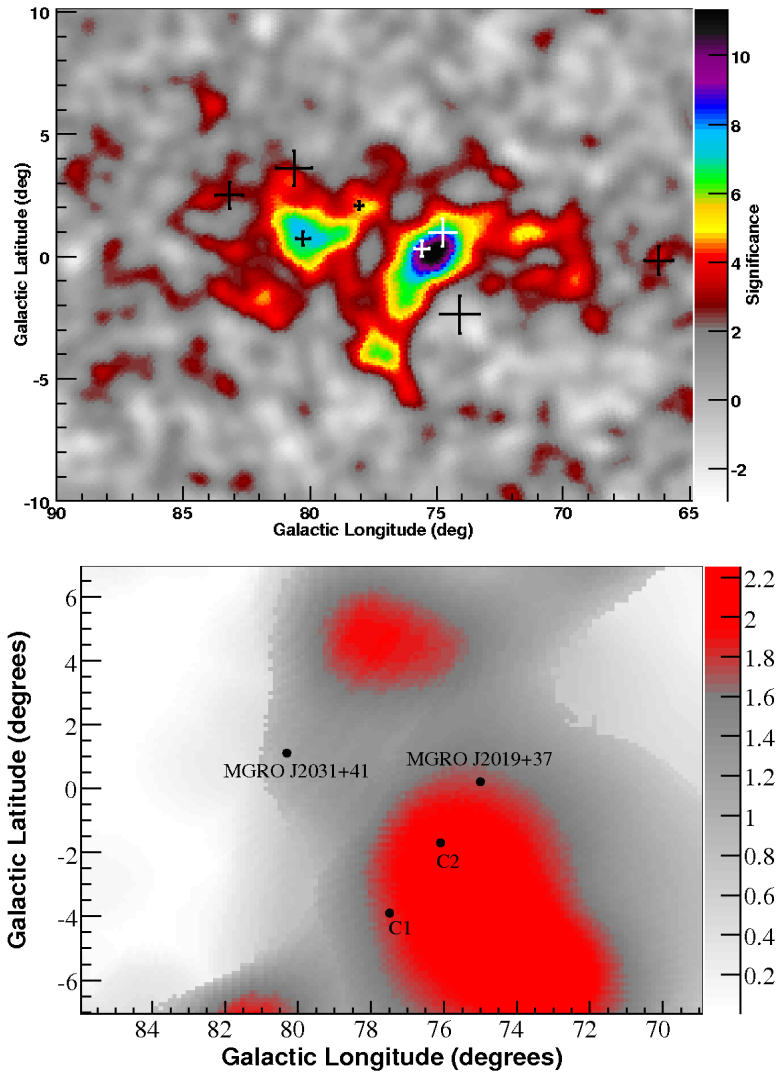

Figure 7.4: Pre-trial significance map of the Cygnus region in TeV gamma rays by Milagro (from [81], top), and significance map of the same region from AMANDA (bottom).

vations for several potential sources in a so-called stacking analysis. The improvement is $\sim \sqrt{N}$ for combining N sources of similar strength, with less improvement if one source is much stronger than average. We include five of eight sources and source candidates observed by Milagro with significance above 5σ before considering trial factors, including MGRO J2019+37 and MGRO J2031+41, two areas of lesser significance near Cygnus, and the source MGRO J1908+06. Observations by HESS [82] indicate MGRO J1908+06 has a hard energy spectrum with $\gamma \sim$-2, similar to the sources near Cygnus. We add a hot spot near $\delta = 1°$, $\alpha = 19$h [81], which may be associated with a large neutrino flux if confirmed as a source [51]. We exclude the three regions with pulsar-wind nebula counterparts, C3, C4, and the Crab Nebula, which are considered weaker candidates for significant hadron acceleration [51]. We adapt a method developed by HiRes [128] to perform our maximum likelihood search simultaneously for all six source locations, resulting in the slightly modified likelihood function

$$\mathcal{L} = \prod_{i=1}^{N} \left(\frac{1}{6} \cdot \frac{n_s}{N} \sum_{j=1}^{6} \mathcal{S}_i^j + (1 - \frac{n_s}{N}) \mathcal{B}_i \right), \tag{7.1}$$

where $\mathcal{S}_i^j$ is the signal probability density of the i^{th} event evaluated for the j^{th} source. Significance is again computed by comparing the obtained test statistic value to the distribution obtained from data randomized in right ascension. We observe a small excess with a chance probability of 20%. The 90% confidence level upper limit obtained on the mean ν_μ flux per source is 9.7×10^{-12} TeV cm^{-2} s^{-1}, considerably more stringent than the non-stacking limits for these sources.

7.2.5 Search for Event Correlations at Small Angular Scales

One additional signal scenario may be several sources producing only a few events each in AMANDA, too few to be considered significant individually in an all-sky analysis. However, the cumulative event clustering at small angular scales from all sources may yield an observable signal. We search for such a signal by counting the number of event pairs in the data given angular and energy constraints. We consider correlations of events at all angular distances up to 8° and over a range of energy thresholds, using the number of modules hit as an energy parameter. For each threshold in angular distance and number of modules hit, we count the number of event pairs in the data and compare with the distribution of pairs from data randomized in right ascension to compute significance. The highest obtained significance is $p = 0.1$ with a threshold of 146 modules hit and 2.8°

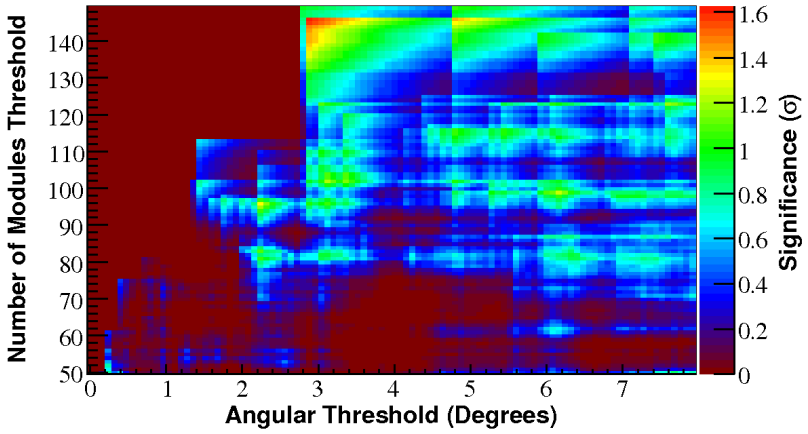

Figure 7.5: Significance (σ) of the observed number of event pairs with respect to thresholds on angular separation and number of modules hit.

angular separation, where we observe two event pairs. The probability of observing this maximum significance by chance, including trial factors from the sliding angular and energy thresholds, is 99% and is not significant. This hypothesis can additionally be tested by decomposing the data into spherical harmonics and searching for excesses at large l, indicating structure at small angular scales. A search using this technique [129] has revealed no excess.

Chapter 8

Search for WIMP Dark Matter from the Sun

An additional unknown component of the universe is the missing, non-luminous mass suggested by a wide variety of astronomical observations. The most recent measurements from WMAP [130] and SDSS [131] indicate this dark matter is cold, i.e. non-relativistic, and has a density $\Omega_c \sim 0.2$ ($\Omega_c h^2 = 0.1050 \pm 0.004$), significantly larger than that of baryonic matter $\Omega_b \sim 0.04$ (figure 8.1). Since the universe is very nearly flat ($\Omega_{tot} \sim 1$), the vast majority of the universe is dark energy, with $\Omega_\Lambda \sim 0.76$.

Weakly interacting massive particles (WIMPs) with electroweak scale masses are currently a favored explanation of cold dark matter. Such particles must be stable or have a lifetime comparable to the age of the universe, and would interact with luminous matter gravitationally and through weak interactions. The minimal supersymmetric standard model (MSSM) provides a natural candidate, the lightest neutralino [132]. An additional candidate is the lightest Kaluza-Klein particle (LKP), predicted by models of universal extra dimensions [133]. A large range of potential WIMP masses exists, with lower bounds of 47 GeV [2] and 300 GeV [134] on the lightest neutralino and LKP, respectively, imposed by accelerator-based analyses. The upper limit of WIMP masses is several TeV, as higher masses overpredict the observed dark matter density [135].

8.1 Detection of WIMP Dark Matter

If WIMPs comprise dark matter, they are present in our galaxy, orbiting the galactic center with mean velocity $\sim$270 km s^{-1} and density $\sim$0.3 GeV cm^{-3} [136]. Searches for these WIMPs generally follow two philosophies. First, WIMP-nucleon elastic scattering events may be directly

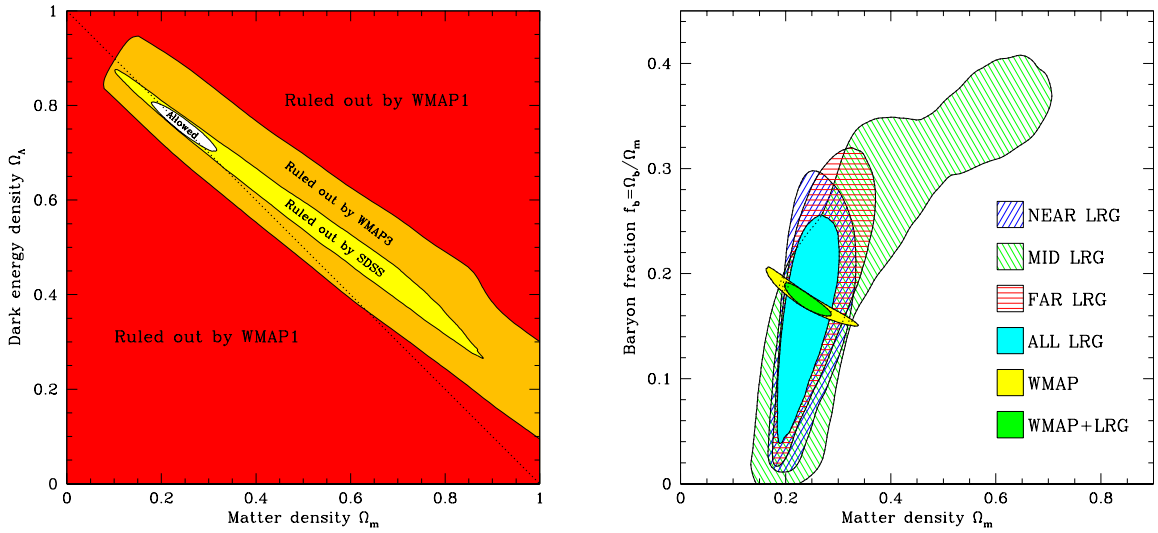

Figure 8.1: Combined measurements from WMAP and the SDSS luminous red galaxy (LRG) survey, showing energy vs. matter density (left), and baryon vs. total matter density (right), from [131].

observable in Earth-based detectors. Such *direct* detection experiments observe the recoil of target nuclei through ionization, scintillation, and phonons. The WIMP-nucleus cross section contains spin-independent (SI) and spin-dependent (SD) components, and it is not known which component is dominant. The most sensitive direct detection experiments [137, 138] use germanium and xenon nuclei, respectively, as targets. The SI cross section scales $\sigma_{SI} \sim A^2$, while the SD cross section does not scale as such with A; thus, direct detection experiments using targets with large A, including germanium and xenon, are much more sensitive to SI couplings. Results from direct detection experiments are summarized in figure 8.2. Multi-ton liquid xenon or liquid argon detectors (e.g. [139]) should improve current direct detection limits by a factor of 1000 in the next 10 – 15 years.

Alternatively, WIMP annihilation or decay may produce a flux of standard model particles observable at Earth. WIMP annihilation should produce W^+W^-, ZZ, quark, and heavy lepton pairs. Decay of these particles ultimately produces photons, neutrinos, and electrons and positrons; thus a WIMP signal would appear as an electron and positron cosmic ray excess or a flux of photons or neutrinos. Such an excess of cosmic ray electrons and positrons from ∼100 GeV – 1 TeV has

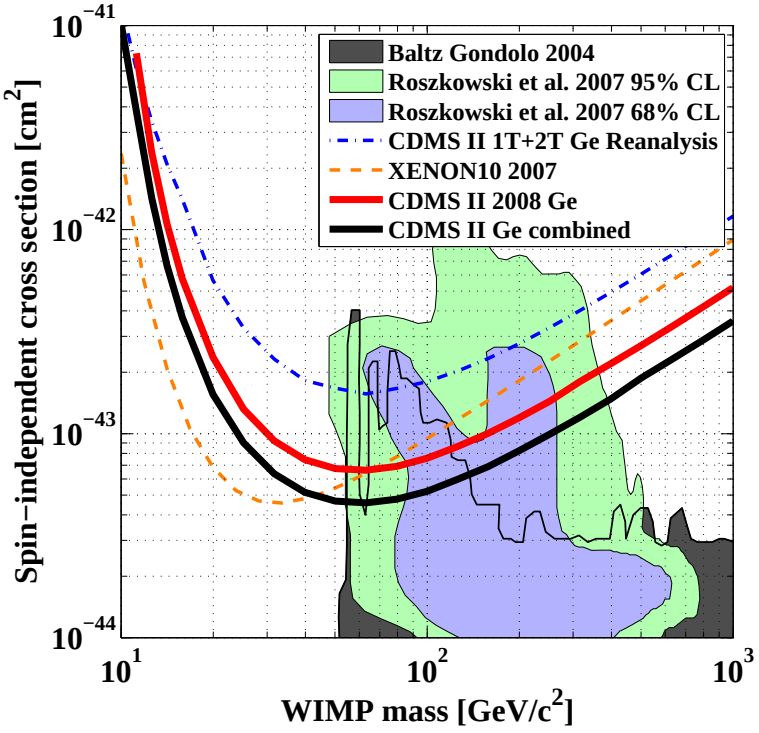

Figure 8.2: Spin-Independent WIMP cross section limits from CDMS [140] and XENON [141] as a function of WIMP mass, along with expected ranges from MSSM predictions, from [140].

recently been observed [21, 22, 23, 24] (figure 8.3), along with an excess of the cosmic ray positron fraction [25]. These excesses are consistent with a dark matter signal (e.g. [143]), but may have an alternative explanation (e.g. a local pulsar [144]). Additionally, a fraction of WIMPs should interact with massive objects and become gravitationally bound. The WIMPs would eventually accumulate and annihilate near the center, producing a neutrino flux. Natural objects for this type of search include the Sun, the Earth, and the galactic center. No emission of GeV – TeV neutrinos from the Sun or the center of the Earth have thus far been observed [145, 146, 147, 148, 149, 150].

8.2 Solar WIMP Search with AMANDA

The AMANDA point source data sample provides an opportunity to probe for GeV – TeV neutrino emission from the Sun. Because of cosmic ray muon background and event selection efficiency

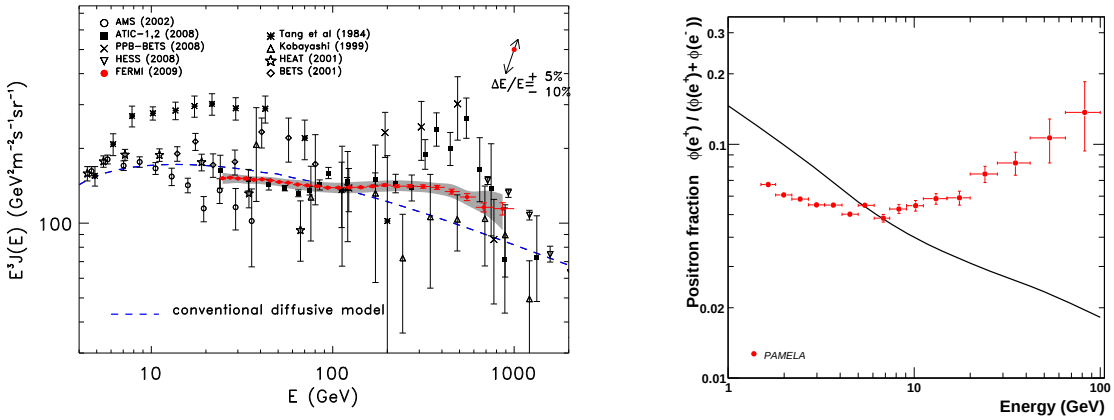

Figure 8.3: Measurements of cosmic ray electrons (left) showing an excess at a few hundred GeV, from [23], and PAMELA measurements of the positron fraction (right), from [25], showing an excess compared to the expected flux from cosmic ray positron production alone [142].

considerations, the search is limited to days when the Sun is below the horizon, reducing the data to 953 days livetime and 4665 total events.

8.2.1 Solar WIMP Signal Simulation

Neutralino annihilations are simulated for masses from 100 GeV to 5 TeV. The neutralino annihilation branching fractions are not known, so we consider the most optimistic case for detection (100% W^+W^-), and the most pessimistic case (100% $b\bar{b}$). For LKP annihilation, we use the branching fractions of [151], with the most significant contribution from $\tau\bar{\tau}$. Neutrino energy distributions at Earth from WIMP annihilation in the Sun (figure 8.4) are generated by DarkSUSY [152], and include absorption and oscillation effects from transit through the Sun to Earth. LKP annihilation spectra are generally similar to neutralino W^+W^- spectra. We simulate these neutrino spectra by reweighting a diffuse ANIS neutrino simulation, described in appendix A. Additionally, the simulation must be properly reweighted to the declination distribution of the Sun (figure 8.5) according to

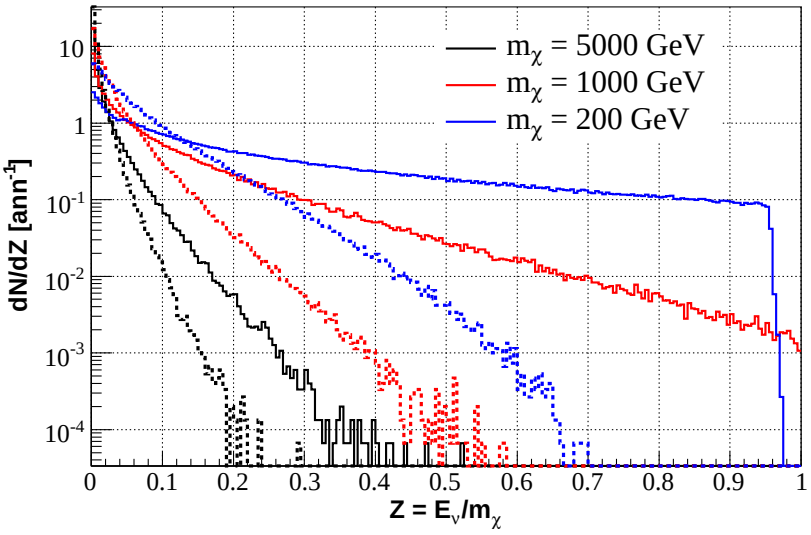

Figure 8.4: Neutrino energy spectra at Earth from neutralino annihilation into W^+W^- (solid) and $b\bar{b}$ (dashed), from DarkSUSY.

[153]:

$$w(\theta) = \frac{1}{\sqrt{1-\left(\frac{90-\theta}{\delta}\right)^2}} \frac{1}{sin\theta} \frac{\int_{80^\circ}^{180^\circ}\int_0^{2\pi} sin\theta d\phi d\theta}{\int_{90^\circ}^{90^\circ+\delta}\int_0^{2\pi} \frac{1}{\sqrt{1-\left(\frac{90-\theta}{\delta}\right)^2}} d\phi d\theta}. \tag{8.1}$$

Angular resolution worsens for soft spectra (figure 8.6) due mostly to the increasing angular mismatch between the muon and the primary neutrino. Additionally, AMANDA detection efficiency drops sharply for neutrino energies below ∼100 GeV. The neutrino effective area and effective volume, averaged over the neutrino energy spectra (appendix A), are shown in figure 8.7. AMANDA is therefore most sensitive to neutrino fluxes produced by annihilation of high mass WIMPs favoring hard (i.e. W^+W^- or $\tau\bar{\tau}$) annihilation channels.

8.2.2 Search Results

We use the unbinned search method, described in chapter 6, without the energy dependent term, since the expected neutrino energy spectra from WIMP annihilation are not significantly different from atmospheric neutrinos. Application of the search in Sun-centered coordinates yields a 0.8σ event deficit from the direction of the Sun, shown in figure 8.8.

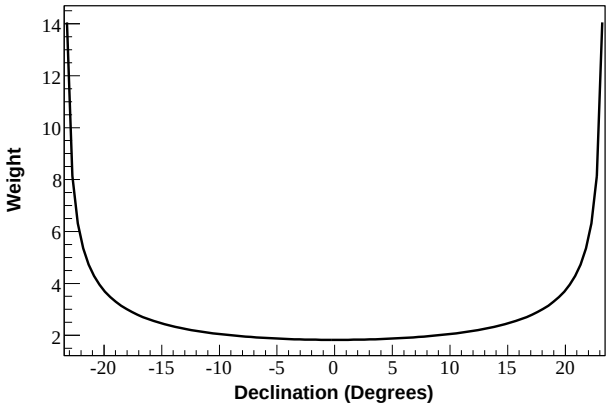

Figure 8.5: Declination distribution of the Sun.

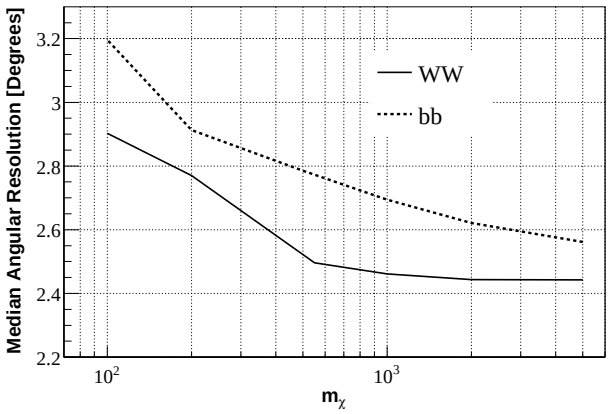

Figure 8.6: Angular resolution for neutralino annihilation spectra with neutralino masses 100 GeV – 5 TeV.

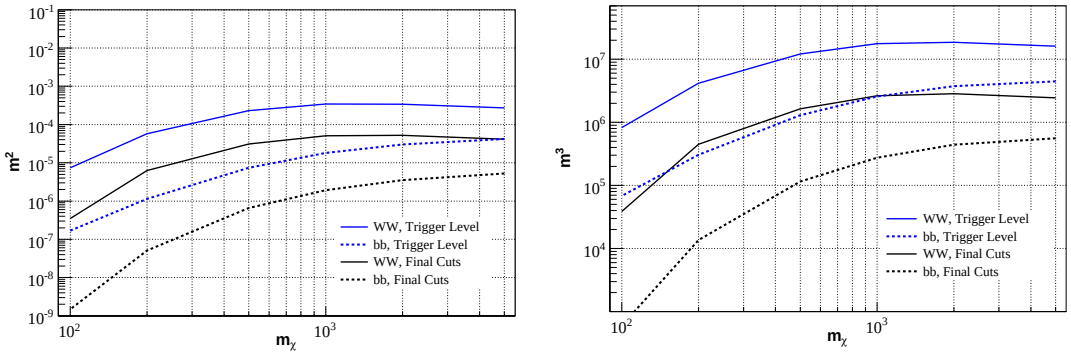

Figure 8.7: Spectrally averaged AMANDA effective area (left) and effective volume (right) for neutralino annihilation spectra with neutralino masses 100 GeV – 5 TeV, without including systematic uncertainties.

8.2.3 Limits on Neutrino-Induced Muon Fluxes and WIMP-Nucleon Cross Sections

The systematic uncertainties affecting upper limits are similar to those affecting the high energy point source analysis, described in section 7.1. An additional uncertainty arises from the uncertainty in neutrino oscillation parameters and affects the muon neutrino spectra observed at Earth. The uncertainties become significantly larger at low energies and affect the WIMP analysis particularly for low WIMP masses, shown in table 8.1 for the case of neutralino WIMPs. Uncertainties in limits for LKP WIMPs are similar to those from neutralino W^+W^- annihilation. The uncertainties due to event selection, event reconstruction, ice, and OM sensitivity are asymmetric and rectangular. We use the following procedure to incorporate these uncertainties into the limits:

- Center the rectangular uncertainty interval and shift effective volume accordingly.
- Transform the rectangular uncertainties into Gaussian uncertainties with the same RMS.
- Add the uncertainties in quadrature to get a final, total uncertainty.

The final Gaussian uncertainties and offsets are shown in table 8.2. The uncertainties, totaling 13%–24%, are incorporated into the Feldman-Cousins event upper limit calculation using method of Conrad *et al.* [121] as modified by Hill [122].

Uncertainty	Source	5000h	2000h	1000h	500h	200h	100h
Ice + OM Sensitivity	MC Study	$^{+7}_{-28}$%	$^{+7}_{-28}$%	$^{+7}_{-28}$%	$^{+9}_{-32}$%	$^{+9}_{-40}$%	$^{+14}_{-47}$%
Event Selection Bias	MC Study	$^{+0}_{-15}$%	$^{+0}_{-15}$%	$^{+0}_{-15}$%	$^{+0}_{-16}$%	$^{+0}_{-16}$%	$^{+0}_{-18}$%
Neutrino Oscillations	MC Study	±5%	±5%	±5%	±5%	±5%	±5%
Neutrino Cross Section	[114]	±3%	±3%	±3%	±3%	±3%	±3%
Reconstruction Bias	MC Study	$^{+0}_{-7}$%	$^{+0}_{-7}$%	$^{+0}_{-7}$%	$^{+0}_{-7}$%	$^{+0}_{-7}$%	$^{+0}_{-7}$%
ν_τ Contribution	[154]	+5%	+4%	+3%	+2%	+2%	+2%
Uncertainty	Source	5000s	2000s	1000s	500s	200s	100s
Ice + OM Sensitivity	MC Study	$^{+9}_{-32}$%	$^{+9}_{-34}$%	$^{+10}_{-37}$%	$^{+11}_{-40}$%	$^{+12}_{-48}$%	$^{+12}_{-62}$%
Event Selection Bias	MC Study	$^{+0}_{-16}$%	$^{+0}_{-16}$%	$^{+0}_{-16}$%	$^{+0}_{-17}$%	$^{+0}_{-19}$%	$^{+0}_{-27}$%
Neutrino Oscillations	MC Study	±5%	±5%	±5%	±5%	±5%	±5%
Neutrino Cross Section	[114]	±3%	±3%	±3%	±3%	±3%	±3%
Reconstruction Bias	MC Study	$^{+0}_{-7}$%	$^{+0}_{-7}$%	$^{+0}_{-7}$%	$^{+0}_{-7}$%	$^{+0}_{-7}$%	$^{+0}_{-7}$%
ν_τ Contribution	[154]	+4%	+3%	+2%	+2%	+2%	+2%

Table 8.1: Systematic uncertainties affecting upper limits on neutrino-induced muon fluxes and neutralino-nucleon cross sections for W^+W^- (h) and $b\bar{b}$ (s) neutralino annihilations.

	5000h	2000h	1000h	500h	200h	100h
Total Offset	−15%	−16%	−17%	−20%	−24%	−26%
Total Uncertainty	±13%	±13%	±13%	±15%	±17%	±19%
	5000s	2000s	1000s	500s	200s	100s
Total Offset	−18%	−20%	−22%	−23%	−28%	−39%
Total Uncertainty	±15%	±15%	±16%	±17%	±19%	±24%

Table 8.2: Final offsets and uncertainties for limits on W^+W^- (h) and $b\bar{b}$ (s) neutralino annihilations.

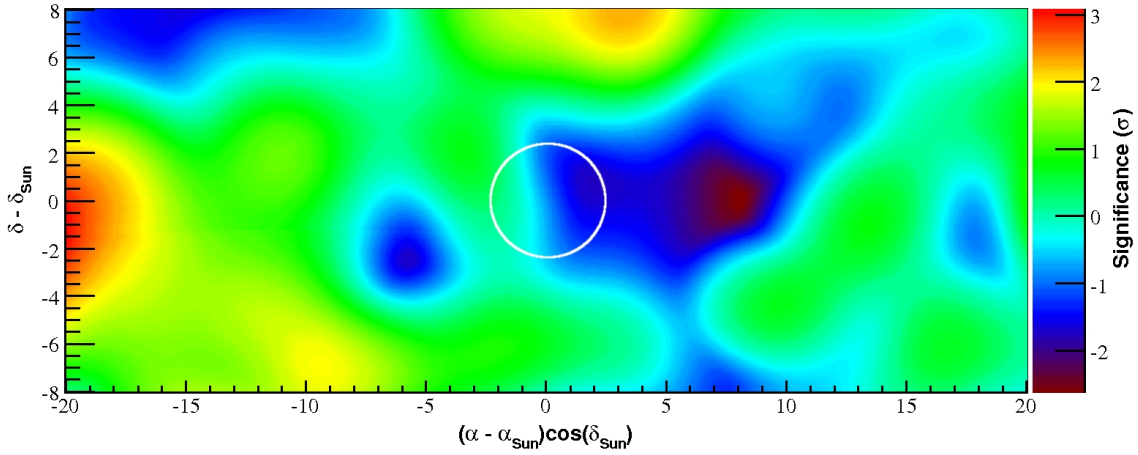

Figure 8.8: Sun-centered skymap of event excesses. The white circle is representative of the AMANDA median angular resolution for the highest energy spectra (i.e. $m_\chi = 5000$ GeV, W^+W^- annihilation channel).

Four meaningful upper limits are calculated from the muon event upper limits:

1. Limits on the WIMP annihilation rate in the Sun.
2. Limits on the neutrino-induced muon flux due to WIMP annihilation in the Sun.
3. Limits on the WIMP-nucleon SI cross section.
4. Limits on the WIMP-nucleon SD cross section.

The upper limits are strongly dependent on the neutrino spectra and therefore dependent on WIMP mass. Upper limits on the neutralino annihilation rate in the Sun are calculated from the event upper limit μ_{90} by

$$\Gamma_A = \frac{4\pi R^2 \mu_{90}}{N_A \rho T_L V_{eff}} \Big[\int_0^{m_\chi} \sigma_{\nu N} \frac{dN_\nu}{dE} dE \Big]^{-1}, \tag{8.2}$$

where R is the Earth-Sun radius, N_A is the Avogadro constant, ρ is the density of the detector medium, T_L is the livetime, $\sigma_{\nu N}$ is the neutrino-nucleon cross section, and $\frac{dN_\nu}{dE}$ is the neutrino energy spectrum. Limits on muon flux are given by

$$\Phi_\mu = \frac{\Gamma_A}{4\pi R^2} \int_{1\ GeV}^{m_\chi} \frac{dN_\mu}{dE} dE, \tag{8.3}$$

m_χ (GeV)	Channel	V_{eff} (m^3)	μ_{90}	Γ_A (s^{-1})	Φ_μ $(km^{-2}y^{-1})$	σ^{SI} (cm^2)	σ^{SD} (cm^2)
100	W^+W^-	2.87×10^4	4.5	1.88×10^{23}	6.75×10^3	3.40×10^{-42}	1.52×10^{-39}
	$b\bar{b}$	3.65×10^2	5.2	6.01×10^{25}	1.95×10^5	1.09×10^{-39}	4.85×10^{-37}
200	W^+W^-	3.42×10^5	4.0	9.81×10^{21}	1.09×10^3	4.23×10^{-43}	2.98×10^{-40}
	$b\bar{b}$	9.80×10^3	4.5	1.29×10^{24}	1.13×10^4	5.56×10^{-41}	3.92×10^{-38}
500	W^+W^-	1.31×10^6	3.7	2.07×10^{21}	5.39×10^2	3.51×10^{-43}	3.81×10^{-40}
	$b\bar{b}$	8.87×10^4	4.0	8.52×10^{22}	2.12×10^3	1.45×10^{-41}	1.57×10^{-38}
1000	W^+W^-	2.18×10^6	3.6	1.39×10^{21}	4.18×10^2	7.82×10^{-43}	1.01×10^{-39}
	$b\bar{b}$	2.14×10^5	4.0	2.89×10^{22}	1.26×10^3	1.63×10^{-41}	2.10×10^{-38}
2000	W^+W^-	2.38×10^6	3.6	1.56×10^{21}	3.90×10^2	3.19×10^{-42}	4.52×10^{-39}
	$b\bar{b}$	3.53×10^5	3.9	1.46×10^{22}	9.10×10^2	2.98×10^{-41}	4.23×10^{-38}
5000	W^+W^-	2.07×10^6	3.6	2.20×10^{21}	3.94×10^2	2.66×10^{-41}	3.97×10^{-38}
	$b\bar{b}$	4.59×10^5	3.7	8.91×10^{21}	7.17×10^2	1.08×10^{-40}	1.61×10^{-37}

Table 8.3: Effective volume, upper limit on the number of muon events from neutralino annihilation in the Sun, and upper limits on neutralino annihilation rate in the Sun, neutrino-induced muon flux from the Sun, and spin-independent and spin-dependent neutralino-proton cross section for a range of neutralino masses, including systematics.

traditionally with a lower threshold of 1 GeV on the muon energy. Finally, WIMP annihilation rates in the Sun are expected to reach equilibrium with capture rates [155]. Since the capture rate is dependent on the WIMP-nucleon cross section, limits on SI and SD cross sections can be calculated from annihilation rate limits [155]. Especially, since the Sun is composed mostly of protons with A = 1, the ratio of SD/SI cross section limits is much better than in modern direct detection experiments. These quantities are tabulated in table 8.3 for neutralino WIMPs and table 8.4 for LKP WIMPs. Limits on neutrino-induced muon flux from neutralino annihilations in the Sun are shown in figure 8.9, and limits on SD cross section are shown in figure 8.10 for neutralino WIMPs and figure 8.11 for LKP WIMPs.

SI cross section limits are not as stringent as those from direct detection experiments; however, limits on SD cross section are significantly better. We scan the MSSM parameter space to determine allowed SD cross sections as a function of WIMP mass, given the SI constraints from direct detection experiments and dark matter density constraints from cosmology. The new AMANDA SD limits (figure 8.10) are now beginning to exclude this allowed MSSM parameter space. A 1000-fold

m_χ (GeV)	V_{eff} (m^3)	μ_{90}	Γ_A (s^{-1})	Φ_μ $(km^{-2}y^{-1})$	σ^{SI} (cm^2)	σ^{SD} (cm^2)
250	4.91×10^5	3.6	6.75×10^{21}	744	3.96×10^{-43}	3.17×10^{-40}
500	1.21×10^6	3.7	2.48×10^{21}	507	4.21×10^{-43}	4.56×10^{-40}
700	1.56×10^6	3.7	1.97×10^{21}	468	5.89×10^{-43}	7.06×10^{-40}
900	1.82×10^6	3.5	1.65×10^{21}	424	7.68×10^{-43}	9.74×10^{-40}
1100	2.01×10^6	3.4	1.50×10^{21}	396	1.00×10^{-42}	1.32×10^{-39}
1500	2.23×10^6	3.5	1.50×10^{21}	394	1.78×10^{-42}	2.45×10^{-39}
3000	2.25×10^6	3.5	1.72×10^{21}	374	7.66×10^{-42}	1.12×10^{-38}

Table 8.4: Effective volume, event upper limit, and upper limits on the LKP annihilation rate in the Sun, neutrino-induced muon flux from the Sun, and spin-independent and spin-dependent LKP-proton cross section for a range of neutralino masses, including systematics.

improvement over current direct-detection SI limits does not significantly constrain allowed SD cross sections; thus, SD cross section limits from IceCube with the DeepCore extension (chapter 9) will continue to constrain MSSM parameter space. SD cross section limits for LKP WIMPs significantly improve existing limits (figure 8.11), but do not yet constrain the parameter space favored by WMAP and SDSS measurements of dark matter density.

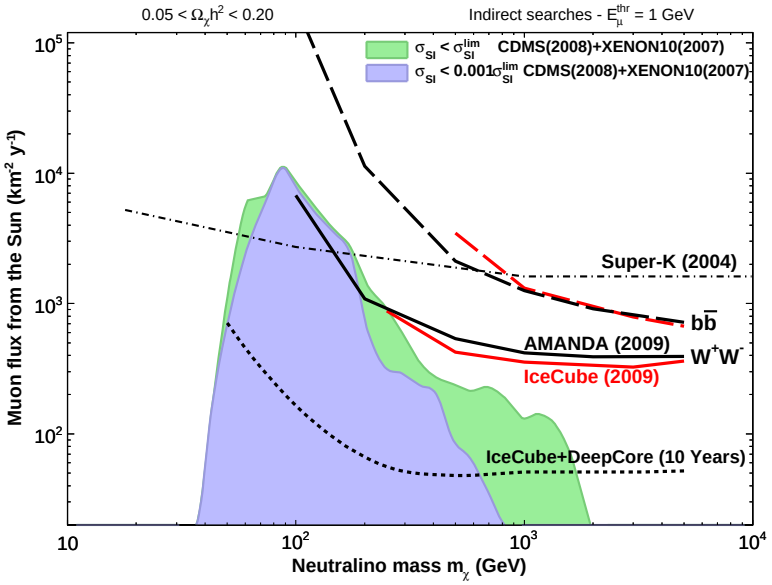

Figure 8.9: Limits on neutrino-induced muon flux from the Sun along with limits from IceCube [145], Super-K [148], and the projected sensitivity of 10 years operation of IceCube with DeepCore (section 9.1.2). The green shaded area represents models from a scan of MSSM parameter space not excluded by the spin-independent cross section limits of CDMS [140] and XENON [141], and the blue shaded area represents allowed models if spin-independent limits are tightened by a factor of 1000.

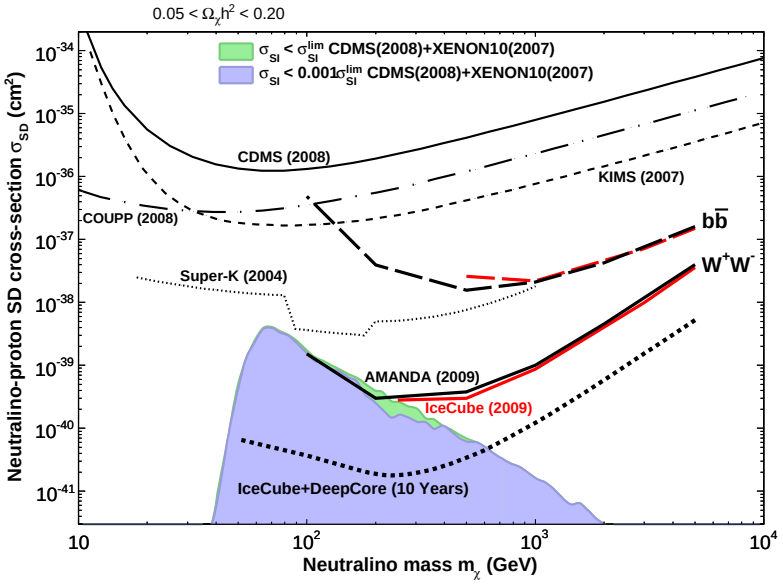

Figure 8.10: Limits on spin-dependent neutralino-proton cross section along with limits from CDMS [140], IceCube [145], Super-K [148], KIMS [156], COUPP [157], and the projected sensitivity of 10 years operation of IceCube with DeepCore (section 9.1.2). The green shaded area represents models from a scan of MSSM parameter space not excluded by the spin-independent cross section limits of CDMS [140] and XENON [141], and the blue shaded area represents allowed models if spin-independent limits are tightened by a factor of 1000.

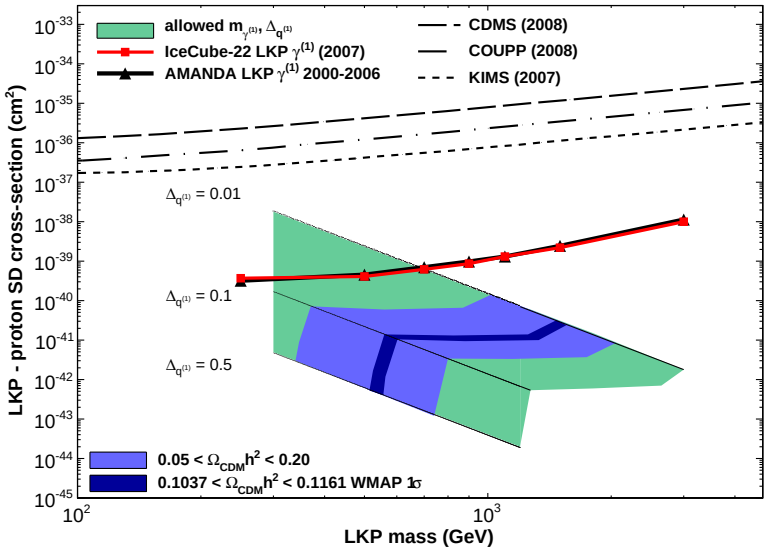

Figure 8.11: Limits on spin-dependent LKP-proton cross section along with limits from CDMS [140], IceCube, KIMS [156], and COUPP [157]. The green shaded area represents the allowed parameter space given a mass splitting $0.01 < \Delta_{q(1)} < 0.5$ between the LKP and lightest quark excitation. The light blue shaded area represents plausible models with dark matter density $0.05 < \Omega_{\rm CDM}h^2 < 0.2$, and the dark blue area represents the WMAP 1σ favored region.

Chapter 9

The Future

The non-detection of neutrino point sources by AMANDA indicates more sensitive detectors are necessary to detect astrophysical neutrino fluxes. In particular, volumes $\sim$km^3 are necessary for next-generation neutrino telescopes to probe predicted neutrino fluxes of 10^{-12} TeV cm^{-2} s^{-1}. The IceCube Neutrino Observatory [95] is currently under construction at the AMANDA South Pole site, and is scheduled for completion in 2011 with $\sim$1 km^3 instrumented volume. Additionally, efforts are underway to build a $\sim$km^3 neutrino telescope in the Mediterranean [158, 159], with the AMANDA-scale ANTARES [160] detector finished in 2008 and currently in operation.

9.1 IceCube

The IceCube array (figure 9.1) is currently under construction and will consist of 80 strings when complete in 2011, with each string containing 60 digital optical modules (DOMs). The strings are arranged hexagonally and instrument the region $\sim$1450-2450 m below the surface, for a total detector volume of $\sim$1 km^3. IceCube additionally contains a surface array, IceTop, consisting of 160 frozen water tanks, each with two DOMs, sensitive to the electromagnetic component of cosmic ray air showers. Finally, IceCube will contain the dense *DeepCore* subdetector, greatly enhancing sensitivity to low energy muons (section 9.1.2).

9.1.1 IceCube Digital Optical Modules

IceCube DOMs, illustrated in figure 9.2, are significantly more advanced compared to the optical modules of AMANDA. Each DOM contains several major components, including a 10 inch

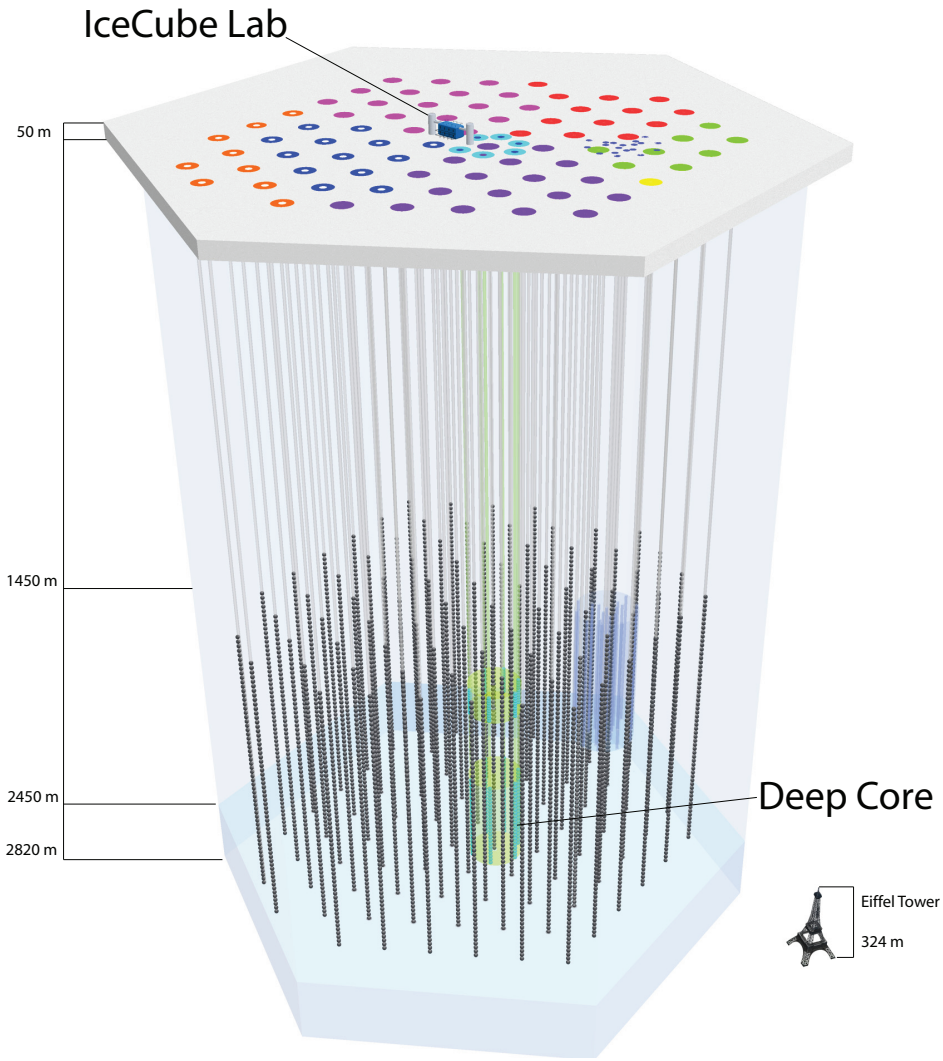

Figure 9.1: The IceCube Neutrino Observatory, to be completed at the South Pole in 2011.

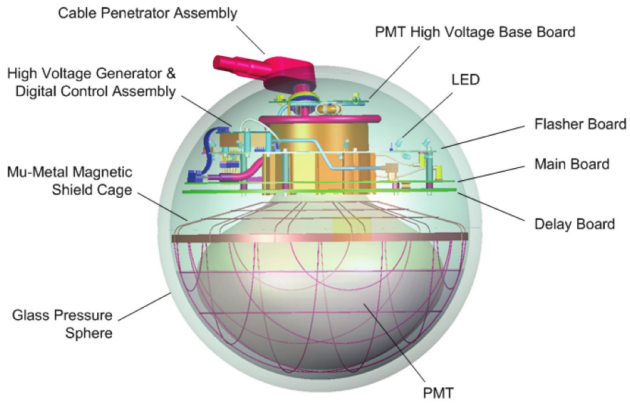

Figure 9.2: Diagram of the IceCube digital optical module (DOM).

Hamamatsu R7081-02 PMT, PMT base with an integrated high voltage generator, a LED flasher board for calibration, and a mainboard which contains the data acquisition [161] and control electronics. The mainboard is controlled by an Altera FPGA with an integrated ARM CPU, run underclocked at 40 MHz to conserve power. The majority of DAQ functions, including PMT voltage control and PMT signal acquisition, are ultimately controlled by software. PMT signals are split at the mainboard, with one signal routed through a 72 ns delay. The original signal is sent to a discriminator, and discriminator triggers are processed by the FPGA. The delayed signal is sent to two waveform capture ASICs: A 40 MHz fADC and one of two ATWDs, custom ASICs providing low-power, high-speed waveform capture. Digitized waveforms are then sent digitally to the surface, and DAQ software integrates waveforms from all DOMs in the array into events when the IceCube trigger conditions are satisfied. Each waveform includes a time stamp from the DOM mainboard local clock, which is synchronized to global GPS time using the RAPCal procedure [162], involving symmetric communication pulses. Each DOM dissipates ∼3 W total power, limited by the power availability at the South Pole.

IceCube DOMs eliminate many of the deficiencies observed with AMANDA modules and provide generally higher quality data. The major improvements are:

- Digitization of PMT waveforms at the source and digital communication eliminates the problems observed with transmission of analog signals to surface electronics. First, a PMT gain of

10^9 is required in AMANDA to overcome transmission losses, significantly reducing the PMT dynamic range, whereas IceCube DOM electronics are designed for 10^7 gain and provide a much better dynamic range of ∼200 photoelectrons per 15 ns. Additionally, the problems caused by crosstalk in AMANDA electrical channels are eliminated. Finally, IceCube PMT waveform information is not degraded during transit to the surface.

- RAPCal timing calibration in IceCube is accurate to ∼2-3 ns and automatic, whereas the AMANDA calibration must be performed after each change in surface electronics, generally after each austral summer polar season. The end-to-end IceCube timing resolution of 3-4 ns is much better than ∼ 15 ns in AMANDA.

- The 10 inch Hamamatsu R7081-02 PMT in IceCube DOMs provides ∼50% more photocathode surface area than the 8 inch AMANDA R5912-2 PMT.

9.1.2 IceCube DeepCore Extension

IceCube becomes relatively insensitive to muons at energies below ∼100 GeV due to the large string spacing of 125 m; however, a significant physics interest exists for neutrino-induced muons below ∼100 GeV. Such physics includes atmospheric neutrino oscillations and, especially, searches for annihilation of low mass WIMPs. IceCube sensitivity at low energies is enhanced by six additional high-density strings in the center of the detector. The additional strings, along with seven nearby standard strings, compose the thirteen string DeepCore subdetector [163] (figure 9.3). The additional strings reduce the DeepCore string spacing to 72 m. DOMs on these strings are spaced at 7 m and contain new PMTs recently developed by Hamamatsu, with high quantum efficiency (∼40%) super-bialkali photocathodes. Most importantly, the DOMs are located mostly in the clear ice at the bottom of the detector, maximizing the ability to record photon hits from low energy muons. One DeepCore string was installed in the 2008 – 2009 season, and the remaining five will be added by early 2010.

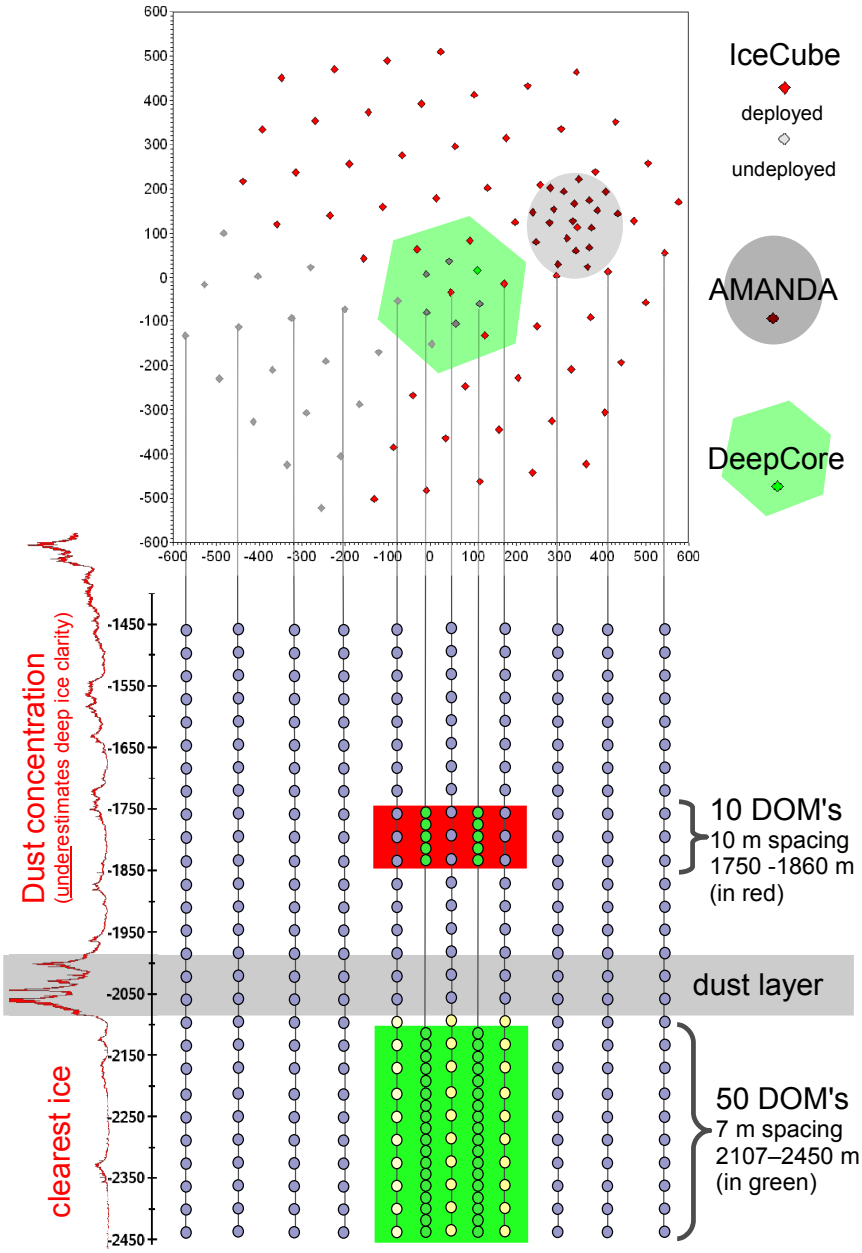

Figure 9.3: Diagram of the DeepCore extension to IceCube.

Bibliography

[1] V. F. Hess, Phys. Z. **13**, 1804 (1912).

[2] C. Amsler *et al.* [PDG], Physics Letters **B667**, 1 (2008).

[3] AMS http://ams.cern.ch/.

[4] PAMELA, http://pamela.roma2.infn.it/.

[5] JACEE, http://marge.phys.washington.edu/jacee/.

[6] CREAM, http://cosmicray.umd.edu/cream/.

[7] AGASA, http://www-akeno.icrr.u-tokyo.ac.jp/AGASA/.

[8] HiRes, http://www.cosmic-ray.org/.

[9] Pierre Auger Observatory, http://www.auger.org/.

[10] R. U. Abbasi *et al.* [HiRes], Phys. Rev. Lett. **100**, 101101 (2008).

[11] J. Abraham *et al.* [Auger], Phys. Rev. Lett. **101**, 061101 (2008).

[12] K. Greisen, Phys. Rev. Lett. **16**, 748 (1966); G. T. Zatsepin and V. A. Kuzmin, Sov. Phys. JETP Lett. **4**, 78 (1966).

[13] M. Unger,*et al.* [Auger], in *Proc. 30th ICRC*, Mérida, (2007), arXiv:0706.1495v1.

[14] J. Ahrens *et al.* [AMANDA], Astropart. Phys. **21**, 565 (2004).

[15] M. Amenomori *et al.* [Tibet], Science **314**, 439 (2006).

[16] A. A. Abdo *et al.* [MILAGRO], Phys. Rev. Lett. **101**, 221101 (2008).

[17] R. U. Abbasi, P. Desiati, and J. C. Velez, in *Proc. 31st ICRC*, Łódź, (2009).

[18] A. Abdo *et al.* [MILAGRO], Astrophys. J. Lett. **664**, L91 (2007).

[19] F. Aharonian *et al.* [HESS], Astrophys. J. **636**, 777 (2006).

[20] J. Albert *et al.* [MAGIC], Science **312**, 1771 (2006).

[21] J. Chang *et al.* [ATIC], Nature **456**, 362 (2008).

[22] S. Torii *et al.* [PPB-BETS], arXiv:0809.0760 (2008).

[23] A. A. Abdo *et al.* [Fermi], Phys. Rev. Lett. **102**, 181101 (2009).

[24] F. Aharonian *et al.* [HESS], arXiv:0905.0105 (2009).

[25] O. Adriani *et al.* [PAMELA], Nature **458**, 607 (2009).

[26] A. Achterberg *et al.* [IceCube], Phys. Rev. D **76**, 042008 (2007).

[27] R. Abbasi *et al.* [IceCube], Phys. Rev. D **79**, 062001 (2009).

[28] M. Ambrosio *et al.* [MACRO], Astrophys. J. **546**, 1038 (2001).

[29] S. Desai *et al.* [Super-Kamiokande], Astropart. Phys. **29**, 42 (2008).

[30] M. Ackermann *et al.* [IceCube], Astrophys. J. **675**, 1014 (2008).

[31] A. Achterberg *et al.* [IceCube], Astrophys. J. **674**, 357 (2008).

[32] J. Abraham *et al.* [Auger], Phys. Rev. Lett. **100**, 211101 (2008).

[33] I. Kravchenko *et al.* [RICE], Phys. Rev. D **73**, 082002 (2006).

[34] P. W. Gorham *et al.* [ANITA], J. Phys. Conf. Ser. **136**, 022052 (2008).

[35] N. G. Lehtinen *et al.* [FORTE], Phys. Rev. D **69**, 013008 (2004).

[36] V. Berezinsky, M. Kachelrie, and A. Vilenkin, Phys. Rev. Lett. **79**, 4302 (1997).

[37] D. J. H. Chung, E. W. Kolb, and A. Riotto, Phys. Rev. D **59**, 023501 (1998).

[38] P. Bhattacharjee, G. Sigl, Rhys. Rep. **327**, 109 (2000).

[39] J. Abraham *et al.* [Auger], Astropart. Phys. **29**, 243 (2008).

[40] J. Abraham *et al.* [Auger], arXiv:0903.1127 (2009).

[41] D. Semikoz and G. Sigl, JCAP **0404**, 003 (2004).

[42] E. Fermi, Phys. Rev. **75**, 1169 (1949).

[43] A. M. Hillas, Annu. Rev. Astron. Astrophys. **22**, 425 (1984).

[44] L. Anchordoqui, T. Paul, S. Reucroft and J. Swain, Int. J. Mod. Phys. A **18**, 2229 (2003).

[45] A. Achterberg *et al.*, Astropart. Physics **26**, 282 (2006).

[46] TeVCat, http://tevcat.uchicago.edu/.

[47] M. Blazejowski *et al.*, Astrophys. J. **630**, 130 (2005).

[48] C. Kouveliotou *et al.*, Astrophys. J. Lett. **413**, 101 (1993).

[49] P. Mézéros, Annu. Rev. Astron. Astrophys. **40**, 137 (2002).

[50] E. Woods and A. Loeb, Astrophys. J. Lett. **425**, 63 (1994).

[51] F. Halzen, A. Kappes, and A. OMurchadha, Phys. Rev. D **78**, 063004 (2008).

[52] F. Aharonian *et al.*, J. Phys. Conf. Ser. **39**, 408 (2006).

[53] D. Torres and F. Halzen, Astropart. Phys. **27**, 500 (2007).

[54] W. Bednarek *et al.*, New Astron. Rev. **49**, 1 (2005).

[55] E. Waxman and J. Bahcall, Phys. Rev. Lett. **78**, 2292 (1997).

[56] F. W. Stecker, Phys. Rev. D **72**, 107301 (2005).

[57] K. Mannheim, R. J. Protheroe, and J. P. Rachen, Phys. Rev. D **63**, 023003 (2000).

[58] A. Loeb and E. Waxman, J. Cosmol. Astropart. Phys. **05**, 003 (2006).

[59] S. Razzaque, P. Mészáros, E. Waxman, Phys. Rev. D **68**, 083001 (2003).

[60] F. Aharonian *et al.* [HESS], Astron. Astrophys. **449**, 223 (2006).

[61] M. Boettcher, A. Reimer, and A. P. Marscher, arXiv:0810.4864 (2008).

[62] T. Kobayashi *et al.*, Adv. Space Res. **27**, 653 (2001).

[63] S. Yoshida and M. Teshima, Prog. Theor. Phys. **89**, 833 (1993).

[64] R. Engel *et al.*, Phys. Rev. D **64**, 093010 (2001).

[65] P. Gorham, 1^{st} International Workshop on the Saltdome Shower Array (SalSA), SLAC, (2005).

[66] B. Louis *et al.*, Los Alamos Sci. **25**, 16 (1997).

[67] R. Abbasi *et al.* [IceCube], Phys. Rev. D **79**, 102005 (2009).

[68] M. C. González-García, M. Maltoni, and J. Rojo, JHEP **0610**, 075 (2006).

[69] G. Barr *et al.*, Phys. Rev. D **70**, 023006 (2004).

[70] M. Honda *et al.*, Phys. Rev. D **75**, 043006 (2007).

[71] E. Zas, F. Halzen, and R. A. Vázquez, Astropart. Phys. **1**, 297 (1993).

[72] R. U. Abbasi *et al.* [HiRes], Astrophys. J. **623**, 164 (2005).

[73] J. Abraham *et al.* [Auger], Science **318**, 938 (2007).

[74] R. Abbasi *et al.* [HiRes], Astropart. Phys. **30**, 175 (2008).

[75] [HESS], http://www.mpi-hd.mpg.de/hfm/HESS/.

[76] [MAGIC], http://wwwmagic.mppmu.mpg.de/.

[77] [VERITAS], http://veritas.sao.arizona.edu/.

[78] [Tibet], http://www.icrr.u-tokyo.ac.jp/em/.

[79] [Milagro], http://umdgrb.umd.edu/cosmic/milagro.html.

[80] [HAWC] http://hawc.umd.edu/.

[81] A. Abdo, Ph.D thesis, Michigan State University, (2007).

[82] A. Djannati-Atai *et al.* [HESS], in *Proc. 30th ICRC*, Mérida, (2007), arXiv:0710.2418.

[83] J. Albert *et al.* [MAGIC], Astrophys. J. Lett. **675**, L25 (2008).

[84] D. Chirkin and W. Rhode, arXiv:hep-ph/0407075 (2004).

[85] T. Weiler, Phys. Rev. Lett. **49**, 234 (1982).

[86] P. B. Price and K. Woschnagg, Astropart. Phys. **15**, 97 (2001).

[87] M. Ackermann *et al.* [AMANDA], J. Geophys. Res. **111**, D13203 (2006).

[88] E. Andres *et al.*, Astropart. Phys. **13**, 1 (2000).

[89] J. G. Learned and K. Mannheim, Annu. Rev. Nucl. Part. Sci. **50**, 679 (2000).

[90] A. M. Dziewonski, D. L. Anderson, Physics of the Earth and Planetary Interiors, **25**, 297 (1981).

[91] M. C. Gonzalez-Garcia *et al.*, Phys. Rev. Lett. **100**, 061802 (2008).

[92] The IceCube Collaboration, in *Proc. 30th ICRC*, Mérida, (2007), arXiv:0711.0353.

[93] J. Ahrens *et al.* [AMANDA], Nucl. Inst. Meth. A **524**, 169 (2004).

[94] A. Achterberg et al. [AMANDA], Nucl. Instrum. Meth. A **556**, 169 (2006).

[95] J. Ahrens *et al.* [IceCube], Astropart. Phys. **20**, 507 (2004); http://icecube.wisc.edu.

[96] W. Wagner *et al.*, in *Proc. 28th ICRC*, **2**, 1365 (2003).

[97] J. Lundberg, Ph.D Thesis, Uppsala Universitet (2008).

[98] N. E. Bramall *et al.*, Geophys. Res. Lett. **32**, L21815 (2005).

[99] A. Gazizov and M. Kowalski, Comput. Phys. Commun. **172**, 203 (2005).

[100] H. L. Lai *et al.*, Eur. Phys. J. **C12**, 375 (2000).

[101] J. Lundberg *et al.*, Nucl. Inst. Meth. A **581**, 619 (2007).

[102] S. Hundertmark, Ph.D Thesis, Humboldt-Universität zu Berlin, Germany (1999).

[103] D. Heck *et al.*, Forschungszentrum Karlsruhe, Tech. Rep. FZKA 6019 (1998).

[104] M. Ribordy, AMANDA internal report, http://icecube.berkeley.edu/amanda-private/reports/20020601-retrigg.pdf.

[105] D. Boersma *et al.*, http://internal.icecube.wisc.edu/amanda/software/sieglinde/.

[106] D. Pandel, Diploma thesis, Humboldt-Universität zu Berlin, Germany (1996).

[107] T. Neunhöffer, Astropart. Phys. **25**, 220 (2006).

[108] T. Burgess, Ph.D Thesis, Stockholm University (2008).

[109] G. C. Hill and K. Rawlins. Astropart. Phys. **19**, 393 (2003).

[110] T. Joachims, in *Advances in Kernel Methods - Support Vector Learning*, ed. B. Schölkopf, C. Burges, and A. Smola, MIT-Press, 169 (1999).

[111] A table of the AMANDA final event sample is available at http://www.icecube.wisc.edu/science/data.

[112] J. Braun *et al.*, Astropart. Phys. **29**, 299 (2008).

[113] T. Neunhöffer and L. Köpke, Nucl. Instr. Meth. A **558**, 561 (2006).

[114] A. Heijboer, PhD Thesis, University of Amsterdam (2004), available at http://antares.in2p3.fr/Publications/index.html#thesis.

[115] J. A. Aguilar and J. J. Hernández-Rey, Astropart. Phys. **29**, 117 (2008).

[116] F. James, http://wwwasdoc.web.cern.ch/wwwasdoc/minuit/.

[117] G.J. Feldman and R.D. Cousins, Phys. Rev. D **57**, 3873 (1998).

[118] A. Achterberg *et al.* [IceCube], Phys. Rev. D **75**, 102001 (2007).

[119] J. Kelley, Ph.D Thesis, University of Wisconsin (2008).

[120] J. Pumplin *et al.* [CTEQ], J. High Energy Phys. **17**, 012 (2002).

[121] J. Conrad *et al.*, Phys. Rev. D **67**, 012002 (2003).

[122] G.C. Hill, Phys. Rev. D **67**, 118101 (2003).

[123] A. Achterberg *et al.* [IceCube], Astropart. Phys. **26**, 129 (2006).

[124] J. Aguilar, in *Proc. 30^{th} ICRC*, Mérida, (2007), arXiv:0710.0252.

[125] D. Kieda *et al.*, in *Proc. 30^{th} ICRC*, Mérida, (2007).

[126] A. A. Abdo *et al.* [MILAGRO], Astrophys. J. **688**, 1078 (2008).

[127] J. F. Beacom and M. D. Kistler, Phys. Rev. D **75**, 083001 (2007).

[128] R. Abbasi *et al.* [HiRes], Astrophys. J. **636**, 680 (2006).

[129] A. Schukraft, J.–P. Huelss, in *Proc. 31^{st} ICRC*, Łódź, (2009).

[130] J. Dunkley *et al.* [WMAP], Astrophys. J. Suppl. **180**, 306 (2009).

[131] M. Tegmark *et al.* [SDSS], Phys. Rev. D **74**, 123507 (2006).

[132] M. Drees and M. M. Nojiri, Phys. Rev. D **47**, 376 (1993).

[133] D. Hooper and S. Profumo, Phys. Rep. **453**, 29 (2007).

[134] J. F. Oliver, J. Papavassiliou, and A. Santamaria, Phys. Rev. D **67**, 056002 (2003).

[135] R. C. Gilmore, Phys. Rev. D **76**, 043520 (2007).

[136] M. Kamionkowski and A. Kinkhabwala, Phys. Rev. D **57**, 3256 (1998).

[137] [CDMS], http://cdms.berkeley.edu/.

[138] [XENON], http://xenon.astro.columbia.edu/.

[139] [LANNDD], arXiv:astro-ph/0604548 (2006).

[140] Z. Ahmed *et al.* [CDMS], Phys. Rev. Lett. **102**, 011301 (2009).

[141] J. Angle *et al.* [XENON], Phys. Rev. Lett. **100**, 021303 (2008).

[142] I. V. Moskalenko and A. W. Strong, Astrophys. J. **493**, 694 (1998).

[143] L. Bergström, J. Edsjö, and G. Zaharijas, arXiv:0905.0333 (2009).

[144] H. Yuksel, M. D. Kistler, T. Stanev, arXiv:0810.2784 (2008).

[145] R. Abbasi *et al.* [IceCube], Phys. Rev. Lett. **102**, 201302 (2009).

[146] M. M. Boliev *et al.* [BAKSAN], Nucl. Phys. Proc. Suppl. **48**, 83 (1996).

[147] M. Ambrosio *et al.* [MACRO], Phys. Rev. D **60**, 082002 (1999).

[148] S. Desai *et al.* [Super-Kamiokande], Phys. Rev. D **70**, 083523 (2004).

[149] M. Ackermann *et al.* [AMANDA], Astropart. Phys. **26**, 155 (2006).

[150] D. Hubert, PhD Thesis, Vrije Universiteit Brussel (2009).

[151] D. Hooper and G. D. Kribs, Phys. Rev. D **67**, 055003 (2003).

[152] P. Gondolo *et al.*, JCAP **0407**, 008 (2004).

[153] D. Hubert, IceCube internal report.

[154] G. Wikstrom, http://www.physto.se/ wikstrom/icecube/ic22/taus.html.

[155] G. Wikström and J. Edsjö, JCAP **04**, 009 (2009).

[156] H. S. Lee *et al.*, Phys. Rev. Lett. **99**, 091301 (2007).

[157] E. Behnke *et al.*, Science **319**, 933 (2008).

[158] [KM3NeT], http://www.km3net.org/proposal/KM3NeT-FINAL-PROPOSAL-ShorterVersionForWebsite.pdf and http://km3net.org.

[159] [NEMO], http://nemo.lns.infn.it.

[160] The ANTARES Collaboration, astro-ph/9907432; http://antares.in2p3.fr.

[161] R. Abbasi *et al.* [IceCube], Nucl. Instrum. Meth. A **601**, 294 (2009).

[162] A. Achterberg *et al.* [IceCube], Astropart. Physics **26**, 155 (2006).

[163] D. Cowen *et al.* [IceCube], in *Proc. of NEUTEL09*, Venice, (2009).

[164] J. Albert *et al.* [MAGIC], Astrophys. J. **693**, 303 (2009).

[165] P. Gregory, Astrophys. J. **575**, 427 (2002).

[166] D. Leahy, A&A **380**, 516 (2001).

[167] A. A. Abdo *et al.* [Fermi], arXiv:0907.4307 (2009).

Appendix A

Weighting Simulated Events

A detector simulation is generally necessary to understand the response of particle detectors to classes of events not present or easily identifiable in the data. Since no high energy neutrino point sources have been identified, point source searches require simulation to asses angular pointing resolution, muon energy resolution, event quality parameters, and the response of the detector to very high energy events. Often when simulating these events, the unlikely events are the most interesting, and understanding the properties of these unlikely events is an essential aspect of the simulation. Finite CPU resources may make simulation of such rare events prohibitive at their natural rate. One solution is to increase the frequency of these events by some factor, and then *reweight* the events back to their original probability, thus reducing statistical uncertainty.

A.1 Weighting Neutrino Simulation

The efficiency of neutrino simulation is improved by weighting in two ways. First, simulated neutrino events that do not interact near the detector are useless since they would never be detected, and the probability of a neutrino interaction near the detector is generally very small, especially for neutrino energies below ∼PeV. Each neutrino is thus forced to interact near the detector. Additionally, the energy spectra of potential sources are not known, and these spectra are expected to vary considerably. The solution is to generate events with a flat spectrum, then reweight each event by the probability difference between this flat spectrum and the spectrum to be tested.

Each neutrino event is forced to interact within the simulation active volume V_i, generally defined by a generation area A_i normal to the track and length L_i along the track, enclosing the

detector. For efficiency and correctness, this active volume should be the smallest practical volume covering all the coordinates of interaction vertices which could possibly trigger the detector. For muon and tau neutrino simulations, it is therefore efficient to use a variable length L_i depending on the maximum lepton range, a function of neutrino energy. The probability of the simulated neutrino interacting within the length L_i is

$$P_{int,i} = 1 - \exp\big(-\sigma_i \rho N_A L_i\big) \simeq \sigma_i \rho N_A L_i; \quad (\mathrm{E}_\nu \lesssim 10 \text{ EeV}), \tag{A.1}$$

where σ_i is the neutrino cross section, ρ is the average density of the medium, and N_A is the Avogadro constant. Horizontal and upgoing neutrinos must pass through a portion of the Earth before reaching the active volume; therefore, the attenuation probability of absorbing the neutrino in transit through Earth must be included:

$$P_{abs,i} = 1 - \exp\big(-\sigma_i N_A X_i\big), \tag{A.2}$$

where X_i is the cumulative column density along the neutrino path. The event weight w_i is then

$$w_i = P_{int,i}\big(1 - P_{abs,i}\big) \frac{\frac{d^2\Phi_i}{dEd\Omega}}{\frac{d^2\Phi_{i,Sim}}{dEd\Omega}}, \tag{A.3}$$

where $\frac{d^2\Phi_{i,Sim}}{dEd\Omega}$ is the simulated event spectrum and $\frac{d^2\Phi_i}{dEd\Omega}$ is the desired spectrum. The simulated event spectrum is not an input and must be derived. The spectrum is a function of fundamental simulation parameters, including the number of simulated events (N_{sim}), the simulated livetime (τ), the simulated energy range, the generation area A_i, and the simulated solid angle (Ω), often a range of cos θ. No angular dependencies within this range of cos θ are generally introduced in the simulation; such dependencies are added through the reweighted spectrum. For convenience, the simulated energy dependence is typically a power law $\mathrm{E}^{-\gamma}$. First, expanding the simulated flux term,

$$\frac{d^2\Phi_{sim}}{dEd\Omega} = \frac{d^4N_{sim}}{dtdAdEd\Omega}. \tag{A.4}$$

The total number of simulated events is the integral of the simulated event spectrum:

$$N_{sim} = \int_\Omega \int_{E_{min}}^{E_{max}} \int_A \int_\tau \frac{d^4N_{sim}}{dtdAdEd\Omega} dtdAdEd\Omega. \tag{A.5}$$

The angle, time, and area dependencies of the simulated event spectrum are constants, and the energy dependence is a power law; thus the quantity

$$\frac{d^4N_{sim}}{dtdAdEd\Omega} E^\gamma \tag{A.6}$$

is a constant and can be factored from the integrand. Integrating the time, angle, and area dimensions gives:

$$N_{sim} = \tau A \Omega \frac{d^4 N_{sim}}{dt dA dE d\Omega} E^{\gamma} \int_{E_{min}}^{E_{max}} E^{-\gamma} dE. \tag{A.7}$$

Since the generation area and energy generally vary event-by-event, each event i is simulated with a particular flux:

$$\frac{d^2\Phi_{i,Sim}}{dE d\Omega} = \frac{d^4 N_{i,Sim}}{dt dA dE d\Omega} = \frac{N_{sim}}{\tau A_i \Omega E_i^{\gamma} \int_{E_{min}}^{E_{max}} E^{-\gamma} dE}, \tag{A.8}$$

where A_i is the event generation area and E_i is the event energy. The final event weight is found by substituting the simulated spectrum of equation A.8 into equation A.3:

$$w_i = w_{\circ,i} \times \frac{d^2\Phi_i}{dE d\Omega} \tag{A.9}$$

$$w_{\circ,i} = \frac{1}{N_{sim}} P_{int,i}\left(1 - P_{abs,i}\right) \tau A_i \Omega E_i^{\gamma} \int_{E_{min}}^{E_{max}} E^{-\gamma} dE, \tag{A.10}$$

where $w_{\circ,i}$ is the weight for a unit spectrum with no energy dependence (i.e. E^0). For ANIS neutrino simulation, this weight is

$$w_{\circ,i} = Si1 \times Flux \times \tau \times E_i^{\gamma} \times \frac{1}{N_{files}}, \tag{A.11}$$

where $Si1$ and $Flux$ are weights returned by ANIS, τ is the livetime in years, and $\frac{d^2\Phi_i}{dE d\Omega}$ is the desired neutrino spectrum; $\frac{d^2\Phi_i}{dE d\Omega}$ is the the sum of $(\nu + \bar{\nu})$ fluxes if generation of both neutrinos and antineutrinos is requested.

A.2 Neutrino Effective Area

The rate of observed neutrino events is directly proportional to an incident neutrino flux,

$$\frac{dN}{dt} = \Phi_{\nu} \times A_{eff}, \tag{A.12}$$

where the proportionality constant A_{eff} has dimensions of area. This constant is significantly smaller than the detector cross sectional area:

- Only a fraction of neutrinos interact near the detector.
- Only a fraction of neutrino interactions are observed by the detector and recorded as events.
- Of these events, many are eliminated by event quality selection.

The *effective* area A_{eff} combines these complicated effects into a single quantity and represents the cross sectional area of a perfectly efficient detector, i.e. detecting all neutrino events passing through the area and no events outside the area. The effective area is strongly dependent on neutrino energy and zenith angle; thus, the rate of neutrino events predicted by a neutrino spectrum $\frac{d^2\Phi}{dEd\Omega}$ is the convolution

$$\frac{dN}{dt} = \int_E \int_\Omega A_{eff}(E,\theta)\frac{d^2\Phi}{dEd\Omega}(E,\theta)d\Omega dE. \tag{A.13}$$

Using this the effective, others can calculate the number of events an arbitrary flux would produce in a given time and therefore determine whether such a flux would be observable. Additionally, effective areas are useful to compare detectors, and, when the effective area includes an event selection efficiency factor, can be used to compare the relative quality of an event selection to other analyses.

Generically, the effective area is the product of generation area and selection efficiency:

$$A_{eff} = \frac{N_{sel}}{N_{sim}}A_{gen} = \frac{\sum_{i=1}^{N_{sim}}\delta_i}{N_{sim}}A_{gen}; \qquad \delta_i = \begin{cases} 1 & \text{if event is selected} \\ 0 & \text{if event is not selected} \end{cases} \tag{A.14}$$

For weighted simulation, both the interaction probability and separate generation area of each event must be taken into account:

$$A_{eff} = \frac{\sum_{i=1}^{N_{sim}} P_{int,i}\big(1-P_{abs,i}\big)A_i\delta_i}{N_{sim}}. \tag{A.15}$$

Equation A.15 returns the average effective area for the entire simulated energy and zenith range according to the input spectrum $\mathrm{E}^{-\gamma}$. The effective area as a function of neutrino energy and zenith angle is generally more useful. This is calculated by dividing the simulation into energy and zenith bins and calculating effective area for each individual bin. Logarithmic energy binning is practical since neutrino detectors are sensitive over many orders of magnitude in neutrino energy. The effective area for a bin in log E and cos θ is calculated using the weights in equation A.10, weighting the simulation to an E^{-1} spectrum and giving equal weight in each bin in log E. The effective area for a bin with space angle Ω_{bin} and energy range $\mathrm{E}_{low} < \mathrm{E} < \mathrm{E}_{hi}$ is given by equation A.15 and equation A.10, reweighted to an E^{-1} spectrum:

$$A_{eff} = \frac{\sum_{i=1}^{N_{sim}}\frac{w_{o,i}}{E_i}\delta_i}{\tau\Omega\int_{E_{min}}^{E_{max}}E^{-1}dE} \times \Big[\frac{\Omega_{bin}}{\Omega}\Big]^{-1} \times \Big[\frac{\int_{E_{low}}^{E_{hi}}E^{-1}dE}{\int_{E_{min}}^{E_{max}}E^{-1}dE}\Big]^{-1} \tag{A.16}$$

$$= \frac{\sum_{i=1}^{N_{sim}}\frac{w_{o,i}}{E_i}\delta_i}{\tau\Omega_{bin}\ln(E_{hi}/E_{low})}, \tag{A.17}$$

where the second two terms in equation A.16 represent the angular and energy bin fractions, respectively. The formulation in equation A.17 is convenient since only the event weight w_i, event energy, and livetime are needed for the effective area calculation.

A.3 Effective Volume

Alternatively, detector response can be characterized by the rate neutrino interaction events are detected. For muon neutrino interactions,

$$\frac{dN}{dt} = \Gamma_{\nu\to\mu} \times V_{eff}, \tag{A.18}$$

where $\Gamma_{\nu\to\mu}$ is the neutrino to muon conversion rate per unit volume. The effective volume V_{eff} represents a perfectly efficient volume detector, detecting all neutrino interactions occurring inside. For large energies, the effective volume is much closer to the detector geometric volume than the effective area is to the detector cross sectional area, since V_{eff} does not depend on the neutrino cross section.

Similar to the effective area, the effective volume is the product of generation volume and selection efficiency:

$$V_{eff} = \frac{N_{sel}}{N_{sim}} V_{gen} = \frac{\sum_{i=1}^{N_{sim}} \delta_i}{N_{sim}} V_{gen}. \tag{A.19}$$

More intuitively, the effective volume is related to the effective area:

$$\Gamma_{\nu\to\mu} = \Phi_\nu \times \frac{dP_{\nu\to\mu}}{dZ}, \tag{A.20}$$

where $\frac{dP_{\nu\to\mu}}{dZ}$ is the interaction probability per unit length along the track,

$$\frac{dP_{\nu\to\mu}}{dZ} = \sigma_\nu \rho N_A, \tag{A.21}$$

from equation A.1. Thus,

$$V_{eff} = \frac{A_{eff}}{\sigma_\nu \rho N_A}. \tag{A.22}$$

This expression is often the most practical method to determine the effective volume, since many neutrino generators do not output either the active volume V_i or length L_i needed for the calculation. For a bin in log E and solid angle, the effective volume is found according to equation A.17 and A.22:

$$V_{eff} = \frac{\sum_{i=1}^{N_{sim}} \frac{w_{\circ,i}}{\sigma_i E_i} \delta_i}{\rho N_A \tau \Omega_{bin} \ln(E_{hi}/E_{low})} \tag{A.23}$$

A.4 Spectrally Averaged Effective Areas and Volumes

In many cases, it is desirable to average effective area or effective volume to a particular neutrino spectrum. Observed event rates are directly proportional to the averaged effective area or volume and the spectrum normalization, and are a practical way to compare sensitivity to the spectrum. The spectrally averaged effective area for a neutrino spectrum $\frac{d\Phi_\nu}{dE}$ is

$$\overline{A_{eff}} = \frac{\int_0^\infty A_{eff}(E)\frac{d\Phi_\nu}{dE}(E)dE}{\int_0^\infty \frac{d\Phi_\nu}{dE}(E)dE}, \tag{A.24}$$

assuming the energy range of the simulation $\mathrm{E}_{min} < \mathrm{E} < \mathrm{E}_{max}$ sufficiently covers the energy range of detectable events produced by the flux. The averaging is most easily done by reweighting the events to the desired spectrum and computing effective area in one bin over the entire simulated energy range:

$$\overline{A_{eff}} = \frac{\sum_{i=1}^{N_{sim}} w_{\circ,i}\frac{d\Phi_\nu}{dE}(E_i)\delta_i}{\tau\Omega\int_0^\infty \frac{d\Phi_\nu}{dE}(E)dE}. \tag{A.25}$$

The spectral averaging for effective volume is slightly different, since the energy distribution of observed events depends on both the neutrino cross section and energy spectrum; however, the effective volume does not include the neutrino cross section dependence. Thus, the cross section is averaged with the spectrum:

$$\overline{V_{eff}} = \frac{\int_0^\infty V_{eff}(E)\sigma_\nu(E)\frac{d\Phi_\nu}{dE}(E)dE}{\int_0^\infty \sigma_\nu(E)\frac{d\Phi_\nu}{dE}(E)dE} \tag{A.26}$$

$$= \frac{\sum_{i=1}^{N_{sim}} w_{\circ,i}\frac{d\Phi_\nu}{dE}(E_i)\delta_i}{\rho N_A\tau\Omega\int_0^\infty \sigma_\nu(E)\frac{d\Phi_\nu}{dE}(E)dE}. \tag{A.27}$$

Appendix B

Time-Dependent Search for Point Sources

Photon fluxes from many astrophysical phenomena exhibit time dependence to a varying extent. GeV – TeV photon observations of AGN reveal flaring on timescales of days, with intensities often several times larger than the flux of the AGN in its quiescent state. GRBs are much more extreme, with burst timescales ranging from milliseconds to a few minutes [48]. Finally, binary systems are naturally periodic, and the microquasar LS I +61 303 exhibits TeV photon emission corresponding to the orbital phase of the system [164]. Such photon fluxes may be indicative of the time dependence of hadron acceleration and therefore indicative of neutrino fluxes. Since the background atmospheric neutrino flux is not strongly dependent on time, any time dependence of an astrophysical neutrino signal provides a means to reduce this background and therefore reduce the number of events needed to claim a discovery.

Time dependent signals can be isolated by selecting only events around the flare or burst (i.e. a time bin), but this approach suffers all the drawbacks of binned methods described in chapter 6. The maximum-likelihood search presented in chapter 6 can be extended to include this time dependence.

B.1 Flares or Bursts with an Assumed Time Dependence

A time-dependent factor is added to the signal PDF:

$$\mathcal{S}_i = \mathcal{L}(\Psi_i) \times \mathcal{L}(\mathrm{E}_i) \times \mathcal{L}(\mathrm{T}_i). \tag{B.1}$$

The likelihood $\mathcal{L}(\mathrm{T}_i)$ describes the time distribution of events produced by the source. This time distribution can be assumed from photon observations of the burst, e.g. normalized keV – MeV light

curves from a GRB. The likelihood $\mathcal{L}(\mathrm{T}_i)$ may alternatively describe a period of time longer than a single flare or burst burst, and could be e.g. normalized long-term light curves for an AGN. We consider a single burst with a time dependence described by a Gaussian centered on time $\mathrm{T}_\circ$. The signal PDF from chapter 6 becomes

$$\mathcal{S}_i(\Psi_i, \sigma_i, \mathrm{Nch}_i, \gamma, \Delta\mathrm{T}_i, \sigma_\mathrm{T}) = \frac{1}{2\pi\sigma_i^2} e^{-\frac{\Psi_i^2}{2\sigma_i^2}} \times P(\mathrm{Nch}_i|\gamma) \times \frac{1}{\sqrt{2\pi}\sigma_\mathrm{T}} e^{-\frac{\Delta\mathrm{T}_i^2}{2\sigma_\mathrm{T}^2}}, \tag{B.2}$$

where $\Delta\mathrm{T}_i$ is the time difference between event i and $\mathrm{T}_\circ$. The atmospheric neutrino background is approximately uniform with time, so we normalize the background PDF with the livetime T_L:

$$\mathcal{B}_i(\mathrm{Nch}_i) = \frac{1}{\Omega_\mathrm{band}\mathrm{T}_L} \times P(\mathrm{Nch}_i|Atm_\nu). \tag{B.3}$$

If the detector efficiency is not 100%, the time dependence of the detector uptime should be included in the signal and background PDFs. Additionally, the zenith angles of source locations are time dependent for detectors away from the poles of the Earth. In such a case, the zenith dependence of atmospheric neutrino fluxes creates a time-dependent background and must be incorporated into the background PDF. Similar to the time-independent search, the likelihood

$$\mathcal{L}(\vec{x}_s, n_s, \gamma) = \prod_{i=1}^{N} \left(\frac{n_s}{N}\mathcal{S}_i + (1 - \frac{n_s}{N})\mathcal{B}_i \right), \tag{B.4}$$

is maximized with respect to the free parameters n_s and γ, and the test statistic is

$$\lambda = -2 \cdot sign(\hat{n}_s) \cdot \log \left[\frac{\mathcal{L}(\vec{x}_s, 0)}{\mathcal{L}(\vec{x}_s, \hat{n}_s, \hat{\gamma})} \right]. \tag{B.5}$$

For some bursts, GRBs in particular, stronger assumptions on the energy distribution are favored (e.g. a broken power law). In such cases, the energy term $P(\mathrm{Nch}_i)$ can be determined from simulation for the desired energy spectrum and used directly in the signal PDF, and the only free parameter is n_s.

B.2 Flares or Bursts with an Unknown Time Dependence

Neutrino bursts may not necessarily be accompanied by strong bursts of photons. Furthermore, the time dependence of photon bursts may potentially be different from any neutrino component of the burst. We therefore consider a search for neutrino bursts without bias toward the burst time or duration.

We additionally do not know the functional form of the time dependence. Neutrino bursts may exhibit approximate Gaussian or top-hat time dependence, or the bursts may be more complex. Since AMANDA is sensitive to bursts or flares with low statistics (∼10 events), the precise functional form of the time dependence is not critical; we therefore assume the time dependence is Gaussian. The signal and background PDFs are identical to the search with known time dependence (equation B.2), except the burst time $\mathrm{T}_\circ$ and duration σ_T are not known. We maximize the likelihood in equation B.4 with respect to n_s and γ, and additionally with respect to $\mathrm{T}_\circ$ and σ_T to identify a best-fit burst. The numerical maximization of the likelihood by MINUIT cannot reliably find the global likelihood maximum without accurate first guess values for the time parameters $\mathrm{T}_\circ$ and σ_T. To identify the first guess values, we first identify events within 5° of the source location. We then assume each pair of consecutive events in time represents a Gaussian burst with mean time $\mathrm{T}_\circ$ equal to the average time of the two events, and width σ_T equal to the RMS time of the two events relative to $\mathrm{T}_\circ$. We then compute the likelihood using $n_s = 2$ and $\gamma = 2.0$, and we keep the the parameters $\mathrm{T}_\circ$ and σ_T for the pair giving the maximum likelihood. We then repeat the procedure for 3, 4, and 5 consecutive events, and the parameters $\mathrm{T}_\circ$ and σ_T which give the overall maximum likelihood are used as a first guess. Numerical maximization with MINUIT yields the global maximum likelihood and best fit parameters $\hat{n}_s$, $\hat{\gamma}$, $\hat{\mathrm{T}}_\circ$, and $\hat{\sigma}_\mathrm{T}$.

B.2.1 Test Statistic and Approximation of the Likelihood Function

The ratio of the background-only likelihood (i.e. $n_s = 0$) and the best fit likelihood using $\hat{n}_s$, $\hat{\gamma}$, $\hat{\mathrm{T}}_\circ$, and $\hat{\sigma}_\mathrm{T}$, similar to equation B.5, is not an adequate test statistic when both the burst time and duration are unknown and are fit to maximize the likelihood. The desired test statistic is the comparison of the background-only likelihood to the signal likelihood, i.e.

$$\lambda = -2 \cdot sign(\hat{n}_s) \cdot \log \left[\frac{\mathcal{L}(\vec{x}_s, 0)}{\mathcal{L}(\vec{x}_s, \hat{n}_s)} \right], \tag{B.6}$$

marginalizing the additional signal parameters γ, $\mathrm{T}_\circ$, and σ_T, which add extra degrees of freedom to the signal hypothesis. This marginal likelihood is

$$\mathcal{L}(\vec{x}_s, n_s) = \int_\gamma \int_{\log \sigma_\mathrm{T}} \int_{\mathrm{T}_\circ} \mathcal{L}(\vec{x}_s, n_s, \gamma, \sigma_\mathrm{T}, \mathrm{T}_\circ) \mathrm{P}(\gamma) \mathrm{P}(\log \sigma_\mathrm{T}) \mathrm{P}(\mathrm{T}_\circ) d\mathrm{T}_\circ d(\log \sigma_\mathrm{T}) d\gamma. \tag{B.7}$$

The prior $\mathrm{P}(\gamma)$ is the spectral index penalty function described in chapter 6, $\mathrm{P}(\log \sigma_{\mathrm{T}})$ is uniform, and $\mathrm{P}(\mathrm{T}_{\circ}) = 1/\mathrm{T}_L$ when the detector is operating and zero when it is off. The parameters γ and $\log \sigma_{\mathrm{T}}$ do not add significant freedom to the signal hypothesis, and integration over these parameters can be ignored, i.e. maximization is adequate, as was done for γ in equation B.5 and in chapter 6. The parameter $\mathrm{T}_{\circ}$, however, has significant freedom; the burst could potentially occur at any time during the livetime T_L, and the prior probability of the burst occurring at $\mathrm{T}_{\circ}$ is roughly $\sim\frac{\sigma_{\mathrm{T}}}{\mathrm{T}_L}$. We therefore integrate over $\mathrm{T}_{\circ}$. For large signals, the only contribution to the likelihood integral is from the region near the maximum at $\hat{\mathrm{T}}_{\circ}$, which is approximately Gaussian with width $\sim\sigma_{\mathrm{T}}$, and the integral over $\mathrm{T}_{\circ}$ can be approximated:

$$\int_{T_0} \mathcal{L}(\vec{x}_s, \hat{n}_s, \hat{\gamma}, \hat{\sigma}_{\mathrm{T}}, \mathrm{T}_{\circ}) \frac{1}{\mathrm{T}_L} d\mathrm{T}_{\circ} \simeq \frac{\sqrt{2\pi}\sigma_{\mathrm{T}}}{\mathrm{T}_L} \mathcal{L}(\vec{x}_s, \hat{n}_s, \hat{\gamma}, \hat{\sigma}_{\mathrm{T}}, \hat{\mathrm{T}}_{\circ}). \tag{B.8}$$

The test statistic is

$$\lambda = -2 \cdot sign(\hat{n}_s) \cdot \log \left[\frac{\mathrm{T}_L}{\sqrt{2\pi}\sigma_{\mathrm{T}}} \frac{\mathcal{L}(\vec{x}_s, 0)}{\mathcal{L}(\vec{x}_s, \hat{n}_s, \hat{\gamma}, \hat{\sigma}_{\mathrm{T}}, \hat{\mathrm{T}}_{\circ})} \right]. \tag{B.9}$$

The discovery potential for E^{-2} neutrino bursts using this method, both when the burst parameters ($\mathrm{T}_{\circ}$, σ_{T}) are known and unknown, is shown in figure B.1 as a function of burst duration. The data is representative of one year operation of a $\sim\mathrm{km}^3$ scale neutrino detector similar to IceCube, with an angular resolution of 0.7° and 67,000 background atmospheric neutrinos. Less events are required for discovery at shorter burst timescales, and additionally less events are required when the burst parameters are known. For long-duration bursts (t > 0.1 year), the time-dependent search with unknown burst parameters does not perform as well as the time-independent search; however for short-duration bursts, the method identifies the burst time and reduces the number of events necessary for discovery. The method performs significantly better than binned equivalents.

B.3 Periodic Sources

Microquasars are binary systems which include a neutron star or black hole and may show natural periodicity due to the orbit of the compact object about its companion star. In particular, the microquasar LS I +61 303 exhibits a well known radio periodicity of 26.496 days [165], corresponding to the orbital period of the system. X-ray fluxes [166], and most recently GeV [167] and TeV [164]

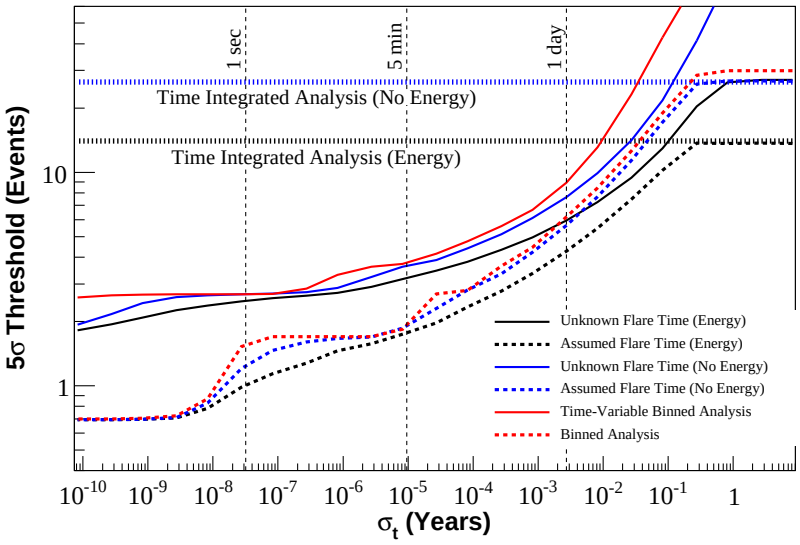

Figure B.1: Simulated IceCube discovery potential (5σ, 50% power) to an E^{-2} neutrino burst with Gaussian time dependence as a function of burst duration. Shown are the method when the burst parameters ($T_\circ$, σ_T) are assumed (dashed) and when the parameters are fitted (solid), for the likelihood methods described (black), the likelihood methods without the energy term (blue), and binned methods. The time-integrated discovery potentials (dotted) are shown for comparison.

photon fluxes, have been observed to vary according to the orbital phase. TeV observations of LS I +61 303 are shown in figure B.3.

High energy neutrino fluxes produced by LS I +61 303 may similarly be periodic. We perform a maximum-likelihood search, modifying the signal PDF to include dependence on the orbital phase of the system. This phase dependence is modeled as a Gaussian, with the phase of maximum emission ϕ and Gaussian phase width σ_w unknown and fit to the data, similar to the search described in the previous section. The signal PDF is

$$\mathcal{S}_i(\Psi_i, \sigma_i, \mathrm{Nch}_i, \gamma, \Delta\phi_i, \sigma_w) = \frac{1}{2\pi\sigma_i^2} e^{-\frac{\Psi_i^2}{2\sigma_i^2}} \times P(\mathrm{Nch}_i|\gamma) \times \frac{1}{\sqrt{2\pi}\sigma_w} e^{-\frac{\Delta\phi_i^2}{2\sigma_w^2}}, \tag{B.10}$$

where $\Delta\phi_i$ is the difference in orbital phase between event i and the mean ϕ, -0.5 $< \Delta\phi_i <$ 0.5. The background PDF is simply

$$\mathcal{B}_i(\mathrm{Nch}_i) = \frac{1}{\Omega_{\mathrm{band}}} \times P(\mathrm{Nch}_i|Atm_\nu) \tag{B.11}$$

with no time normalization term since the integral of orbital phase from 0 to 1 is unity. The test statistic is

$$\lambda = -2 \cdot sign(\hat{n}_s) \cdot \log\left[\frac{1}{\sqrt{2\pi}\sigma_w} \frac{\mathcal{L}(\vec{x}_s, 0)}{\mathcal{L}(\vec{x}_s, \hat{n}_s, \hat{\gamma}, \hat{\sigma}_w, \hat{\phi})}\right], \tag{B.12}$$

but the leading factor of $\frac{1}{\sqrt{2\pi}\sigma_w}$ is not essential since σ_w is unlikely to be more than $\sim$2 orders of magnitude smaller than the orbital period. Figure B.2 shows the time-averaged sensitivity and discovery potential of this method as a function of the Gaussian width of simulated signals, relative to the time-integrated analysis of chapter 7. For widths not significantly smaller than the orbital period, this method performs poorly compared to the time-integrated analysis due to the extra free parameters in the signal likelihood. For small widths, the method is able to lock on to the phase region where neutrino emission occurs, reducing the background and the number of events necessary for discovery. Nine events from the AMANDA data are within 3° of the position of LS I +61 303, shown in figure B.3. Application of the method reveals no significant event clustering.

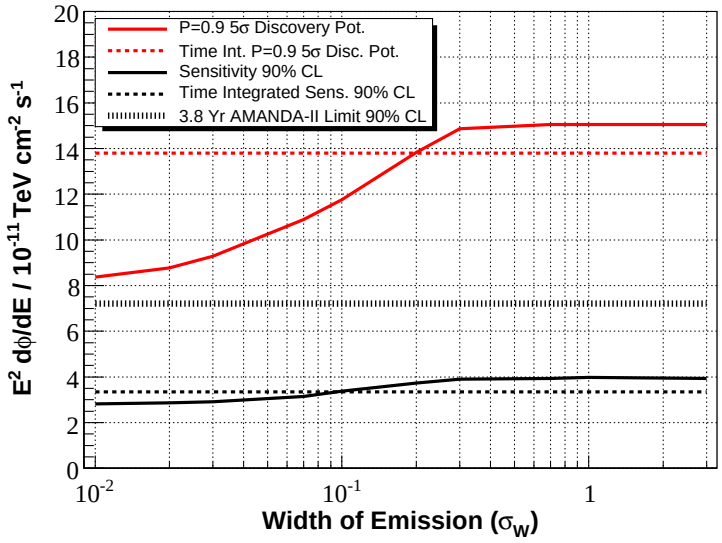

Figure B.2: Time-averaged sensitivity at 90% CL (black, solid) and 5σ discovery potential at 90% power (red, solid) to a periodic neutrino signal from LS I +61 303 with respect to the period width of neutrino emission, assuming the emission follows a Gaussian profile with respect to the orbital phase. For comparison are the sensitivity (black, dashed), 90% CL flux upper limit (black, dotted), and discovery potential (red, dashed) of the time-integrated analysis from chapter 7.

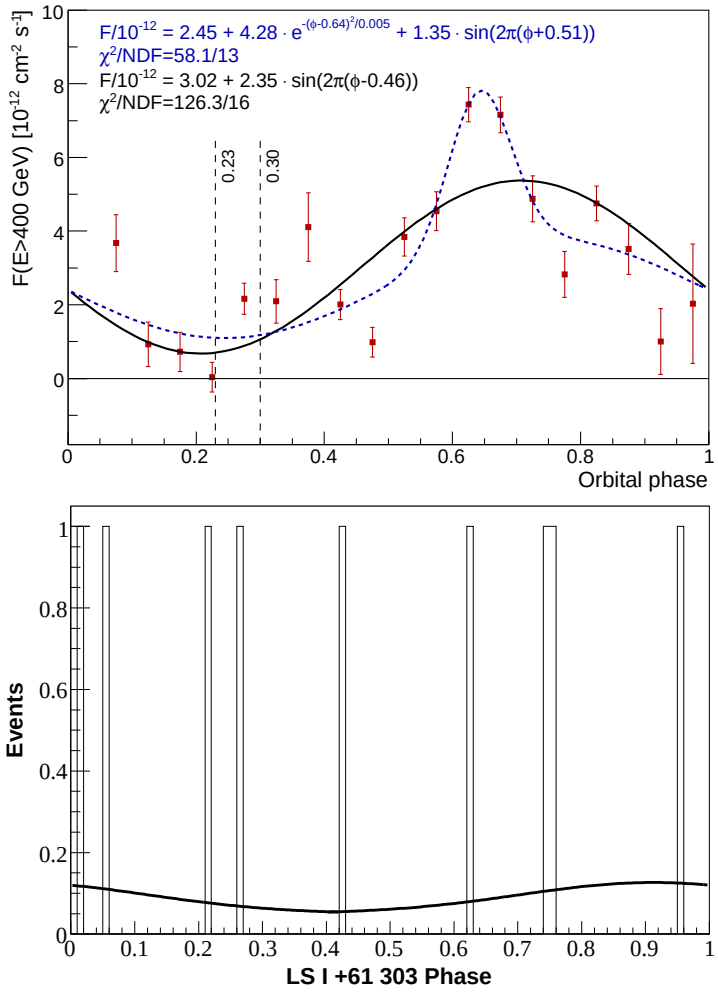

Figure B.3: LS I +61 303 TeV photon flux observed by MAGIC (from [164]) with respect to orbital phase (top), and nine events observed by AMANDA within three degrees of LS I +61 303 (bottom), along with the best signal fit to the orbital phase.